Investigation into the Effectiveness of Arrays of Slots Radiating through Truncated Waveguides to Combat the Formation of Second-Order Lobes



EGH490 FINAL DELIVERY

Submitted to the

School of Electrical Engineering & Robotics

Queensland University of Technology

For the degree of

BACHELOR OF ENGINEERING

in

ELECTRICAL & AEROSPACE

Submitted by

Chabod Masere

Supervised by

Dr Jacob Coetzee

Acknowledgements

I would like to express my sincere gratitude to my supervisor, Dr Jacob Coetzee, for his guidance, technical insight, and support throughout this research project. His direction helped shape the development of this work, from the early single-slot modelling stage through to the final truncated slotted waveguide array implementation.

I also acknowledge the School of Electrical Engineering and Robotics at Queensland University of Technology for providing the academic environment, software access, and technical resources required to complete this project. The use of CST Studio Suite and related engineering tools was essential to the simulation, modelling, and analysis carried out in this research.

Finally, I would like to thank my family, peers, and colleagues for their encouragement throughout this project. Their support was valuable during the challenges of simulation, design refinement, prototyping, and report preparation.

Chabod Masere

Investigation into the Effectiveness of Arrays of Slots Radiating through Truncated Waveguides to Combat the Formation of Second-Order Lobes

Chabod Masere[1]

[1]School of Electrical Engineering and Robotics, QUT

Abstract– This research investigates the effectiveness of truncated slotted waveguide arrays for suppressing unwanted second-order lobes in the far-field radiation pattern. A single-slot CST model was first developed and evaluated using a 23×21 parametric sweep over cavity-slot offset and cavity-slot length, producing 483 simulation cases. The extracted response was then used to generate a truncated 6×6 slotted waveguide array with controlled, non-uniform slot geometry. A target sidelobe level of -25 dB was set. The final CST model achieved a sidelobe level of approximately -23.2 dB at 9 GHz, with the main lobe directed at $\phi = 90^\circ$ and a 3 dB angular width of 14.2°. Although the result remained 1.8 dB above the target, it demonstrated meaningful sidelobe suppression and validated the proposed approach as a preliminary optimisation method for truncated slotted waveguide arrays.

Index Terms– *Slotted waveguide arrays; truncated waveguides; second-order lobe suppression; sidelobe reduction; far-field directivity; slot admittance; aperture excitation; antenna array design.*

I. INTRODUCTION

The formation of second-order lobes is a significant challenge in the design of slotted waveguide arrays, particularly in applications requiring high directivity, efficient aperture radiation, and controlled far-field behaviour. Slotted waveguide array antennas are widely used in radar, communication, and remote-sensing systems because they offer high gain, low transmission loss, strong power-handling capability, and mechanically robust aperture structures [3, 4]. In these antennas, electromagnetic energy propagates through the waveguide and is radiated through a sequence of carefully positioned slots. The location, length, offset, and excitation of these slots determine how the radiated fields combine in the far field.

Ideally, the slot contributions combine constructively in the desired main-beam direction while remaining suppressed elsewhere. However, unwanted spatial harmonics can arise when the slot spacing, excitation phase, or guided-wave propagation characteristics are not adequately controlled. These harmonics may produce secondary radiation maxima away from the main beam, referred to in this work as second-order lobes. Their presence degrades radiation-pattern quality by redistributing radiated power away from the intended direction and increasing off-axis radiation. This behaviour is related to the broader array-antenna problem of unwanted spatial radiation modes, where periodic spacing and phase progression can generate additional lobes within the visible region of the radiation pattern [5].

The problem becomes more difficult in truncated slotted waveguide arrays because the finite aperture length and limited number of radiating elements introduce edge effects and modify the aperture-field distribution. These effects can increase sidelobe and higher-order lobe levels if the slot geometry, slot offset, slot spacing, and excitation distribution are not carefully controlled. For radar and aerospace communication systems, this can reduce directivity, aperture efficiency, angular discrimination, and directional signal reliability [6, 7].

This research investigates the use of truncated waveguide slot geometry as a method for suppressing second-order lobes in a slotted waveguide array. The work focuses on controlling the cavity-slot offset and cavity-slot length through single-slot self-admittance analysis, spline-based array synthesis, and full 6×6 CST verification. The aim is to reduce unwanted secondary radiation while preserving a dominant main beam and maintaining practical waveguide-array performance.

II. SECOND-ORDER LOBES

Before discussing second-order lobes directly, it is useful to define the main features of an antenna radiation pattern. As shown in Fig. 1, the main lobe is the dominant radiation region and represents the intended direction of maximum radiated power. The beamwidth describes the angular spread of this main beam, commonly measured between the half-power points. Side lobes are smaller radiation maxima that occur away from the main lobe, while nulls are angular regions where the radiated field is strongly reduced [1, 2].

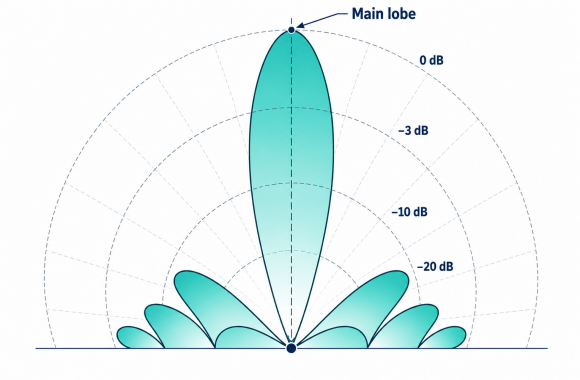


Figure 1. *General antenna radiation-pattern terminology showing the main lobe, beamwidth, side lobes, and nulls. These features provide the basis for interpreting unwanted second-order lobes in slotted waveguide arrays.*

Second-order lobes are unwanted secondary radiation maxima that appear away from the intended main beam of an antenna array. In slotted waveguide arrays, these lobes can form when the slot spacing, guided-wave phase progression, or aperture excitation distribution permits higher-order spatial harmonics to radiate. Although the main beam carries the desired radiated energy, second-order lobes redirect part of the radiated power into unintended angular regions. This reduces pattern cleanliness and can degrade directivity, gain, aperture efficiency, and radiation control [3, 4].

From an antenna-design perspective, the presence of second-order lobes is undesirable because the array no longer radiates predominantly in the intended direction. Instead, part of the energy is distributed into off-axis lobes, which can produce false angular responses, increase interference, and reduce the effectiveness of the radiating aperture. In array antennas, unwanted lobes are closely related to the spatial sampling of the aperture, the element spacing, and the phase progression across the array [1, 5]. In applications such as radar, wireless communications, telemetry, and electronic warfare, unwanted radiation maxima can compromise system performance because energy is transmitted or received in directions outside the intended coverage region [2, 6].

The second-order lobe problem is illustrated in Fig. 2 and Fig. 3. In Fig. 2, the radiation surface contains a dominant main beam together with multiple irregular off-axis lobes distributed across the visible region. This type of pattern shows how a poorly controlled aperture response can scatter energy into several unintended directions. The surrounding lobes are not part of the desired main-beam radiation and therefore represent unwanted radiation components.

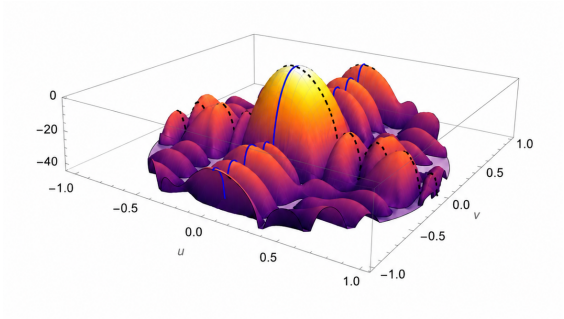


Figure 2. *Illustrative three-dimensional radiation pattern showing a dominant main beam accompanied by multiple irregular off-axis lobes; secondary radiation maxima can distribute energy into unintended directions.*

Figure 3 shows a more regular lobe structure. In this case, the main beam remains dominant, but repeated secondary maxima are visible around the main radiation region. These repeated lobes indicate that the array is radiating through additional angular channels instead of concentrating energy only into the intended beam. Even when these lobes are lower than the main beam, they are still undesirable because they reduce the usable radiation efficiency of the aperture and can contribute to interference or false directional responses [1, 5].

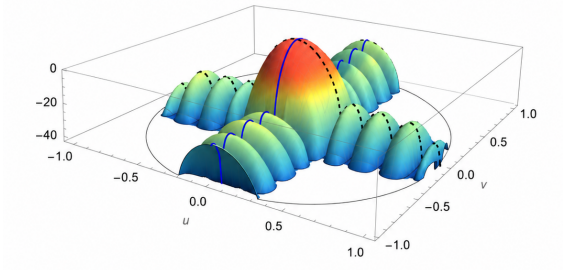


Figure 3. *Illustrative three-dimensional radiation pattern showing a dominant main beam with a more regular secondary-lobe structure. Although the main beam remains strongest, repeated off-axis lobes are still present and represent unwanted radiation.*

The key design objective is therefore not only to maintain a strong main beam, but also to reduce the strength of the surrounding second-order lobes.

In a slotted waveguide array, this can be approached by controlling the slot geometry across the aperture rather than using a purely uniform slot arrangement. By varying the slot offset and slot length, the local coupling strength and phase contribution of each radiating element can be adjusted. This allows the aperture excitation to be shaped more deliberately, which provides a basis for reducing unwanted lobe formation [4, 7].

In this research, the second-order lobe problem is addressed using a truncated-waveguide slot array. The single-slot model is first analysed to determine how the cavity-slot offset, x^{cav}, and cavity-slot length, L^{cav}, influence the local radiating behaviour. The extracted self-admittance data are then used as a lookup basis for generating the full 6×6 array. Through spline interpolation and centreline mapping, each slot is assigned an element-specific offset and length. This process enables a controlled, non-uniform slot distribution intended to suppress unwanted second-order lobes while preserving the dominant main beam.

III. INITIAL SINGLE-SLOT WAVEGUIDE MODEL

The first stage of the research used the CST Studio Suite as the full-wave electromagnetic simulation platform. CST was used to construct the waveguide geometry, assign material regions, define the cavity and slot parameters, configure the waveguide excitation, simulate the electromagnetic field behaviour, and extract the far-field radiation patterns. This provided a consistent environment for studying how the waveguide and slot geometry influenced sidelobe behaviour and second-order lobe formation.

The study began with a simplified single-slot rectangular waveguide model, then progressed to the final truncated 6×6 slotted waveguide array. The single-slot model was used to examine the radiation behaviour of an individual slot under controlled conditions before introducing array-level effects such as repeated slot placement, aperture truncation, mutual coupling, and higher-order lobe formation. This stage included the baseline waveguide, truncated cavity, cavity slot, vacuum assignment, curve refinement, and waveguide excitations at both ends of the model.

a. Design Parameters

The operating frequency was set to 9 GHz, which lies within the X-band. This frequency was used to define the electromagnetic length scales of the single-slot waveguide model. The corresponding free-space wavelength was calculated as

$$\lambda_0 = \frac{c}{f}, \tag{1}$$

where $c = 3.00 \times 10^8$ m/s and $f = 9.00 \times 10^9$ Hz. Substituting these values gives

$$\lambda_0 = \frac{3.00 \times 10^8}{9.00 \times 10^9} = 0.03333 \text{ m} = 33.33 \text{ mm}. \tag{2}$$

However, because the field propagates inside a rectangular waveguide, the guided wavelength of the dominant TE_{10} mode was used as the main longitudinal design reference. In CST, this was defined as

$$\lambda_{10} = \frac{1000}{\left[\left(\frac{f}{0.299792458}\right)^2 - \left(\frac{500}{a}\right)^2\right]^{1/2}}, \tag{3}$$

where f is entered in GHz and the broad-wall waveguide dimension a is entered in millimetres. For $f = 9$ GHz and $a = 22.86$ mm,

$$\lambda_{10} = \frac{1000}{\left[\left(\frac{9}{0.299792458}\right)^2 - \left(\frac{500}{22.86}\right)^2\right]^{1/2}} = 48.63 \text{ mm}. \tag{4}$$

The initial waveguide length was therefore set equal to the guided wavelength:

$$\ell = \lambda_{10} = 48.63 \text{ mm}. \tag{5}$$

The wave impedance parameter used in the CST model was calculated from

$$Z_{\text{wave}} = f(1.256637)\lambda_{10}. \tag{6}$$

$$Z_{\text{wave}} = 9(1.256637)(48.63) = 550.0\ \Omega. \tag{7}$$

The analytical CST parameters used to define the model are summarised in Table 1, while the corresponding physical geometry dimensions are listed in Table 2.

b. Waveguide Overview

The single-slot model was constructed as a rectangular waveguide section with a central radiating slot and truncated cavity region. The physical waveguide body had an overall length of 48.63 mm, width of 45.72 mm, and height of 17.70 mm. The feeding mouth retained the standard rectangular waveguide aperture dimensions of 22.86 mm $\times$ 10.16 mm, corresponding to the broad-wall and narrow-wall dimensions of the X-band waveguide.

A truncated cavity was positioned above the waveguide wall to control the local slot-cavity coupling behaviour. This cavity had a length of 18 mm, width of 12 mm, and depth of 5 mm. The cavity slot was defined with a length of 16 mm, width of 1.588 mm, and depth of 1.27 mm, matching the

Table 1
CST parameters used for the initial single-slot rectangular waveguide model.

Parameter	Symbol	Value
Operating frequency	f	9.0 GHz
Waveguide width	a	22.86 mm
Waveguide height	b	10.16 mm
Wall thickness	t	1.27 mm
Slot width	w	1.5875 mm
Side length	side	22.86 mm
Guide wavelength	λ_{10}	48.6303 mm
Waveguide length	ℓ	48.6303 mm
Slot displacement	δ	0 mm
Adjusted length	ℓ_δ	48.6303 mm
Overall model width	width	45.72 mm
Wave impedance	Z_{wave}	549.995 Ω
Cavity width	a_{cavity}	12 mm
Cavity height	b_{cavity}	5 mm
Cavity depth	d_{cavity}	18 mm
Cavity slot length	L_{cav}	16 mm
Cavity slot offset	X_{cav}	2 mm

Table 2
Physical geometry dimensions of the single-slot CST model.

Parameter	Symbol	Value
Physical waveguide length	L_{wg}	48.63 mm
Physical waveguide width	W_{wg}	45.72 mm
Physical waveguide height	H_{wg}	17.70 mm
Feeding mouth length	L_{feed}	22.86 mm
Feeding mouth width	W_{feed}	10.16 mm
Truncated cavity length	L_{tcav}	18 mm
Truncated cavity width	W_{tcav}	12 mm
Truncated cavity depth	D_{tcav}	5 mm
Cavity slot length	L_{slot}	16 mm
Cavity slot width	W_{slot}	1.588 mm
Cavity slot depth	D_{slot}	1.27 mm

wall thickness of the waveguide. These physical dimensions are listed in Table 2.

The baseline CST single-slot model is shown in Fig. 4. This model consisted of a rectangular waveguide section containing one cavity-backed radiating slot. The broad-wall dimension a and narrow-wall dimension b defined the internal waveguide cross-section, while the wall thickness t defined the metallic boundary. The slot width w, cavity slot length L_{cav}, and cavity slot offset X_{cav} defined the initial radiating aperture geometry.

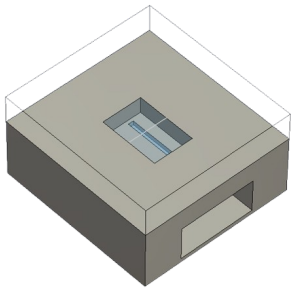


Figure 4. *CST model of the initial single-slot rectangular waveguide geometry used as the baseline configuration before development of the truncated* 6×6 *slotted waveguide array.*

c. Vacuum Region Assignment

The truncated region in the single-slot model was assigned as a vacuum in CST, as shown in Fig. 5. This was necessary because the cavity represents the internal electromagnetic volume through which the guided wave interacts with the slot aperture. If this region were treated as metal, the slot would not support the intended field penetration or radiation mechanism. By treating the cavity as a vacuum, the model approximated an air-filled slot cavity, allowing electromagnetic fields to occupy the cavity volume, couple through the aperture, and radiate from the waveguide structure.

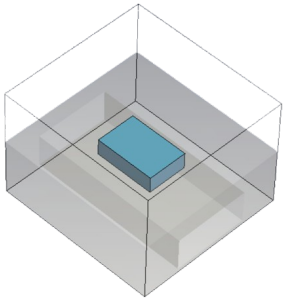


Figure 5. *CST model showing the cavity region assigned as vacuum within the initial single-slot waveguide geometry. The vacuum assignment allowed electromagnetic fields to occupy the cavity volume and couple through the slot aperture during simulation.*

d. Curve References

The slot and cavity geometry were defined using two reference curves, as shown in Fig. 6. Curve 1 and Curve 2 represent the slot-side and cavity-side boundaries of the single-slot structure. To examine the local coupling behaviour, the x-component of the electric field, E_x, was evaluated along both curves at $f = 9$ GHz.

Since the CST field result is complex in the frequency domain, both the real and imaginary components of E_x were extracted. The curve result was interpreted as the line-integrated electric-field response,

$$I_{E_x} = \int_C E_x \, dl, \tag{8}$$

where I_{E_x} represents the accumulated electric-field excitation along the selected curve. This provided a compact measure of the relative field strength and phase behaviour between the slot and cavity regions.

This analysis was used to assess how effectively the cavity region couples energy into the radiating slot aperture. Poorly controlled slot-cavity coupling can produce uneven aperture excitation, which may contribute to increased sidelobe levels when extended to the full 6×6 array. The curve-based field evaluation therefore provided a baseline measure of

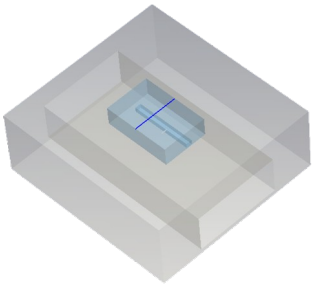


Figure 6. *CST geometry showing Curve 1 and Curve 2 used for single-slot field evaluation. The x-component of the electric field, E_x, was evaluated along both curves at $f = 9$ GHz.*

the local radiation mechanism before the design was implemented at array scale.

e. Port Excitation Setup

Waveguide ports were assigned at both ends of the single-slot model to excite the dominant guided mode through the rectangular waveguide. Each port was referenced from its respective end face and extended inward toward the centre of the structure. In CST, this was implemented using an inward extent of $-\ell/2$, where ℓ is the total waveguide length.

Since the initial waveguide length was defined as $\ell = \lambda_{10}$, each port used an inward extent of $-\lambda_{10}/2$. This kept the slot region centred while allowing the guided excitation to enter from the waveguide end faces.

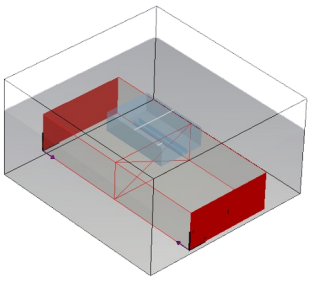


Figure 7. *Waveguide port-pin placement used in the CST single-slot model. Each port was defined with an inward extent of $-\ell/2$ from its respective end face.*

This port arrangement ensured that the slot was excited by the propagating waveguide mode rather than by a direct aperture excitation. This better represents the excitation condition used later in the full slotted waveguide array.

f. Parametric Sweep Definition

A parametric sweep was conducted to evaluate how the cavity-slot offset and cavity-slot length affected the single-slot electromagnetic response. Two geometric variables were swept: the cavity-slot offset, X_{cav}, and the cavity-slot length, L_{cav}. These parameters were selected because they directly influence the slot-cavity coupling strength, aperture excitation, and radiation behaviour.

The offset X_{cav} was varied from 0.6 mm to 5.0 mm in increments of 0.2 mm, giving 23 offset values. The cavity-slot length L_{cav} was varied from 15.0 mm to 17.0 mm in increments of 0.1 mm, giving 21 length values. The full sweep therefore produced

$$N_{\text{sweep}} = 23 \times 21 = 483 \tag{9}$$

individual simulation cases.

Table 3
Parametric sweep ranges used for the single-slot CST model.

Parameter	Symbol	Range	Step
Cavity-slot offset	X_{cav}	0.6–5.0 mm	0.2 mm
Cavity-slot length	L_{cav}	15.0–17.0 mm	0.1 mm

This sweep allowed the relationship between slot offset, cavity-slot length, and electromagnetic coupling behaviour to be examined systematically. Each value of X_{cav} was simulated across the full range of L_{cav}, producing a two-dimensional parameter space. The resulting 483 cases were then used to identify suitable geometry regions before extending the design to the truncated 6×6 slotted waveguide array.

IV. SINGLE-SLOT ANALYSIS

a. Sweep Dataset Compilation

For each geometry in the CST parametric sweep, the complex scattering parameters S_{11} and S_{21} were exported using their real and imaginary components. The reflection coefficient, S_{11}, was used to assess input-port reflection, while the transmission coefficient, S_{21}, was used to assess power transfer through the single-slot waveguide model. These quantities were represented as

$$S_{11} = \text{Re}(S_{11}) + j\,\text{Im}(S_{11}), \tag{10}$$

$$S_{21} = \text{Re}(S_{21}) + j\,\text{Im}(S_{21}). \tag{11}$$

The corresponding magnitudes were calculated using

$$|S_{11}| = \sqrt{\text{Re}(S_{11})^2 + \text{Im}(S_{11})^2}, \tag{12}$$

$$|S_{21}| = \sqrt{\text{Re}(S_{21})^2 + \text{Im}(S_{21})^2}. \tag{13}$$

The compiled dataset also included impedance and admittance-derived quantities, including Z_{11}, Z_{12}, R_{self}, X_{self}, G_{self}, and B_{self}. These values were used to interpret the equivalent electromagnetic loading introduced by each slot geometry. In particular, G_{self} and B_{self} were used to identify regions of strong slot excitation and near-resonant behaviour.

In addition to the port-based quantities, CST field-integral results were recorded for Curve 1 and Curve 2. These curves represented the cavity-side and slot-side field-evaluation paths. For each curve, the extracted integral was complex and was expressed as

$$I_{C1} = \mathrm{Re}(I_{C1}) + j\,\mathrm{Im}(I_{C1}), \tag{14}$$

$$I_{C2} = \mathrm{Re}(I_{C2}) + j\,\mathrm{Im}(I_{C2}). \tag{15}$$

The final sweep dataset therefore linked each geometric parameter pair, $(x^{\mathrm{cav}}, L^{\mathrm{cav}})$, to its corresponding scattering response, equivalent admittance, and local field-integral behaviour. This allowed the relationship between slot geometry, port matching, transmission, self-admittance, and slot-cavity excitation to be examined systematically.

b. Self-Admittance Analysis and Equivalent Circuit

The single-slot response was interpreted using the equivalent two-port transmission-line model shown in Fig. 8. The two CST waveguide ports define the input and output reference planes, while the radiating slot is represented as a normalised shunt self-admittance, Y_{self}. Since both ports were normalised to $Z_0 = 1$, the slot loading could be interpreted directly in terms of normalised admittance.

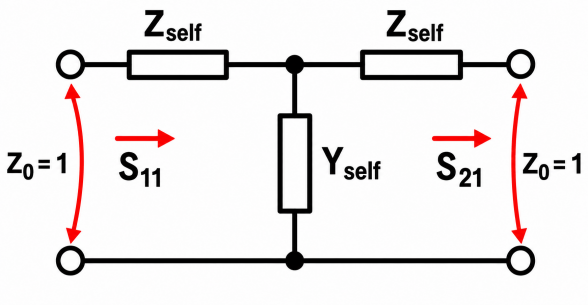


Figure 8. *Equivalent two-port transmission-line representation of the single-slot waveguide model. The radiating slot is modelled as a shunt self-admittance, Y_{self}, extracted from the scattering parameters S_{11} and S_{21} using normalised port impedances, $Z_0 = 1$.*

The self-admittance was expressed as

$$Y_{\mathrm{self}} = G_{\mathrm{self}} + jB_{\mathrm{self}}, \tag{16}$$

where G_{self} is the self-conductance and B_{self} is the self-susceptance. The conductance term represents real electromagnetic loading associated with power coupled into the radiating aperture, while the susceptance term represents the reactive component of the slot response.

For the normalised two-port model, the complex self-admittance was calculated from the CST scattering parameters using

$$Y_{\mathrm{self}} = \frac{(1 - S_{11})^2 - S_{21}^2}{2S_{21}}. \tag{17}$$

The real and imaginary components were then extracted as

$$G_{\mathrm{self}} = \mathrm{Re}\{Y_{\mathrm{self}}\}, \tag{18}$$

$$B_{\mathrm{self}} = \mathrm{Im}\{Y_{\mathrm{self}}\}. \tag{19}$$

For each offset–length combination in the sweep, the exported values of S_{11} and S_{21} were substituted into Eq. (17). This produced corresponding values of Y_{self}, G_{self}, and B_{self} for every simulated geometry.

The self-conductance, G_{self}, was used to identify regions where the slot was strongly excited and efficiently coupled energy out of the waveguide. A local maximum in G_{self} indicates stronger radiating behaviour. The self-susceptance, B_{self}, was used to assess the resonance condition of the slot. When B_{self} approaches zero, the reactive component of the slot admittance is minimised, indicating near-resonant behaviour.

The preferred design region was therefore identified by locating parameter combinations where G_{self} approached a local maximum while B_{self} remained close to zero. These conditions indicate that the slot is both strongly coupled and approximately resonant, making the corresponding cavity-slot dimensions suitable candidates for extension to the truncated 6×6 slotted waveguide array.

c. Single-Slot Self-Admittance Sweep Results

Self-admittance was extracted for each investigated cavity-slot offset in order to evaluate how the single-slot response changed with geometry. For each fixed value of cavity-slot offset, x^{cav}, the cavity-slot length, L^{cav}, was swept through its prescribed range. This produced a set of sweep curves showing the variation of self-conductance, G_{self}, and self-susceptance, B_{self}, as functions of slot length.

Only representative offset cases are included in the main body to avoid unnecessary repetition. The selected figures show the main electromagnetic trend across the sweep, beginning with weak coupling at small offsets and progressing toward stronger slot excitation at larger offsets. The purpose of the sweep was not simply to locate the maximum value of G_{self}, but to identify a physically useful region where the conductance was high while the susceptance approached or crossed the zero axis. This condition indicates that the slot was both strongly excited and approximately resonant.

The representative sweep results in Figs. 9–14 show that increasing x^{cav} generally increases the peak value of G_{self}. This trend indicates that larger cavity-slot offsets improve the coupling between the

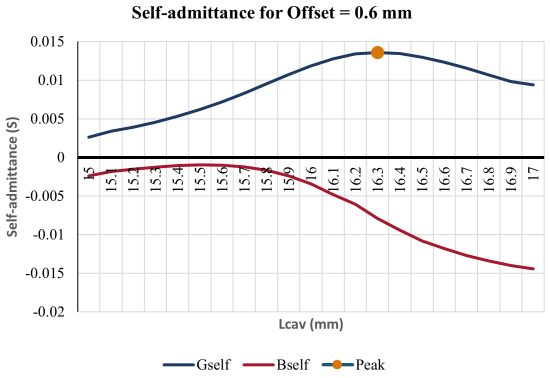


Figure 9. *Self-admittance sweep for $x^{\mathrm{cav}} = 0.6$ mm. This low-offset case shows comparatively weak self-conductance, indicating limited coupling between the guided wave and the radiating aperture.*

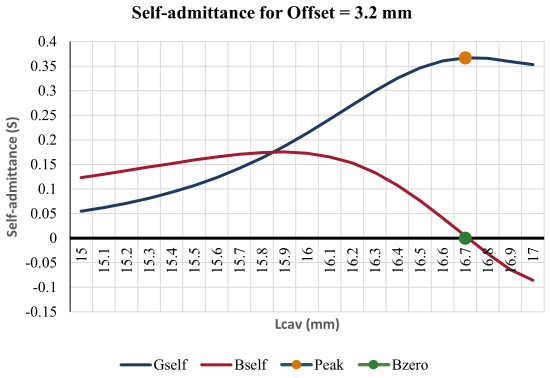


Figure 12. *Self-admittance sweep for $x^{\mathrm{cav}} = 3.2$ mm. The response shows further growth in G_{self}, indicating stronger coupling between the waveguide mode and the slot aperture.*

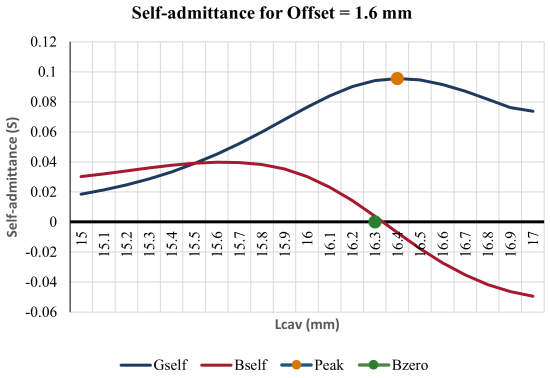


Figure 10. *Self-admittance sweep for $x^{\mathrm{cav}} = 1.6$ mm. The increase in G_{self} relative to the low-offset case shows that the slot becomes more strongly excited as the cavity-slot offset is increased.*

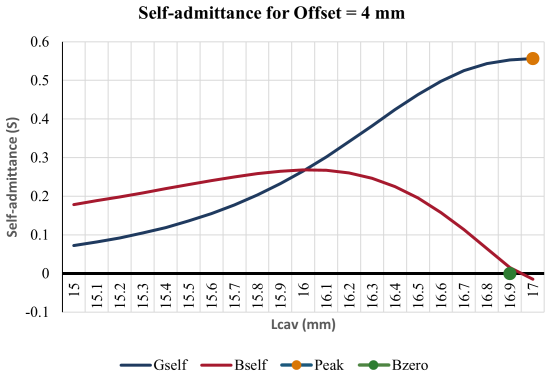


Figure 13. *Self-admittance sweep for $x^{\mathrm{cav}} = 4.0$ mm. This case represents a high-coupling region where the peak conductance becomes significantly larger than in the smaller-offset cases.*

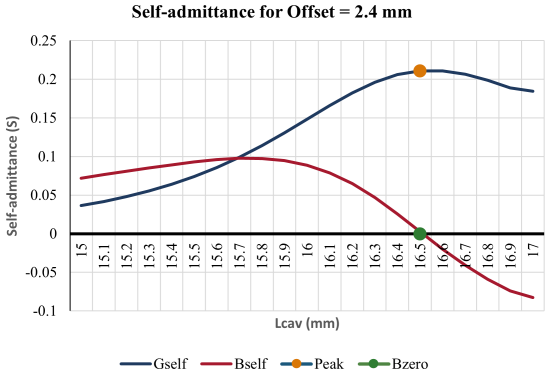


Figure 11. *Self-admittance sweep for $x^{\mathrm{cav}} = 2.4$ mm. This intermediate-offset case shows stronger conductance and a clearer transition of B_{self} through the zero axis.*

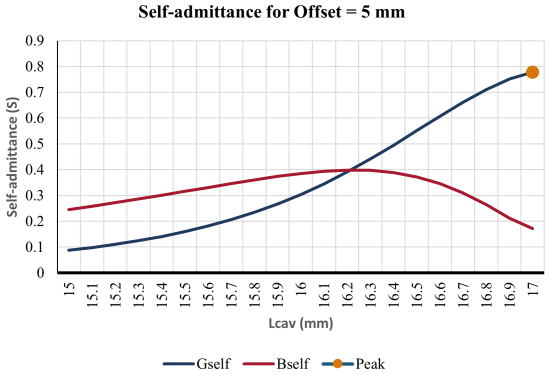


Figure 14. *Self-admittance sweep for $x^{\mathrm{cav}} = 5.0$ mm. This upper-offset case was used to assess the high-offset limit of the sweep and determine whether further increases in offset remained useful for design selection.*

guided wave and the radiating aperture. However, high conductance alone was not sufficient for selecting the final geometry. A large value of G_{self} only confirms strong coupling; it does not confirm that the slot is operating near resonance.

For this reason, B_{self} was assessed simultaneously with G_{self}. The preferred design region was identified where G_{self} was locally high and B_{self} was close to zero. This combination indicates that the slot geometry produced strong radiation while minimising reactive loading. The remaining offset sweeps showed similar intermediate behaviour and were therefore retained as verification data rather than repeated in the main body.

d. Spline Interpolation and Centreline Mapping of the Single-Slot Data

The final 6×6 cavity-slot array was generated from the single-slot CST sweep using spline interpolation. The sweep provided discrete data linking cavity-slot offset, x^{cav}, and cavity-slot length, L^{cav}, to the extracted slot response.

Spline interpolation was used because the CST sweep only evaluated finite geometry combinations. This allowed intermediate slot dimensions to be estimated with finer resolution than the original sweep step size.

The interpolation was referenced to the waveguide centreline, defined as $x^{\text{cav}} = 0$. In the single-slot model, the offset magnitude controlled the coupling strength between the guided mode and the radiating slot.

When the single-slot data were transferred to the full 6×6 array, each offset magnitude was obtained from the spline-interpolated dataset. The offset sign was then assigned according to the physical placement of the slot about the centreline.

This produced alternating positive and negative offset values across the array, as shown in Table 4. Mirrored slot locations were assigned equal-magnitude but opposite-sign offsets, preserving geometric symmetry while controlling the excitation of each radiating element.

The interpolation procedure used two mappings. First, the required conductance for each array element was mapped to a cavity-slot offset magnitude. Second, that offset magnitude was mapped to the corresponding cavity-slot length. The complete MATLAB implementation is provided in Appendix D.

The resulting table represents an array-synthesis output rather than the repeated use of one globally optimal single-slot geometry. Each element (t, n) was assigned its own cavity-slot offset, $x^{\text{cav}}_{t,n}$, and cavity-slot length, $L^{\text{cav}}_{t,n}$.

The coupling-slot angle, θ_t, and coupling-slot length, l_t, were then specified for each slot index to complete the full-array geometry.

Table 4
Cavity slot and coupling slot dimensions.

Element index	Cavity slot offset $x^{\text{cav}}_{t,n}$ (mm)	Cavity slot length $L^{\text{cav}}_{t,n}$ (mm)
1,1	1.293	16.007
1,2	-1.925	16.156
1,3	2.764	16.323
1,4	-2.764	16.323
1,5	1.925	16.156
1,6	-1.293	16.007
2,1	1.348	15.832
2,2	-2.084	15.961
2,3	2.801	16.053
2,4	-2.801	16.053
2,5	2.084	15.961
2,6	-1.348	15.832
3,1	1.324	15.803
3,2	-1.848	15.912
3,3	2.460	16.075
3,4	-2.460	16.075
3,5	1.848	15.912
3,6	-1.324	15.803
4,1	1.320	15.802
4,2	-1.840	15.911
4,3	2.495	15.997
4,4	-2.495	15.997
4,5	1.840	15.911
4,6	-1.320	15.802
5,1	1.350	15.833
5,2	-2.088	15.961
5,3	2.784	16.131
5,4	-2.784	16.131
5,5	2.088	15.961
5,6	-1.350	15.833
6,1	1.295	16.008
6,2	-1.932	16.157
6,3	2.745	16.277
6,4	-2.745	16.277
6,5	1.932	16.157
6,6	-1.295	16.008

Slot index	Coupling slot angle θ_t (deg.)	Coupling slot length l_t (mm)
1	6.879	15.775
2	-13.686	15.786
3	17.060	15.792
4	-17.155	15.792
5	13.660	15.786
6	-6.858	15.775

The values in Table 4 show alternating cavity-slot offset signs across each row. This sign convention represents slot placement on opposite sides of the waveguide centreline.

The offset magnitudes define the local coupling strength, while the cavity-slot lengths maintain the required resonant behaviour for each selected offset. The highlighted central elements correspond to the central aperture region, where slot placement is most critical for symmetry and excitation control.

V. WAVEGUIDE ARRAY

a. Full 6×6 Array Geometry Implementation

After the cavity-slot and coupling-slot dimensions were generated, the complete 6×6 array geometry was implemented in CST. The purpose of this stage was to convert the spline-generated dimensional table into a full electromagnetic model that could be simulated and evaluated at array level. This

represented the transition from isolated single-slot analysis to a complete aperture structure, where the radiating behaviour is governed not only by the geometry of each individual slot, but also by the collective interaction between all slots in the array.

The final model was constructed as a layered truncated-waveguide structure. The lower layer acted as the base conductive plate, while the upper layers introduced the coupling slots, radiating slots, and cavity-slot apertures. This layered approach allowed each functional part of the antenna to be implemented separately before being combined into the final CST model. The four principal layers are shown in Figs. 15–18.

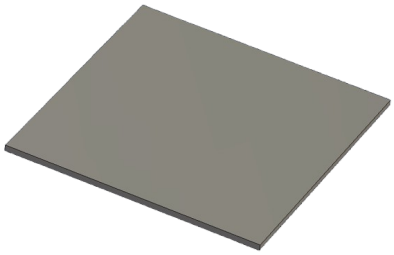


Figure 15. *Base conductive layer used in the full* 6×6 *truncated-waveguide array model. This layer provides the lower structural reference surface for the assembled geometry.*

The base layer in Fig. 15 provides the lower conductive boundary of the layered waveguide assembly. Since this layer does not contain slot features, its primary function is to define the lower metallic reference surface and support the closed waveguide structure.



Figure 16. *Coupling-slot layer of the* 6×6 *array. The non-uniform slot positions form the lower excitation distribution used to couple energy from the waveguide into the upper cavity region.*

The coupling-slot layer in Fig. 16 introduces the lower excitation features of the array. These slots are not arranged as a simple uniform grid. Instead, their offsets follow the generated design distribution, producing a controlled variation in coupling strength across the aperture. This is important because the coupling slots determine how strongly energy is transferred from the waveguide into the upper cavity-backed radiating region.

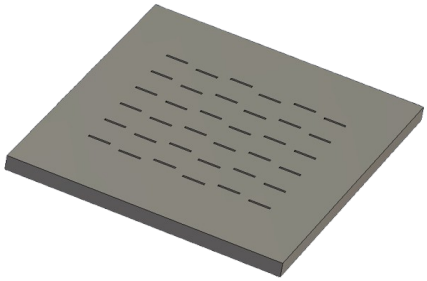


Figure 17. *Radiating slot layer of the full* 6×6 *array. The narrow slots form the upper radiating aperture distribution used to generate the far-field radiation pattern.*

The radiating slot layer in Fig. 17 forms the visible 6×6 aperture distribution. The slot positions and lengths were implemented from the spline-generated design values, allowing the excitation distribution to vary across the array rather than being produced by identical repeated slots. This non-uniformity is central to the project objective, since the aim is to shape the far-field response and suppress unwanted second-order lobes.

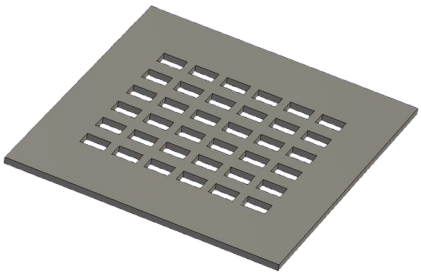


Figure 18. *Cavity-slot layer of the completed* 6×6 *array model. The larger rectangular openings define the cavity-backed aperture regions associated with each radiating element.*

The cavity-slot layer in Fig. 18 contains the larger rectangular openings associated with the cavity-backed aperture regions. These cavity features influence the local field distribution, the effective slot admittance, and the phase uniformity across the aperture. In the completed structure, the cavity layer provides an additional degree of electromagnetic control beyond simple slot offset.

A key implementation requirement was maintaining correct alignment between the coupling slots, cavity regions, and radiating slots. The cavity features were kept centred relative to the waveguide structure, while the slot offsets were varied according to the generated dimensional table. This allowed the model to preserve a consistent cavity geometry while using slot displacement as the primary mechanism for modifying local coupling strength. Since slot offset affects the effective admittance of each element, the offset distribution provides a practical

method for shaping the excitation profile across the full aperture.

The assembled CST geometry is shown in Figs. 19–22. These views show the completed array surface, mechanical chassis, conducting boundary assignment, and surrounding simulation domain used for far-field evaluation.

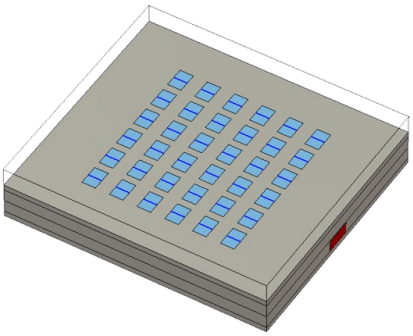


Figure 19. *Completed CST model of the* 6×6 *slotted array showing the radiating apertures on the upper face. The slot positions correspond to the spline-generated cavity-slot dimensions.*

Figure 19 shows the completed array surface with the 6×6 slot pattern applied to the upper face. The highlighted regions correspond to the radiating slot apertures. These slots were assigned using the element-specific offsets and lengths listed in Table 4. The non-uniform placement confirms that the final array was implemented as a shaped aperture rather than as a uniformly repeated slot pattern.

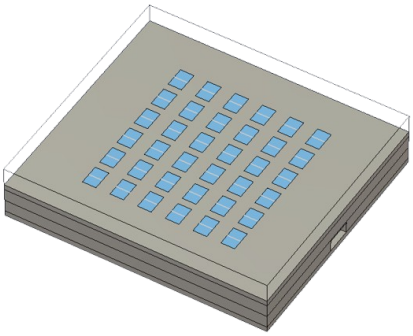


Figure 20. *CST chassis model of the* 6×6 *slotted waveguide array. The chassis defines the physical boundary of the waveguide structure and supports the radiating slot layer.*

Figure 20 shows the chassis model used to support the slot layers. The chassis defines the physical waveguide body and establishes the mechanical boundary of the array. This confirms that the slot layers were integrated into a complete truncated-waveguide structure rather than being treated as isolated conducting surfaces.

Figure 21 shows the conducting regions after material assignment. The metallic regions were modelled as perfect electric conductor (PEC) boundaries

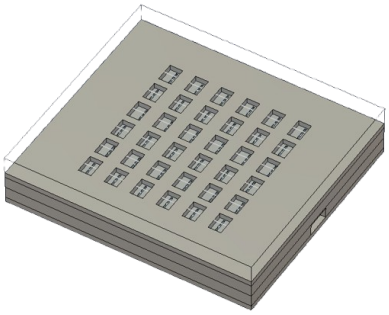


Figure 21. *PEC assignment applied to the* 6×6 *slotted array model. The conducting waveguide body and slot boundaries were treated as ideal metallic surfaces during simulation.*

for the electromagnetic simulation. This approximation allowed the waveguide walls and slot boundaries to be treated as ideal conductors, providing a useful first-order model before introducing material loss, surface roughness, or fabrication tolerances.

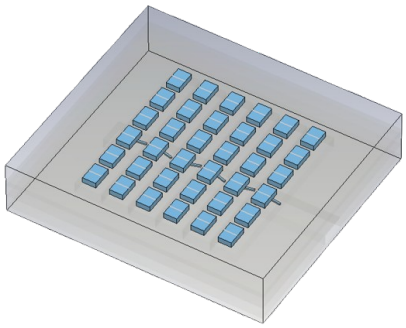


Figure 22. *Vacuum simulation domain surrounding the* 6×6 *slotted array. The external region allows the fields radiated from the apertures to propagate into free space for far-field evaluation.*

Figure 22 shows the surrounding vacuum region used to model the radiating environment. This external domain is required so that fields leaving the slot apertures can propagate into free space. The inclusion of this region allowed the far-field directivity pattern and lobe behaviour of the full array to be evaluated after the geometry was assembled.

The completed geometry introduced electromagnetic effects that were not present in the isolated single-slot model. In the single-slot case, the extracted self-admittance provides an estimate of how one slot couples energy from the waveguide into the radiating aperture. In the full array, each slot is influenced by neighbouring elements through mutual coupling inside the waveguide and external coupling through the aperture region. Therefore, the full 6×6 array cannot be interpreted as a direct repetition of the single-slot result. Instead, the CST model captures higher-order interactions, edge effects, cavity loading, and the cumulative impedance presented

by the complete aperture to the feeding waveguide.

Before simulation, the completed geometry was visually and dimensionally checked. This included verifying the 6×6 slot count, confirming that the slot offsets followed the generated dimensional table, checking that the cavity and coupling-slot layers were correctly aligned, and ensuring that the structure remained electrically continuous where required. These checks were necessary because small geometric errors in slot position, length, or cavity alignment can alter the aperture phase distribution and degrade the far-field response.

Once the full geometry was verified, CST simulations were performed to assess the completed array. The main array-level outputs were S_{11}, Smith chart response, and far-field directivity. These results allowed the input match and radiation behaviour to be evaluated together, confirming whether the final aperture remained reasonably coupled to the feed while producing the intended radiation pattern.

b. Array Equivalent Circuit and Smith Chart Interpretation

After implementation of the complete 6×6 array geometry in CST, the array response was interpreted using an equivalent shunt-admittance representation. This model provides a circuit-level interpretation of the electromagnetic loading introduced by the full slot array. While the single-slot study was used to examine the self-admittance of an isolated radiating slot, the complete array was represented by an equivalent array admittance, Y_{array}, connected across a normalised two-port transmission-line model.

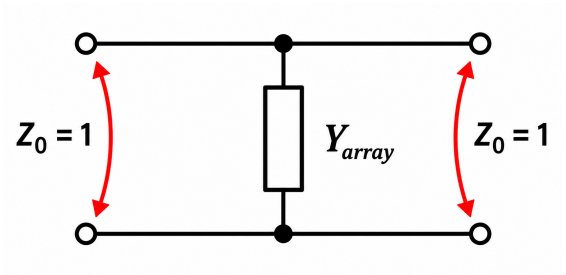


Figure 23. *Equivalent two-port representation of the completed 6×6 slotted array. The full slot array is represented as an equivalent shunt admittance, Y_{array}, connected across a normalised transmission line with $Z_0 = 1$.*

In Fig. 23, the two ports represent the input and output reference planes of the CST waveguide model. The reference impedance was normalised such that $Z_0 = 1$, allowing the slot-array loading to be interpreted using normalised impedance and admittance quantities. The central shunt element, Y_{array}, represents the combined effect of all radiating apertures in the 6×6 array. This includes the radiation conductance of the slots, the stored reactive energy associated with the aperture and cavity fields, and the effect of mutual coupling between neighbouring slots.

The equivalent array admittance can be expressed as

$$Y_{\text{array}} = G_{\text{array}} + jB_{\text{array}}, \tag{20}$$

where G_{array} is the conductance associated with real radiated power and B_{array} is the susceptance associated with stored electromagnetic energy. A useful array design should provide sufficient conductance for radiation while keeping the reactive component controlled near the operating frequency. If the susceptance is large, the array behaves as a strongly reactive discontinuity and the input match deteriorates.

For a normalised shunt admittance connected across a transmission line, the scattering response can be related to the equivalent admittance by

$$S_{11} = \frac{-Y_{\text{array}}}{2 + Y_{\text{array}}}, \tag{21}$$

and

$$S_{21} = \frac{2}{2 + Y_{\text{array}}}. \tag{22}$$

These expressions show that the reflection coefficient is directly governed by the equivalent admittance presented by the complete slot array. If the equivalent admittance is too small, the array couples weakly and radiates inefficiently. If it is too large or strongly reactive, the array becomes mismatched and produces a larger reflected wave. Therefore, the design objective is to obtain a balanced admittance that radiates effectively while remaining reasonably matched to the feeding waveguide.

The polar plot of S_{11} is shown in Fig. 24. This plot represents the reflection coefficient trajectory over the swept frequency range from 8.9 GHz to 9.1 GHz. The distance of the curve from the origin corresponds to the reflection magnitude, while the angular position corresponds to the reflection phase. The trajectory does not collapse to the origin, which confirms that the array is not perfectly matched. However, the reflection coefficient remains bounded over the swept range, which is consistent with the moderate return-loss behaviour observed in the rectangular S_{11} magnitude plot.

The impedance Smith chart is shown in Fig. 25. This view converts the reflection coefficient into an equivalent input impedance trajectory. At 8.9 GHz, the indicated input impedance is approximately

$$Z_{\text{in}} \approx 230 + j134\ \Omega, \tag{23}$$

while at 9.1 GHz it is approximately

$$Z_{\text{in}} \approx 1.14 \times 10^3 - j218\ \Omega. \tag{24}$$

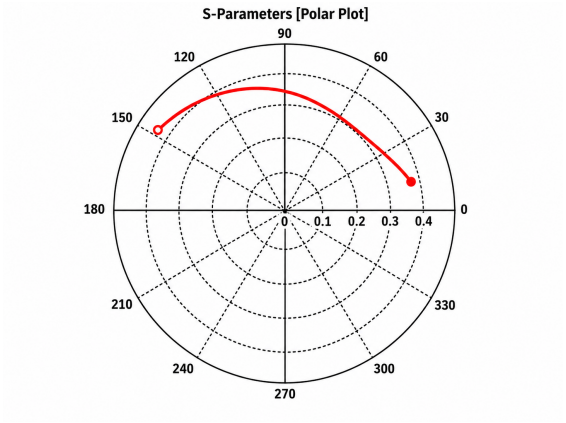


Figure 24. *Polar plot of the simulated S_{11} response of the completed 6×6 slotted array over the frequency range from 8.9 GHz to 9.1 GHz. The curve shows the variation of reflection coefficient magnitude and phase across the swept band.*

These values show that the input impedance varies significantly across the sweep and remains displaced from the ideal matched impedance. The large real component, particularly near the upper end of the sweep, indicates that the array presents a relatively high impedance to the feed. The change in the sign of the imaginary component also indicates that the input response passes through a transition between inductive and capacitive behaviour across the analysed band.

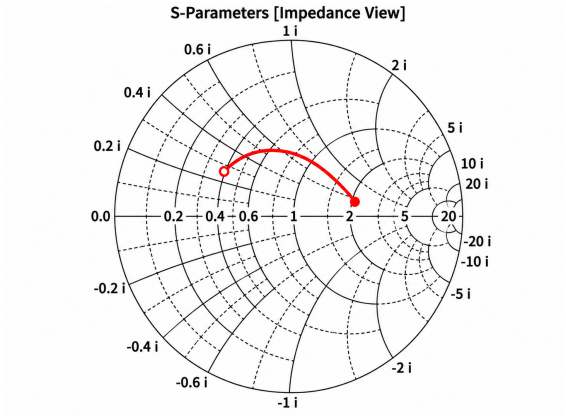


Figure 25. *Smith chart response of the completed 6×6 slotted array in impedance view. The curve shows the variation of equivalent input impedance over the swept frequency range.*

The same response is shown in admittance form in Fig. 26. This representation is more directly connected to the equivalent circuit in Fig. 23, since the slot array is modelled as a shunt admittance. At 8.9 GHz, the indicated input admittance is approximately

$$Y_{\text{in}} \approx 0.00325 - j0.00189 \text{ S}, \qquad (25)$$

while at 9.1 GHz it is approximately

$$Y_{\text{in}} \approx 0.000847 + j0.000162 \text{ S}. \qquad (26)$$

The real part of the admittance represents the conductance available for power transfer into the array, while the imaginary part represents the residual reactive loading. The reduction in conductance from 8.9 GHz to 9.1 GHz indicates that the effective coupling of the array changes across the sweep. The relatively small imaginary admittance at the upper end of the band suggests that the response becomes less reactive there, although the total conductance is also reduced.

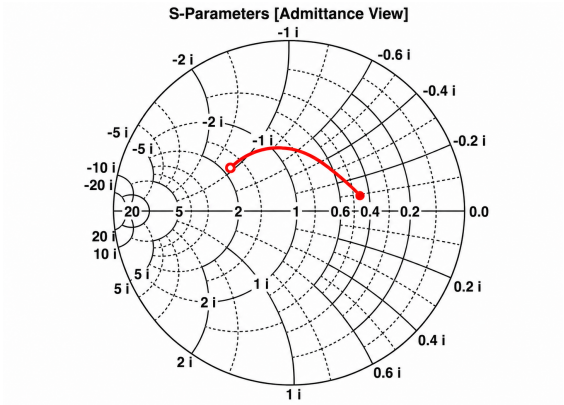


Figure 26. *Smith chart response of the completed 6×6 slotted array in admittance view. This plot directly supports the shunt-admittance interpretation of the complete array response.*

Together, the polar plot, impedance Smith chart, and admittance Smith chart show that the completed array behaves as a frequency-dependent electromagnetic load. The polar plot confirms that the reflected signal changes in both magnitude and phase across the sweep. The impedance Smith chart shows that the input impedance remains displaced from the ideal matched condition, explaining why the simulated return loss is moderate rather than excellent. The admittance Smith chart provides the most useful interpretation for this study, because the complete slot array is being treated as an equivalent shunt admittance.

Therefore, the equivalent-circuit interpretation confirms that the completed 6×6 slot array is capable of radiating as a collective aperture, but that the impedance match is not yet fully optimised. This is consistent with the S_{11} frequency sweep, where the minimum reflection coefficient is usable but not deeply matched. Further improvement would require refinement of the slot offsets, slot lengths, cavity geometry, or feed transition so that Y_{array} moves closer to the matched admittance condition at the intended operating frequency.

c. Frequency Sweep and Far-Field Response
After implementation of the complete 6×6 slot-array geometry, a frequency-domain sweep was performed in CST to evaluate the impedance response and radiation behaviour of the final structure. The sweep was restricted to a narrow band around the intended operating frequency in order to reduce computational cost while still capturing the dominant resonance behaviour of the array. In addition to the input reflection coefficient, S_{11}, and the far-field directivity response, the electric-field distribution across the completed aperture was examined to verify that the slot array was being excited as intended.

Figure 27 shows the electric-field magnitude distribution observed from the upper radiating face of the completed 6×6 array. The field concentration is strongest around the slot apertures, confirming that energy is being coupled from the internal waveguide structure into the radiating slot layer. The field pattern is not perfectly uniform across all elements, which is expected because the array uses non-uniform slot offsets and lengths rather than identical repeated apertures. The stronger field regions near the central elements indicate greater local coupling, while the weaker edge regions are consistent with aperture truncation and reduced excitation near the boundaries of the array.

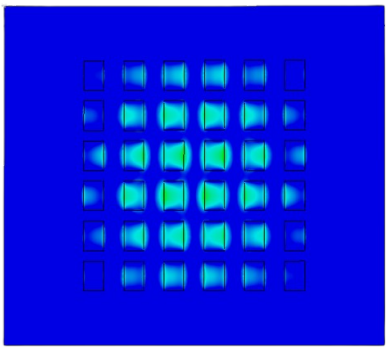


Figure 27. *Top-face electric-field magnitude distribution of the completed* 6×6 *slotted array. The strongest field concentrations occur around the radiating apertures, indicating effective coupling into the upper slot layer.*

Figure 28 shows the corresponding field distribution viewed from the lower coupling-slot side of the structure. The field is strongly concentrated along the central coupling path, indicating that the lower slot arrangement is actively feeding the upper cavity-backed aperture region. The vertically aligned high-field region shows how energy is transferred through the internal coupling structure before being redistributed across the full 6×6 radiating aperture. This result is important because it confirms that the completed geometry is not merely a static slot layout, but an electromagnetically coupled structure in which the lower coupling slots, cavity region, and upper radiating apertures operate together.

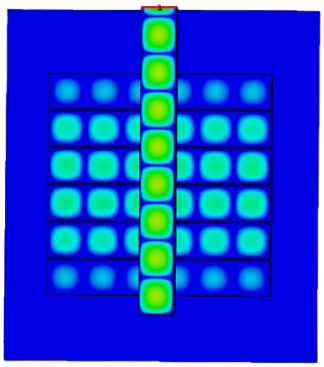


Figure 28. *Bottom-side electric-field magnitude distribution of the completed* 6×6 *array. The central high-field region shows the coupling path feeding the cavity-backed aperture structure.*

The top and bottom field plots provide a qualitative check on the array implementation before examining the global performance metrics. The upper view confirms that the radiating apertures are excited across the array surface, while the lower view shows the internal coupling path that transfers energy into the aperture region. Together, these plots support the interpretation that the final design behaves as a coupled multilayer waveguide aperture rather than as a simple collection of isolated slots. The main quantities extracted from the subsequent simulation were therefore the input reflection coefficient, S_{11}, and the far-field directivity response in the two principal angular cuts.

Figure 29 shows the simulated S_{11} magnitude response of the completed 6×6 slotted waveguide array. The curve exhibits a clear minimum near the centre of the swept band, with the lowest reflection level occurring at approximately 9.03 GHz. The minimum value is approximately -10.5 dB, indicating that the array is reasonably coupled to the waveguide feed at the selected operating frequency. Although this is not an ideal impedance match, it is sufficient to demonstrate that the full-array geometry can be excited and evaluated without severe mismatch. Further optimisation of the slot offsets, slot lengths, cavity dimensions, or feed transition would be required to obtain a deeper return-loss minimum.

The far-field response was then evaluated at 9 GHz using two principal cuts. Figure 30 shows the directivity pattern for the constant-θ cut, where $\theta = 90°$ and the angular variation is plotted with respect to ϕ. The main lobe occurs at $\phi = 90°$, which is consistent with the intended broadside radiation direction. The reported main-lobe magnitude is approximately 0.143 dB, and the 3 dB angular width

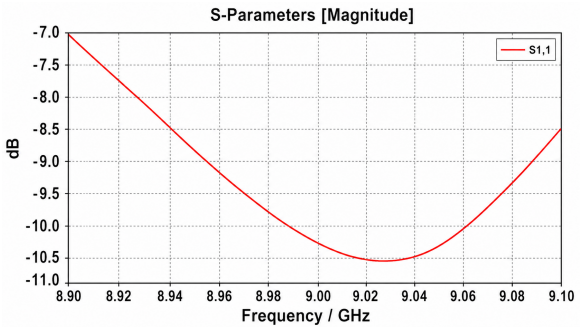


Figure 29. *Simulated S_{11} magnitude response of the completed 6×6 slotted waveguide array. The minimum reflection coefficient occurs near 9.03 GHz, indicating the approximate operating frequency of the array.*

is approximately 14.2°. The sidelobe level in this plane is approximately −23.2 dB, which is below the target suppression benchmark of −20 dB.

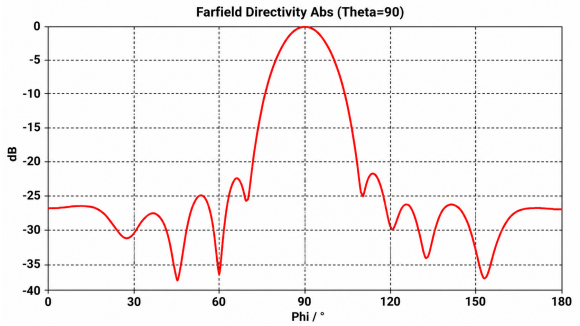


Figure 30. *Far-field directivity response at 9 GHz for the constant-θ cut, where $\theta = 90°$. The plot shows directivity magnitude in dB against ϕ in degrees. The main beam occurs at $\phi = 90°$, with a reported sidelobe level of approximately −23.2 dB.*

Figure 31 shows the corresponding constant-ϕ cut, where $\phi = 90°$ and the angular variation is plotted with respect to θ. In this plane, the main beam is again centred at 90°, confirming that the dominant radiation direction remains aligned with the intended broadside direction. The 3 dB angular width is approximately 13.7°, and the reported sidelobe level is approximately −21.8 dB. This result also satisfies the −20 dB suppression target, although the sidelobe suppression is slightly weaker than that observed in the constant-θ cut.

The two far-field cuts show that the completed array produces a dominant broadside beam in both principal planes. The constant-θ cut gives a stronger sidelobe suppression, with a sidelobe level of approximately −23.2 dB, while the constant-ϕ cut gives a sidelobe level of approximately −21.8 dB. Since both values are below −20 dB, the simulated radiation behaviour satisfies the project objective of suppressing unwanted off-axis radiation to a level significantly below the main beam.

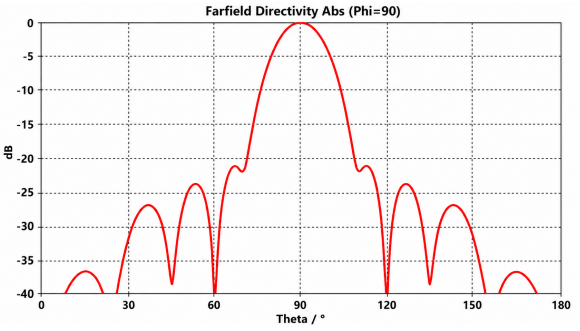


Figure 31. *Far-field directivity response at 9 GHz for the constant-ϕ cut, where $\phi = 90°$. The plot shows directivity magnitude in dB against θ in degrees. The main beam occurs at $\theta = 90°$, with a reported sidelobe level of approximately −21.8 dB.*

Taken together, the frequency sweep and far-field results provide two complementary checks on the final array design. The S_{11} result confirms that the completed slot array remains reasonably coupled to the waveguide feed near 9.03 GHz, while the far-field cuts confirm that the array produces a controlled broadside beam with sidelobes suppressed below the target level in both principal planes. Therefore, the CST results demonstrate that the proposed slot-placement strategy can be implemented at full-array scale and can achieve the intended second-order lobe suppression behaviour, subject to further refinement of the impedance match.

d. Applied-Voltage Matrix Analysis

The applied-voltage response of the final 6×6 slotted array was analysed to evaluate how the implemented cavity-slot and coupling-slot geometry affected the aperture excitation. Since the applied voltage is a complex quantity, the response at each array element was separated into its real and imaginary components. The complex applied voltage at element (i, j) was written as

$$V_{\mathrm{app},i,j} = \mathrm{Re}\{V_{\mathrm{app},i,j}\} + j\,\mathrm{Im}\{V_{\mathrm{app},i,j}\}, \qquad (27)$$

where i and j denote the row and column indices of the 6×6 array. Tables 5 and 6 show the real and imaginary components of the applied-voltage distribution.

The real component shows that the largest positive voltage contribution occurs near the centre of the array, particularly around the central elements. The imaginary component follows a similar spatial trend in magnitude but remains negative across the aperture. Together, these two matrices define the full complex excitation of each slot element.

The applied-voltage magnitude was calculated from the real and imaginary components using

$$|V_{\mathrm{app},i,j}| = \sqrt{\mathrm{Re}\{V_{\mathrm{app},i,j}\}^2 + \mathrm{Im}\{V_{\mathrm{app},i,j}\}^2}. \qquad (28)$$

This magnitude represents the excitation strength of each slot element. Larger values indicate stronger local excitation, while smaller values indicate weaker contribution to the aperture field.

Table 7 shows that the strongest excitation occurs around the centre of the aperture, where the applied-voltage magnitude reaches values close to 11. The outer corner elements are below 2, confirming that the realised aperture excitation is tapered from the centre toward the edges. This type of taper is useful because it reduces abrupt aperture discontinuities and can contribute to lower off-axis radiation.

The phase angle of the applied voltage was calculated from the complex argument,

$$\angle V_{\mathrm{app},i,j} = \operatorname{atan2}\left(\operatorname{Im}\{V_{\mathrm{app},i,j}\}, \operatorname{Re}\{V_{\mathrm{app},i,j}\}\right). \tag{29}$$

The two-argument arctangent was used so that the correct quadrant of the complex voltage was preserved.

Table 8 shows that the applied-voltage phase is not completely uniform across the aperture. The centre elements remain close to approximately $-50°$, while larger deviations appear toward the outer elements. This matters because the far-field pattern depends on both magnitude and phase; large phase imbalance can distort the aperture field and contribute to unwanted lobe formation.

To compare the realised excitation with the intended aperture taper, the magnitude distribution was normalised using the centre-four reference magnitude. Since the array has no single centre element, the four central elements were averaged to form the reference value. The normalised magnitude was calculated as

$$|V_{\mathrm{app},i,j}|_{\mathrm{norm}} = \frac{|V_{\mathrm{app},i,j}|}{\overline{|V_{\mathrm{app}}|}_{\mathrm{c4}}}. \tag{30}$$

Table 9 shows that the centre elements have normalised magnitudes close to unity, as expected from the centre-four reference. The outer rows and columns have much lower normalised values, with the corner elements near 0.16–0.17. This confirms that the realised excitation distribution is strongly tapered from the centre toward the edges.

The normalised applied-voltage distribution was then compared with the intended target excitation profile. The target matrix defines the desired aperture taper used to guide the array synthesis. As shown in Table 10, the target distribution is symmetric about the centre of the array, with maximum excitation at the centre four elements and progressively reduced excitation toward the edges.

To quantify how closely the realised excitation followed the target distribution, an error matrix was calculated as

$$E_{i,j} = |V_{\mathrm{app},i,j}|_{\mathrm{norm}} - T_{i,j}, \tag{31}$$

where $T_{i,j}$ is the target excitation value at element (i, j). Positive values indicate that the realised excitation was higher than the target, while negative values indicate that it was lower.

Table 11 shows that most of the excitation errors remain within a few hundredths of the target values. The largest positive deviations occur in the second and fourth rows, while the largest negative deviation occurs near the central region at element $(3, 3)$. Overall, the small error values indicate that the implemented slot geometry produced an applied-voltage distribution that closely followed the intended target excitation profile.

These results provide an important verification step for the 6×6 array synthesis. The real and imaginary voltage matrices define the complex excitation, the magnitude and phase matrices describe the realised aperture field, and the normalised/error matrices confirm how closely the realised excitation matches the intended taper. This supports the use of the spline-generated cavity-slot dimensions as a practical method for shaping the aperture response and reducing unwanted lobe behaviour.

e. Centre-Four Applied-Voltage Normalisation

The centre-four elements were examined separately because the 6×6 array has no single centre element. The physical centre of the aperture lies between elements $(3, 3)$, $(3, 4)$, $(4, 3)$, and $(4, 4)$. These four elements were therefore used to define the central reference magnitude and phase for the applied-voltage distribution. The complete C++ implementation used for this calculation is provided in Appendix F.

The centre-four applied-voltage magnitude was calculated as

$$\overline{|V_{\mathrm{app}}|}_{\mathrm{c4}} = \frac{1}{4}\big(|V_{\mathrm{app},3,3}| + |V_{\mathrm{app},3,4}| + |V_{\mathrm{app},4,3}| + |V_{\mathrm{app},4,4}|\big). \tag{32}$$

Substituting the calculated values gives

$$\overline{|V_{\mathrm{app}}|}_{\mathrm{c4}} = \frac{1}{4}\big(10.479520 + 10.723351 + 11.076428 + 10.819638\big) = 10.774734. \tag{33}$$

The centre-four phase reference was calculated as

$$\overline{\angle V_{\mathrm{app}_{\mathrm{c4}}}} = \frac{1}{4}\big(\angle V_{\mathrm{app},3,3} + \angle V_{\mathrm{app},3,4} + \angle V_{\mathrm{app},4,3} + \angle V_{\mathrm{app},4,4}\big). \tag{34}$$

This gives

$$\overline{\angle V_{\mathrm{app}_{\mathrm{c4}}}} = \frac{1}{4}\big(-48.09^\circ + (-50.43^\circ) + (-51.38^\circ) + (-49.60^\circ)\big) = -49.88^\circ. \tag{35}$$

The normalised applied-voltage magnitude for each element was calculated using

$$|V_{\mathrm{app},i,j}|_{\mathrm{norm}} = \frac{|V_{\mathrm{app},i,j}|}{\overline{|V_{\mathrm{app}}|}_{\mathrm{c4}}}. \tag{36}$$

For the centre-four elements, this gives

$$\begin{aligned} |V_{\mathrm{app},3,3}|_{\mathrm{norm}} &= \frac{10.479520}{10.774734} = 0.9726, \\ |V_{\mathrm{app},3,4}|_{\mathrm{norm}} &= \frac{10.723351}{10.774734} = 0.9952, \\ |V_{\mathrm{app},4,3}|_{\mathrm{norm}} &= \frac{11.076428}{10.774734} = 1.0280, \\ |V_{\mathrm{app},4,4}|_{\mathrm{norm}} &= \frac{10.819638}{10.774734} = 1.0042. \end{aligned} \tag{37}$$

The phase deviation of each element relative to the centre-four phase reference was calculated as

$$\Delta\phi_{i,j} = \angle V_{\mathrm{app},i,j} - \overline{\angle V_{\mathrm{app}_{\mathrm{c4}}}}. \tag{38}$$

For the centre-four elements, this gives

$$\begin{aligned} \Delta\phi_{3,3} &= -48.09^\circ - (-49.88^\circ) = 1.78^\circ, \\ \Delta\phi_{3,4} &= -50.43^\circ - (-49.88^\circ) = -0.55^\circ, \\ \Delta\phi_{4,3} &= -51.38^\circ - (-49.88^\circ) = -1.50^\circ, \\ \Delta\phi_{4,4} &= -49.60^\circ - (-49.88^\circ) = 0.27^\circ. \end{aligned} \tag{39}$$

The excitation error was calculated by comparing the normalised applied-voltage magnitude with the target excitation matrix:

$$E_{i,j} = |V_{\mathrm{app},i,j}|_{\mathrm{norm}} - T_{i,j}, \tag{40}$$

where $T_{i,j}$ is the target excitation at element (i, j). The maximum absolute error was

$$\max|E_{i,j}| = 0.0465, \tag{41}$$

and the root-mean-square error was calculated using

$$E_{\mathrm{RMS}} = \sqrt{\frac{1}{36}\sum_{i=1}^{6}\sum_{j=1}^{6} E_{i,j}^2} = 0.0262. \tag{42}$$

These results show that the centre-four normalised magnitudes remain close to unity and that the centre-four phase deviations remain close to 0°. The small maximum and RMS errors indicate that the realised applied-voltage distribution closely follows the intended target excitation profile. This verifies that the centre-four reference is suitable for assessing the aperture excitation of the 6 × 6 array.

e. Applied-Voltage Matrix Analysis

The applied-voltage response of the final 6×6 slotted array was analysed to evaluate how the implemented cavity-slot and coupling-slot geometry affected the aperture excitation. Since the applied voltage is a complex quantity, the response at each array element was first separated into its real and imaginary components. The complex applied voltage at element (i, j) was written as

$$V_{\mathrm{app},i,j} = \mathrm{Re}\{V_{\mathrm{app},i,j}\} + j\,\mathrm{Im}\{V_{\mathrm{app},i,j}\}, \tag{43}$$

where i and j denote the row and column indices of the 6 × 6 array. Tables 5 and 6 show the real and imaginary components of the applied-voltage distribution.

Table 5
Real component of the applied-voltage distribution, $\mathrm{Re}\{V_{\mathrm{app}}\}$.

$\mathrm{Re}\{V_{\mathrm{app}}\}$ (Real Part)						
$i\backslash j$	1	2	3	4	5	6
1	1.430680	1.557819	2.190069	1.648017	1.964227	1.225528
2	3.053586	4.102413	5.317674	4.756039	4.456888	2.897924
3	4.015515	5.903867	6.999762	6.831015	5.873717	4.118667
4	4.091945	5.899121	6.913457	7.012372	5.845611	3.975239
5	2.915737	4.466292	4.938300	5.374880	4.122050	3.031380
6	1.241757	1.998119	1.805654	2.340819	1.430327	1.449499

Table 6
Imaginary component of the applied-voltage distribution, $\mathrm{Im}\{V_{\mathrm{app}}\}$.

$\mathrm{Im}\{V_{\mathrm{app}}\}$ (Imaginary Part)						
$i\backslash j$	1	2	3	4	5	6
1	-1.215424	-2.299639	-3.729877	-3.471311	-2.381231	-1.141884
2	-1.974363	-4.400251	-6.255274	-6.779727	-4.039809	-2.160932
3	-2.543347	-5.235148	-7.798953	-8.266045	-5.021496	-2.617474
4	-2.774660	-5.228442	-8.653981	-8.239612	-5.634161	-2.723634
5	-1.999506	-3.785695	-6.293602	-5.877724	-4.209233	-1.941643
6	-1.155136	-2.432653	-3.494322	-3.757526	-2.422456	-1.196527

The real component in Table 5 shows that the largest positive voltage contribution occurs near the centre of the array, particularly around the central elements. The imaginary component in Table 6 follows a similar spatial trend in magnitude but remains negative across the aperture. Together, these two matrices define the full complex excitation of each slot element.

The applied-voltage magnitude was then calculated from the real and imaginary components using

$$|V_{\mathrm{app},i,j}| = \sqrt{\mathrm{Re}\{V_{\mathrm{app},i,j}\}^2 + \mathrm{Im}\{V_{\mathrm{app},i,j}\}^2}. \tag{44}$$

This magnitude represents the excitation strength of each slot element. Larger values indicate stronger local excitation, while smaller values indicate weaker contribution to the aperture field.

Table 7
Applied-voltage magnitude distribution, $|V_{\text{app}}|$.

$|V_{\text{app}}|$ (Magnitude)						
$i\backslash j$	1	2	3	4	5	6
1	1.877259	2.777614	4.325319	3.842650	3.086819	1.675057
2	3.636275	6.015979	8.210122	8.281582	6.015306	3.614912
3	4.753206	7.890654	10.479520	10.723351	7.727611	4.880019
4	4.943961	7.882654	11.076428	10.819638	8.118802	4.818787
5	3.535469	5.854848	7.999765	7.964733	5.891429	3.599895
6	1.695966	3.148060	3.933277	4.427012	2.813206	1.879554

Table 7 shows that the strongest excitation occurs around the centre of the aperture, where the applied-voltage magnitude reaches values close to 11. The outer corner elements are below 2, confirming that the realised aperture excitation is tapered from the centre toward the edges. This type of taper is useful because it reduces abrupt aperture discontinuities and can contribute to lower off-axis radiation.

The phase angle of the applied voltage was calculated from the complex argument,

$$\angle V_{\text{app},i,j} = \operatorname{atan2}\left(\operatorname{Im}\{V_{\text{app},i,j}\}, \operatorname{Re}\{V_{\text{app},i,j}\}\right). \tag{45}$$

The two-argument arctangent was used so that the correct quadrant of the complex voltage was preserved.

Table 8
Applied-voltage phase angle calculated from the complex voltage argument.

Phase Angle $= \arg[\text{Re} + j\,\text{Im}]$ (degrees)						
$i\backslash j$	1	2	3	4	5	6
1	−40.35°	−55.89°	−59.58°	−64.60°	−50.48°	−42.98°
2	−32.89°	−47.01°	−49.63°	−54.95°	−42.19°	−36.71°
3	−32.35°	−41.56°	−48.09°	−50.43°	−40.53°	−32.44°
4	−34.14°	−41.55°	−51.38°	−49.60°	−43.94°	−34.42°
5	−34.44°	−40.29°	−51.88°	−47.56°	−45.60°	−32.64°
6	−42.93°	−50.60°	−62.67°	−58.08°	−59.44°	−39.54°

Table 8 shows that the applied-voltage phase is not completely uniform across the aperture. The centre elements remain close to approximately −50°, while larger deviations appear toward the outer elements. This matters because the far-field pattern depends on both magnitude and phase; large phase imbalance can distort the aperture field and contribute to unwanted lobe formation.

To compare the realised excitation with the intended aperture taper, the magnitude distribution was normalised using the centre-four reference magnitude. Since the array has no single centre element, the four central elements were averaged to form the reference value. The normalised magnitude was calculated as

$$|V_{\text{app},i,j}|_{\text{norm}} = \frac{|V_{\text{app},i,j}|}{|V_{\text{app}}|_{\text{c4}}}. \tag{46}$$

Table 9
Normalised applied-voltage magnitude distribution, $|V_{\text{app}}(m,n)|/|V_{\text{center}}|$.

$|V_{\text{app}}(m,n)|/|V_{\text{center}}|$ (Normalised Magnitude)						
$i\backslash j$	1	2	3	4	5	6
1	0.1742	0.2578	0.4014	0.3566	0.2865	0.1555
2	0.3375	0.5583	0.7620	0.7686	0.5583	0.3355
3	0.4411	0.7323	0.9726	0.9952	0.7172	0.4529
4	0.4588	0.7316	1.0280	1.0042	0.7535	0.4472
5	0.3281	0.5434	0.7425	0.7392	0.5468	0.3341
6	0.1574	0.2922	0.3650	0.4109	0.2611	0.1744

Table 9 shows that the centre elements have normalised magnitudes close to unity, as expected from the centre-four reference. The outer rows and columns have much lower normalised values, with the corner elements near 0.16–0.17. This confirms that the realised excitation distribution is strongly tapered from the centre toward the edges.

The normalised applied-voltage distribution was then compared with the intended target excitation profile. The target matrix defines the desired aperture taper used to guide the array synthesis. As shown in Table 10, the target distribution is symmetric about the centre of the array, with maximum excitation at the centre four elements and progressively reduced excitation toward the edges.

Table 10
Target excitation distribution for the 6×6 array.

Target Excitation						
$i\backslash j$	1	2	3	4	5	6
1	0.1557	0.2715	0.3753	0.3753	0.2715	0.1557
2	0.2996	0.5223	0.7221	0.7221	0.5223	0.2996
3	0.4149	0.7234	1.0000	1.0000	0.7234	0.4149
4	0.4149	0.7234	1.0000	1.0000	0.7234	0.4149
5	0.2996	0.5223	0.7221	0.7221	0.5223	0.2996
6	0.1557	0.2715	0.3753	0.3753	0.2715	0.1557

To quantify how closely the realised excitation followed the target distribution, an error matrix was calculated as

$$E_{i,j} = |V_{\text{app},i,j}|_{\text{norm}} - T_{i,j}, \tag{47}$$

where $T_{i,j}$ is the target excitation value at element (i,j). Positive values indicate that the realised excitation was higher than the target, while negative values indicate that it was lower.

Table 11 shows that most of the excitation errors remain within a few hundredths of the target values. The largest positive deviations occur in

Table 11
Normalised applied-voltage error relative to the target excitation distribution.

Error = Normalised $\lvert V_{\text{app}}\rvert$ − Target						
$i\backslash j$	**1**	**2**	**3**	**4**	**5**	**6**
1	0.0185	−0.0137	0.0261	−0.0187	0.0150	−0.0002
2	0.0379	0.0360	0.0399	0.0465	0.0360	0.0359
3	0.0262	0.0089	−0.0274	−0.0048	−0.0062	0.0380
4	0.0439	0.0082	0.0280	0.0042	0.0301	0.0323
5	0.0285	0.0211	0.0204	0.0171	0.0245	0.0345
6	0.0017	0.0207	−0.0103	0.0356	−0.0104	0.0187

the second and fourth rows, while the largest negative deviation occurs near the central region at element $(3, 3)$. Overall, the small error values indicate that the implemented slot geometry produced an applied-voltage distribution that closely followed the intended target excitation profile.

These results provide an important verification step for the 6×6 array synthesis. The real and imaginary voltage matrices define the complex excitation, the magnitude and phase matrices describe the realised aperture field, and the normalised/error matrices confirm how closely the realised excitation matches the intended taper. This supports the use of the spline-generated cavity-slot dimensions as a practical method for shaping the aperture response and reducing unwanted lobe behaviour.

VI. TARGET ACHIEVEMENTS AND RESEARCH OUTCOMES

The objective of this research was to investigate whether a truncated-waveguide slot-array approach could suppress unwanted second-order lobes while maintaining a controlled main-beam response. This objective was addressed through a staged workflow involving single-slot modelling, self-admittance extraction, spline-based array synthesis, full 6×6 CST implementation, applied-voltage verification, and final radiation-pattern evaluation. The main technical outcomes are summarised in Table 12.

Overall, the project achieved its main technical targets. A single-slot response was successfully converted into a non-uniform 6×6 truncated-waveguide slot array through interpolation, centreline mapping, and CST implementation. The final results show that controlled slot-geometry variation can be used to shape the aperture excitation and reduce unwanted lobe behaviour. This provides a strong numerical foundation for future physical prototyping and experimental validation.

VII. PLA PROTOTYPE REALISATION

After the numerical design and CST verification stages, the array geometry was fabricated as a PLA prototype. The purpose of this prototype was to verify the physical realisation of the 6×6 slot layout before progressing to a conductive metallic version. Since the final array contains non-uniform cavity-slot offsets and lengths, the prototype provided a practical check that the slot distribution could be manufactured and visually inspected as a complete structure.

Table 12
Summary of research targets and achieved outcomes.

Research target	**Achieved outcome**
Single-slot investigation	Cavity-slot offset and length were swept in CST to characterise the slot response.
Self-admittance extraction	S_{11} and S_{21} were converted into $Y_{\text{self}} = G_{\text{self}} + jB_{\text{self}}$ to identify strong and near-resonant slot regions.
Lookup dataset generation	The sweep results were organised into a spline-interpolated design dataset.
6×6 array synthesis	A non-uniform cavity-slot layout was generated for all 36 array elements.
Full CST implementation	The layered truncated-waveguide array was assembled as a complete 3D CST model.
Applied-voltage verification	The realised aperture excitation closely followed the target distribution, with small maximum and RMS error.
Frequency and far-field verification	The final array produced a dominant main beam with reduced off-axis lobe behaviour.



Figure 32. *Top view of the PLA prototype showing the full 6×6 slot arrangement. The prototype was used to verify the physical layout and manufacturability of the slot geometry.*

Figure 32 shows the upper radiating surface of the PLA prototype. The printed model captures the rectangular slot array and confirms that the synthesised slot layout can be transferred from the CST model into a physical geometry. This is an important intermediate step because the design relies on element-specific slot placement rather than identical repeated slots.

The low-angle view in Fig. 33 shows the depth of the slot openings and the layered body of the prototype. This view was useful for checking the physical definition of the slot apertures, the thickness of the top layer, and the overall form of the



Figure 33. *Low-angle view of the PLA prototype showing the slot openings and layered body of the truncated-waveguide structure.*

truncated-waveguide body.



Figure 34. *Front view of the PLA prototype showing the completed printed structure and slot aperture pattern.*

Figure 34 provides a second view of the completed printed structure. Together, the three prototype views confirm that the 6×6 array geometry was physically realisable using additive manufacturing. The PLA model therefore served as a mechanical proof-of-concept for the proposed array.

Although the PLA prototype validates manufacturability and geometry realisation, it does not represent the final electromagnetic prototype. PLA is non-conductive and therefore cannot reproduce the metallic boundary conditions required for waveguide operation. The final validation stage would require a conductive prototype, such as stainless steel or another suitable metal, to measure the return loss and radiation pattern experimentally.

VIII. FUTURE METALLIC PROTOTYPE

The final prototype is intended to be manufactured as a metallic layered waveguide structure, as shown in Fig. 35. The PLA prototype verified the physical geometry, but a metallic version is required for electromagnetic operation because the antenna depends on conductive waveguide boundaries and precisely defined slot apertures.

The exploded assembly shows the main layers required to realise the design. The upper layer contains the 6×6 radiating slot pattern, while the lower layers provide the coupling slots, cavity features, waveguide body, and mechanical support. Accurate alignment between these layers is critical because small fabrication errors may shift the resonance, affect S_{11}, or alter the far-field lobe structure.

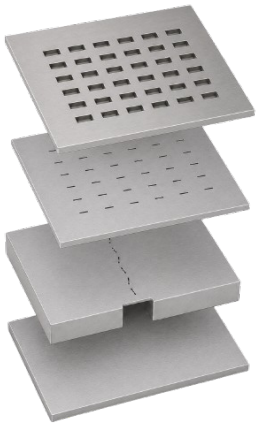


Figure 35. *Conceptual final metallic prototype of the truncated 6×6 slotted waveguide array. The exploded view shows the layered construction of the radiating slot layer, coupling features, cavity region, and base structure.*

The metallic prototype would allow experimental validation of the CST results. This would involve measuring the reflection coefficient, S_{11}, using a vector network analyser, followed by far-field radiation-pattern testing to compare the measured main beam, beamwidth, sidelobe level, and second-order-lobe behaviour against simulation.

The metallic prototype therefore represents the next stage of the project. It would move the work from numerical verification to physical electromagnetic validation.

IX. CONCLUSION AND FUTURE WORK

This research investigated whether a truncated-waveguide slot-array structure could reduce unwanted second-order lobes while maintaining a controlled main-beam response. The work progressed from single-slot CST modelling and self-admittance extraction to spline-based 6×6 array synthesis, full CST implementation, and radiation-pattern evaluation.

The single-slot study showed that cavity-slot offset and length strongly influence the electromagnetic response. The extracted S-parameters were converted into self-admittance terms, G_{self} and B_{self}, which were used to identify suitable slot dimensions for the full array.

Spline interpolation was then used to generate non-uniform cavity-slot offsets and lengths for all 36 array elements. This produced a controlled aperture distribution rather than a repeated uniform slot

geometry. The completed CST model showed a tapered applied-voltage distribution, with stronger excitation near the centre and weaker excitation toward the edges.

The final frequency and far-field results showed a usable impedance match near the operating frequency and a dominant main beam with reduced off-axis radiation. A PLA prototype verified the physical geometry, but electromagnetic validation requires a metallic prototype.

Future work should focus on fabricating a conductive prototype, measuring S_{11} with a vector network analyser, and experimentally validating the far-field pattern. Further optimisation should also consider cavity-slot geometry, coupling-slot geometry, aperture taper, layer alignment, surface roughness, and material conductivity.

Bibliography

[1] C. A. Balanis, *Antenna Theory: Analysis and Design*, 4th ed. Hoboken, NJ, USA: John Wiley & Sons, 2016.

[2] J. L. Volakis, Ed., *Antenna Engineering Handbook*, 4th ed. New York, NY, USA: McGraw-Hill, 2007.

[3] L. Josefsson and S. R. Rengarajan, *Slotted Waveguide Array Antennas: Theory, Analysis and Design*. London, U.K.: IET, 2018, doi: 10.1049/SBEW517E.

[4] H. M. El Misilmani, M. Al-Husseini, and K. Y. Kabalan, "Design of slotted waveguide antennas with low sidelobes for high power microwave applications," *Progress In Electromagnetics Research C*, vol. 56, pp. 15–28, 2015.

[5] P. Delos, B. Broughton, and J. Kraft, "Phased array antenna patterns—Part 2: Grating lobes and beam squint," *Analog Devices Analog Dialogue*, 2020.

[6] Y.-S. Yeoh and K.-S. Min, "Characteristics of 6 × 26 slotted waveguide array antenna for wave monitoring radar system," *Journal of Electromagnetic Engineering and Science*, vol. 21, no. 5, pp. 439–447, Nov. 2021, doi: 10.26866/jees.2021.5.r.53.

[7] B. M. Yousef *et al.*, "Ultra-low SLL slotted waveguide antenna array using groove-gap waveguide technology for millimeter-wave applications," *AEU - International Journal of Electronics and Communications*, 2024.

Appendix A: Data Records for Single Slot Parametric Sweep

Table 13
S-parameter data records for the single-slot parametric sweep.

Run ID	$\Re\{S_{11}\}$	$\Im\{S_{11}\}$	$\Re\{S_{21}\}$	$\Im\{S_{21}\}$
1	-0.001468	0.001917	0.998874	0.000488
2	-0.001697	0.001754	0.998312	0.000078
3	-0.001969	0.001593	0.998051	-0.000075
4	-0.002289	0.001444	0.997730	-0.000189
5	-0.002664	0.001316	0.997348	-0.000256
6	-0.003099	0.001227	0.996908	-0.000264
7	-0.003597	0.001197	0.996414	-0.000201
8	-0.004151	0.001253	0.995870	-0.000051
9	-0.004744	0.001423	0.995283	0.000217
10	-0.005344	0.001733	0.994685	0.000626
11	-0.005902	0.002198	0.994123	0.001201
12	-0.006360	0.002808	0.993664	0.001939
13	-0.006669	0.003529	0.993352	0.002446
14	-0.006791	0.004297	0.993263	0.003522
15	-0.006727	0.005047	0.993339	0.004273
16	-0.006507	0.005719	0.993553	0.004951
17	-0.006176	0.006277	0.993840	0.005369
18	-0.005783	0.006712	0.994235	0.005863
19	-0.005370	0.007031	0.994657	0.006245
20	-0.004972	0.007242	0.995108	0.006619
21	-0.004691	0.007397	0.995227	0.006908
22	-0.002523	-0.000244	0.997355	-0.001993
23	-0.002929	-0.000529	0.996906	-0.002236
24	-0.003402	-0.000798	0.996417	-0.002510
25	-0.003958	-0.001046	0.995985	-0.002630
26	-0.004612	-0.001258	0.995328	-0.002827
27	-0.005371	-0.001406	0.994568	-0.002956
28	-0.006241	-0.001453	0.993701	-0.002980
29	-0.007211	-0.001354	0.992736	-0.002852
30	-0.008253	-0.001057	0.991700	-0.002523
31	-0.009313	-0.000518	0.990647	-0.001946
32	-0.010310	0.000292	0.989658	-0.001095
33	-0.011143	0.001362	0.988828	0.000020
34	-0.011719	0.002631	0.988259	0.001337
35	-0.011975	0.003999	0.988011	0.002755
36	-0.011905	0.005347	0.988089	0.004156
37	-0.011555	0.006572	0.988444	0.005434
38	-0.011000	0.007607	0.988995	0.006523
39	-0.010327	0.008428	0.989654	0.007396
40	-0.009608	0.009044	0.990402	0.008137
41	-0.008902	0.009477	0.991095	0.008613
42	-0.008403	0.009839	0.991583	0.008916
43	-0.003908	-0.002826	0.995884	-0.004577
44	-0.004523	-0.003254	0.995364	-0.005012
45	-0.005244	-0.003655	0.994666	-0.005397
46	-0.006092	-0.004027	0.993836	-0.005754
47	-0.007088	-0.004340	0.992857	-0.006059
48	-0.008243	-0.004556	0.991712	-0.006273
49	-0.009564	-0.004622	0.990387	-0.006339

Continued on next page

Table 13
S-parameter data records for the single-slot parametric sweep. continued.

Run ID	$\Re\{S_{11}\}$	$\Im\{S_{11}\}$	$\Re\{S_{21}\}$	$\Im\{S_{21}\}$
50	-0.011037	-0.004469	0.988890	-0.006183
51	-0.012623	-0.004024	0.987262	-0.005723
52	-0.014243	-0.003216	0.985588	-0.004881
53	-0.015771	-0.001996	0.984113	-0.003373
54	-0.017073	-0.000389	0.982787	-0.001708
55	-0.018002	0.001533	0.981835	0.000269
56	-0.018458	0.003624	0.981351	0.002409
57	-0.018420	0.005709	0.981575	0.004396
58	-0.017946	0.007628	0.982059	0.006353
59	-0.017146	0.009273	0.982872	0.008033
60	-0.016147	0.010597	0.983883	0.009388
61	-0.015066	0.011606	0.984726	0.010440
62	-0.013989	0.012338	0.985844	0.011225
63	-0.013481	0.012856	0.986514	0.011920
64	-0.005543	-0.005990	0.994561	-0.007829
65	-0.006408	-0.006585	0.993730	-0.008360
66	-0.007421	-0.007152	0.992743	-0.008911
67	-0.008610	-0.007676	0.991595	-0.009409
68	-0.010005	-0.008121	0.990119	-0.009852
69	-0.011620	-0.008433	0.988523	-0.010133
70	-0.013466	-0.008538	0.986623	-0.010179
71	-0.015530	-0.008349	0.984577	-0.009948
72	-0.017758	-0.007760	0.982256	-0.009404
73	-0.020042	-0.006679	0.980097	-0.008295
74	-0.022235	-0.005033	0.977882	-0.006648
75	-0.024133	-0.002830	0.975963	-0.004437
76	-0.025535	-0.000167	0.974543	-0.001758
77	-0.026295	0.002764	0.973772	0.001198
78	-0.026365	0.005729	0.973698	0.004196
79	-0.025809	0.008499	0.974259	0.007002
80	-0.024769	0.010911	0.975310	0.009446
81	-0.023417	0.012886	0.976670	0.011448
82	-0.021917	0.014421	0.978175	0.013121
83	-0.020408	0.015539	0.979635	0.014183
84	-0.019770	0.016228	0.980236	0.015001
85	-0.007370	-0.009632	0.992588	-0.011614
86	-0.008493	-0.010414	0.991462	-0.012345
87	-0.009827	-0.011167	0.990136	-0.013072
88	-0.011389	-0.011866	0.988571	-0.013767
89	-0.013214	-0.012465	0.986733	-0.014363
90	-0.015328	-0.012899	0.984597	-0.014788
91	-0.017744	-0.013076	0.982153	-0.014950
92	-0.020446	-0.012881	0.979420	-0.014735
93	-0.023367	-0.012175	0.976475	-0.013918
94	-0.026403	-0.010845	0.973430	-0.012548
95	-0.029351	-0.008791	0.970479	-0.010454
96	-0.031961	-0.006009	0.967869	-0.007621
97	-0.033978	-0.002580	0.965854	-0.004153
98	-0.035186	0.001261	0.964647	-0.000279
99	-0.035491	0.005208	0.964500	0.003550
100	-0.034955	0.008968	0.965054	0.007345
101	-0.033735	0.012305	0.966355	0.010761

Continued on next page

Table 13
S-parameter data records for the single-slot parametric sweep. continued.

Run ID	$\Re\{S_{11}\}$	$\Im\{S_{11}\}$	$\Re\{S_{21}\}$	$\Im\{S_{21}\}$
102	-0.032057	0.015087	0.967928	0.013545
103	-0.030131	0.017291	0.969822	0.015779
104	-0.028130	0.018961	0.971853	0.017414
105	-0.027136	0.020093	0.972789	0.018618
106	-0.009428	-0.013706	0.990608	-0.015933
107	-0.010844	-0.014653	0.989205	-0.016790
108	-0.012519	-0.015592	0.987536	-0.017672
109	-0.014477	-0.016473	0.985617	-0.018478
110	-0.016760	-0.017236	0.983250	-0.019236
111	-0.019401	-0.017800	0.980580	-0.019780
112	-0.022414	-0.018058	0.977634	-0.019972
113	-0.025790	-0.017871	0.974251	-0.019795
114	-0.029459	-0.017080	0.970583	-0.019016
115	-0.033288	-0.015527	0.966756	-0.017471
116	-0.037052	-0.013089	0.962992	-0.015038
117	-0.040461	-0.009725	0.959585	-0.011676
118	-0.043182	-0.005547	0.956860	-0.007495
119	-0.044949	-0.000795	0.955088	-0.002734
120	-0.045621	0.004171	0.954417	0.002244
121	-0.045222	0.008995	0.954824	0.007088
122	-0.043924	0.013361	0.956144	0.011492
123	-0.041980	0.017080	0.958089	0.015304
124	-0.039664	0.020084	0.960345	0.018318
125	-0.037189	0.022406	0.962869	0.020609
126	-0.036082	0.023839	0.963926	0.022062
127	-0.011636	-0.018185	0.988265	-0.020583
128	-0.013376	-0.019369	0.986621	-0.021683
129	-0.015415	-0.020535	0.984578	-0.022836
130	-0.017789	-0.021630	0.982190	-0.023980
131	-0.020554	-0.022587	0.979409	-0.024915
132	-0.023746	-0.023316	0.976193	-0.025619
133	-0.027389	-0.023692	0.972523	-0.025968
134	-0.031471	-0.023556	0.968415	-0.025805
135	-0.035928	-0.022725	0.963937	-0.024948
136	-0.040612	-0.021003	0.959304	-0.023154
137	-0.045273	-0.018245	0.954640	-0.020374
138	-0.049581	-0.014380	0.950331	-0.016490
139	-0.053158	-0.009491	0.946866	-0.011612
140	-0.055663	-0.003827	0.944373	-0.005943
141	-0.056884	0.002222	0.943164	0.000105
142	-0.056800	0.008218	0.943189	0.006188
143	-0.055565	0.013762	0.944430	0.011749
144	-0.053459	0.018590	0.946585	0.016541
145	-0.050800	0.022582	0.949251	0.020533
146	-0.047884	0.025721	0.952140	0.023688
147	-0.046522	0.027559	0.953442	0.025585
148	-0.014006	-0.022873	0.985879	-0.025540
149	-0.016059	-0.024318	0.983834	-0.026896
150	-0.018476	-0.025716	0.981406	-0.028283
151	-0.021285	-0.027027	0.978583	-0.029582
152	-0.024542	-0.028183	0.975312	-0.030726
153	-0.028294	-0.029081	0.971545	-0.031613

Continued on next page

Table 13
S-parameter data records for the single-slot parametric sweep. continued.

Run ID	$\Re\{S_{11}\}$	$\Im\{S_{11}\}$	$\Re\{S_{21}\}$	$\Im\{S_{21}\}$
154	-0.032571	-0.029581	0.967255	-0.032102
155	-0.037364	-0.029504	0.962466	-0.031894
156	-0.042607	-0.028648	0.957222	-0.031015
157	-0.048146	-0.026791	0.951822	-0.029103
158	-0.053709	-0.023753	0.946278	-0.026051
159	-0.058943	-0.019433	0.941067	-0.021720
160	-0.063419	-0.013892	0.936618	-0.016171
161	-0.066737	-0.007367	0.933201	-0.009669
162	-0.068610	-0.000281	0.931339	-0.002572
163	-0.068958	0.006873	0.930979	0.004543
164	-0.067911	0.013627	0.932057	0.011339
165	-0.065756	0.019630	0.934190	0.017284
166	-0.062848	0.024696	0.937209	0.022341
167	-0.059562	0.028756	0.940435	0.026391
168	-0.058260	0.031073	0.941616	0.028698
169	-0.016559	-0.027922	0.983433	-0.030691
170	-0.018962	-0.029588	0.981034	-0.032322
171	-0.021747	-0.031205	0.978247	-0.033930
172	-0.024978	-0.032731	0.975014	-0.035451
173	-0.028714	-0.034091	0.971271	-0.036805
174	-0.033011	-0.035171	0.966966	-0.037882
175	-0.037903	-0.035822	0.962065	-0.038530
176	-0.043383	-0.035850	0.956576	-0.038558
177	-0.049400	-0.035026	0.950633	-0.037730
178	-0.055793	-0.033111	0.944238	-0.035822
179	-0.062290	-0.029886	0.937739	-0.032608
180	-0.068506	-0.025222	0.931521	-0.027957
181	-0.073985	-0.019136	0.926038	-0.021958
182	-0.078256	-0.011852	0.921755	-0.014689
183	-0.080965	-0.003783	0.919033	-0.006632
184	-0.081955	0.004536	0.918035	0.001674
185	-0.081300	0.012562	0.918693	0.009712
186	-0.079273	0.019857	0.920719	0.017072
187	-0.076253	0.026149	0.923684	0.023271
188	-0.072628	0.031365	0.927299	0.028525
189	-0.071151	0.034246	0.928839	0.031417
190	-0.019120	-0.033225	0.980875	-0.036174
191	-0.021827	-0.035141	0.978146	-0.038096
192	-0.024976	-0.037007	0.974990	-0.039965
193	-0.028615	-0.038776	0.971343	-0.041742
194	-0.032812	-0.040368	0.967140	-0.043343
195	-0.037627	-0.041666	0.962319	-0.044651
196	-0.043100	-0.042511	0.956840	-0.045507
197	-0.049237	-0.042703	0.950698	-0.045711
198	-0.055977	-0.042003	0.943954	-0.045024
199	-0.063191	-0.040143	0.936826	-0.043140
200	-0.070594	-0.036889	0.929425	-0.039900
201	-0.077822	-0.032058	0.922197	-0.035083
202	-0.084375	-0.025635	0.915645	-0.028674
203	-0.089752	-0.017790	0.910303	-0.020888
204	-0.093518	-0.008910	0.906540	-0.012015
205	-0.095430	0.000466	0.904573	-0.002589

Continued on next page

Table 13
S-parameter data records for the single-slot parametric sweep. continued.

Run ID	$\Re\{S_{11}\}$	$\Im\{S_{11}\}$	$\Re\{S_{21}\}$	$\Im\{S_{21}\}$
206	-0.095478	0.009736	0.904528	0.006691
207	-0.093883	0.018387	0.906110	0.015217
208	-0.091014	0.026041	0.908995	0.022836
209	-0.087332	0.032471	0.912652	0.029365
210	-0.085707	0.036152	0.914253	0.033022
211	-0.021905	-0.038869	0.977983	-0.042092
212	-0.024939	-0.041023	0.974960	-0.044212
213	-0.028465	-0.043114	0.971430	-0.046314
214	-0.032534	-0.045106	0.967359	-0.048317
215	-0.037215	-0.046912	0.962675	-0.050135
216	-0.042580	-0.048407	0.957309	-0.051644
217	-0.048666	-0.049420	0.951220	-0.052670
218	-0.055487	-0.049740	0.944399	-0.053004
219	-0.062994	-0.049107	0.936997	-0.052343
220	-0.071038	-0.047247	0.928958	-0.050501
221	-0.079351	-0.043894	0.920652	-0.047164
222	-0.087546	-0.038846	0.912468	-0.042131
223	-0.095124	-0.032042	0.904910	-0.035427
224	-0.101534	-0.023622	0.898520	-0.027025
225	-0.106293	-0.013944	0.893702	-0.017308
226	-0.109079	-0.003565	0.890866	-0.006998
227	-0.109813	0.006892	0.890075	0.003392
228	-0.108665	0.016825	0.891309	0.013259
229	-0.105992	0.025791	0.893960	0.022212
230	-0.102294	0.033442	0.897614	0.029864
231	-0.101082	0.037338	0.898877	0.033804
232	-0.024578	-0.044446	0.975491	-0.047846
233	-0.027900	-0.046818	0.972162	-0.050201
234	-0.031745	-0.049148	0.968292	-0.052588
235	-0.036168	-0.051378	0.963825	-0.054845
236	-0.041244	-0.053422	0.958742	-0.056914
237	-0.047039	-0.055153	0.952984	-0.058655
238	-0.053607	-0.056401	0.946382	-0.059879
239	-0.060967	-0.056955	0.939019	-0.060484
240	-0.069076	-0.056557	0.930912	-0.060128
241	-0.077817	-0.054920	0.922174	-0.058525
242	-0.086940	-0.051758	0.913056	-0.055399
243	-0.096078	-0.046840	0.903924	-0.050516
244	-0.104752	-0.040040	0.895254	-0.043750
245	-0.112380	-0.031452	0.887632	-0.035197
246	-0.118440	-0.021361	0.881598	-0.025209
247	-0.122518	-0.010271	0.877528	-0.014159
248	-0.124435	0.001193	0.875545	-0.002654
249	-0.124257	0.012376	0.875710	0.008465
250	-0.122277	0.022742	0.877725	0.018777
251	-0.118954	0.031848	0.881008	0.027882
252	-0.117247	0.037427	0.882718	0.033441
253	-0.027464	-0.050388	0.972446	-0.054111
254	-0.031151	-0.053004	0.968789	-0.056753
255	-0.035373	-0.055561	0.964569	-0.059343
256	-0.040204	-0.058016	0.959736	-0.061831
257	-0.045727	-0.060276	0.954211	-0.064127

Continued on next page

Table 13
S-parameter data records for the single-slot parametric sweep. continued.

Run ID	$\Re\{S_{11}\}$	$\Im\{S_{11}\}$	$\Re\{S_{21}\}$	$\Im\{S_{21}\}$
258	-0.052015	-0.062212	0.947920	-0.066098
259	-0.059119	-0.063649	0.940812	-0.067574
260	-0.067070	-0.064373	0.932858	-0.068337
261	-0.075840	-0.064116	0.924101	-0.068066
262	-0.085303	-0.062590	0.914640	-0.066579
263	-0.095222	-0.059497	0.904724	-0.063524
264	-0.105247	-0.054582	0.894784	-0.058679
265	-0.114899	-0.047691	0.885138	-0.051839
266	-0.123597	-0.038866	0.876448	-0.043069
267	-0.130784	-0.028348	0.869269	-0.032608
268	-0.136001	-0.016591	0.864003	-0.020894
269	-0.138971	-0.004234	0.861032	-0.008591
270	-0.139690	0.008055	0.860222	0.003709
271	-0.138387	0.019684	0.861595	0.015215
272	-0.135465	0.030217	0.864523	0.025686
273	-0.134069	0.036127	0.865894	0.031645
274	-0.030156	-0.056123	0.969857	-0.060067
275	-0.034086	-0.058968	0.965901	-0.062944
276	-0.038584	-0.061749	0.961400	-0.065768
277	-0.043723	-0.064433	0.956258	-0.068498
278	-0.049582	-0.066929	0.950397	-0.071041
279	-0.056235	-0.069108	0.943741	-0.073270
280	-0.063745	-0.070802	0.936229	-0.075014
281	-0.072137	-0.071796	0.927834	-0.076062
282	-0.081387	-0.071836	0.918581	-0.076156
283	-0.091444	-0.070621	0.908522	-0.074992
284	-0.102045	-0.067853	0.897918	-0.072281
285	-0.112885	-0.063254	0.887160	-0.067749
286	-0.123504	-0.056641	0.876542	-0.061200
287	-0.133359	-0.047979	0.866690	-0.052602
288	-0.141872	-0.037429	0.858175	-0.042142
289	-0.148509	-0.025402	0.851535	-0.030158
290	-0.152937	-0.012431	0.847081	-0.017185
291	-0.155023	0.000797	0.844980	-0.004102
292	-0.154882	0.013640	0.845120	0.008740
293	-0.152862	0.025495	0.847152	0.020507
294	-0.151178	0.033522	0.848864	0.028575
295	-0.033014	-0.062023	0.966987	-0.066278
296	-0.037263	-0.065087	0.962729	-0.069383
297	-0.042078	-0.068086	0.957909	-0.072436
298	-0.047554	-0.070982	0.952431	-0.075390
299	-0.053775	-0.073686	0.946208	-0.078154
300	-0.060818	-0.076072	0.939164	-0.080602
301	-0.068744	-0.077972	0.931235	-0.082566
302	-0.077588	-0.079176	0.922388	-0.083836
303	-0.087376	-0.079427	0.912602	-0.084156
304	-0.097964	-0.078437	0.902009	-0.083233
305	-0.109188	-0.075896	0.890852	-0.080721
306	-0.120745	-0.071521	0.879297	-0.076419
307	-0.132210	-0.065100	0.867833	-0.070073
308	-0.143056	-0.056557	0.857035	-0.061644
309	-0.152692	-0.045995	0.847366	-0.051135

Continued on next page

Table 13
S-parameter data records for the single-slot parametric sweep. continued.

Run ID	$\Re\{S_{11}\}$	$\Im\{S_{11}\}$	$\Re\{S_{21}\}$	$\Im\{S_{21}\}$
310	-0.160583	-0.033739	0.839415	-0.038952
311	-0.166298	-0.020320	0.833692	-0.025604
312	-0.169638	-0.006379	0.830354	-0.011803
313	-0.170630	0.007404	0.829400	0.001902
314	-0.169566	0.020326	0.830432	0.014805
315	-0.168423	0.029387	0.831551	0.023791
316	-0.035910	-0.068169	0.963945	-0.072512
317	-0.040469	-0.071451	0.959465	-0.075914
318	-0.045610	-0.074667	0.954320	-0.079187
319	-0.051439	-0.077774	0.948430	-0.082363
320	-0.058043	-0.080688	0.941825	-0.085318
321	-0.065502	-0.083278	0.934388	-0.087961
322	-0.073877	-0.085376	0.926016	-0.090125
323	-0.083206	-0.086772	0.916688	-0.091590
324	-0.093478	-0.087213	0.906419	-0.092101
325	-0.104623	-0.086417	0.895273	-0.091368
326	-0.116462	-0.084067	0.883439	-0.089085
327	-0.128712	-0.079874	0.871196	-0.084960
328	-0.140968	-0.073612	0.858951	-0.078767
329	-0.152749	-0.065138	0.847187	-0.070378
330	-0.163425	-0.054560	0.836530	-0.059883
331	-0.172453	-0.042143	0.827568	-0.047617
332	-0.179364	-0.028358	0.820679	-0.033928
333	-0.183886	-0.013824	0.816127	-0.019412
334	-0.185993	0.000777	0.814049	-0.004966
335	-0.185864	0.014806	0.814171	0.008978
336	-0.185428	0.024078	0.814503	0.018068
337	-0.038917	-0.074105	0.961040	-0.078811
338	-0.043739	-0.077581	0.956199	-0.082403
339	-0.049168	-0.080979	0.950766	-0.085883
340	-0.055304	-0.084272	0.944626	-0.089256
341	-0.062233	-0.087368	0.937692	-0.092433
342	-0.070035	-0.090139	0.929886	-0.095287
343	-0.078779	-0.092412	0.921173	-0.097600
344	-0.088491	-0.093998	0.911461	-0.099270
345	-0.099174	-0.094643	0.900777	-0.100000
346	-0.110756	-0.094063	0.889194	-0.099505
347	-0.123084	-0.091959	0.876865	-0.097487
348	-0.135916	-0.088029	0.864074	-0.093688
349	-0.148876	-0.082038	0.851107	-0.087783
350	-0.161446	-0.073843	0.838538	-0.079674
351	-0.173074	-0.063467	0.826859	-0.069363
352	-0.183194	-0.051135	0.816743	-0.057114
353	-0.191328	-0.037252	0.808631	-0.043397
354	-0.197137	-0.022397	0.802822	-0.028647
355	-0.200506	-0.007214	0.799448	-0.013554
356	-0.201561	0.007559	0.798409	0.001111
357	-0.201889	0.017161	0.798134	0.010483
358	-0.041817	-0.080109	0.958051	-0.085097
359	-0.046898	-0.083736	0.953005	-0.088826
360	-0.052601	-0.087322	0.947307	-0.092500
361	-0.059024	-0.090803	0.940882	-0.096068

Continued on next page

Table 13
S-parameter data records for the single-slot parametric sweep. continued.

Run ID	$\Re\{S_{11}\}$	$\Im\{S_{11}\}$	$\Re\{S_{21}\}$	$\Im\{S_{21}\}$
362	-0.066258	-0.094086	0.933646	-0.099439
363	-0.074379	-0.097046	0.925522	-0.102487
364	-0.083452	-0.099520	0.916448	-0.105052
365	-0.093514	-0.101308	0.906384	-0.106932
366	-0.104562	-0.102170	0.895335	-0.107887
367	-0.116543	-0.101832	0.883352	-0.107644
368	-0.129355	-0.099987	0.870546	-0.105903
369	-0.142701	-0.096358	0.857274	-0.102406
370	-0.156232	-0.090703	0.843753	-0.096843
371	-0.169515	-0.082852	0.830411	-0.089118
372	-0.182016	-0.072794	0.817857	-0.079164
373	-0.193186	-0.060687	0.806792	-0.067208
374	-0.202507	-0.046885	0.797481	-0.053529
375	-0.209610	-0.031903	0.790390	-0.038675
376	-0.214307	-0.016361	0.785673	-0.023203
377	-0.216643	-0.000895	0.783374	-0.007888
378	-0.217846	0.008395	0.782123	0.001259
379	-0.044613	-0.085773	0.955361	-0.091200
380	-0.049872	-0.089609	0.950060	-0.095108
381	-0.055805	-0.093378	0.944116	-0.098970
382	-0.062477	-0.097037	0.937438	-0.102727
383	-0.069971	-0.100499	0.929940	-0.106291
384	-0.078369	-0.103645	0.921537	-0.109540
385	-0.087723	-0.106313	0.912178	-0.112315
386	-0.098088	-0.108310	0.901810	-0.114421
387	-0.109447	-0.109407	0.890446	-0.115625
388	-0.121772	-0.109336	0.878117	-0.115666
389	-0.134921	-0.107811	0.864966	-0.114256
390	-0.148693	-0.104546	0.851290	-0.111083
391	-0.162753	-0.099293	0.837233	-0.105950
392	-0.176685	-0.091877	0.823306	-0.098654
393	-0.189991	-0.082245	0.810009	-0.089187
394	-0.202127	-0.070502	0.797834	-0.077549
395	-0.212588	-0.056944	0.787396	-0.064109
396	-0.220959	-0.042034	0.779026	-0.049329
397	-0.227001	-0.026349	0.772929	-0.033778
398	-0.230676	-0.010592	0.769313	-0.018159
399	-0.232752	-0.000386	0.767243	-0.008117
400	-0.047493	-0.091677	0.952416	-0.097362
401	-0.053072	-0.095677	0.946849	-0.101451
402	-0.059280	-0.099619	0.940633	-0.105494
403	-0.066234	-0.103445	0.933671	-0.109426
404	-0.074022	-0.107069	0.925877	-0.113161
405	-0.082718	-0.110371	0.917174	-0.116579
406	-0.092382	-0.113196	0.907505	-0.119523
407	-0.103058	-0.115356	0.896822	-0.121806
408	-0.114754	-0.116622	0.885159	-0.123153
409	-0.127416	-0.116742	0.872492	-0.123391
410	-0.140928	-0.115438	0.858976	-0.122207
411	-0.155078	-0.112441	0.844878	-0.119345
412	-0.169621	-0.107473	0.830342	-0.114509
413	-0.184131	-0.100355	0.815846	-0.107537

Continued on next page

Table 13
S-parameter data records for the single-slot parametric sweep. continued.

Run ID	$\Re\{S_{11}\}$	$\Im\{S_{11}\}$	$\Re\{S_{21}\}$	$\Im\{S_{21}\}$
414	-0.198113	-0.091033	0.801819	-0.098370
415	-0.211054	-0.079582	0.788888	-0.087023
416	-0.222453	-0.066246	0.777533	-0.073873
417	-0.231890	-0.051427	0.768080	-0.059200
418	-0.239081	-0.035667	0.760917	-0.043564
419	-0.243861	-0.019877	0.756140	-0.027895
420	-0.246782	-0.009264	0.753203	-0.017558
421	-0.050031	-0.097198	0.949859	-0.103197
422	-0.055780	-0.101346	0.944134	-0.107482
423	-0.062183	-0.105445	0.937731	-0.111704
424	-0.069333	-0.109433	0.930578	-0.115816
425	-0.077319	-0.113227	0.922590	-0.119736
426	-0.086215	-0.116710	0.913691	-0.123349
427	-0.096084	-0.119727	0.903810	-0.126451
428	-0.106961	-0.122108	0.892931	-0.128962
429	-0.118871	-0.123632	0.881064	-0.130587
430	-0.131764	-0.124060	0.868169	-0.131145
431	-0.145536	-0.123112	0.854412	-0.130336
432	-0.160010	-0.120524	0.839910	-0.127921
433	-0.174961	-0.116023	0.824963	-0.123576
434	-0.189950	-0.109452	0.809976	-0.117161
435	-0.204566	-0.100700	0.795309	-0.108541
436	-0.218312	-0.089813	0.781559	-0.097802
437	-0.230701	-0.076976	0.769164	-0.085114
438	-0.241306	-0.062540	0.758666	-0.070911
439	-0.249803	-0.046958	0.750168	-0.055487
440	-0.255993	-0.030916	0.743993	-0.039587
441	-0.259681	-0.019081	0.740293	-0.027936
442	-0.052642	-0.102563	0.947334	-0.108835
443	-0.058525	-0.106845	0.941453	-0.113245
444	-0.065119	-0.111093	0.934861	-0.117626
445	-0.072481	-0.115238	0.927499	-0.121909
446	-0.080688	-0.119191	0.919291	-0.126002
447	-0.089809	-0.122838	0.910168	-0.129792
448	-0.099920	-0.126031	0.900092	-0.133109
449	-0.111041	-0.128595	0.888972	-0.135822
450	-0.123184	-0.130319	0.876828	-0.137700
451	-0.136315	-0.130969	0.863698	-0.138505
452	-0.150374	-0.130288	0.849638	-0.137979
453	-0.165161	-0.128015	0.834871	-0.135887
454	-0.180417	-0.123898	0.819615	-0.131938
455	-0.195813	-0.117753	0.804220	-0.125963
456	-0.210943	-0.109463	0.789016	-0.117807
457	-0.225333	-0.099051	0.774614	-0.107561
458	-0.238515	-0.086663	0.761477	-0.095383
459	-0.250048	-0.072603	0.749966	-0.081472
460	-0.259593	-0.057315	0.740370	-0.066345
461	-0.266968	-0.041303	0.733014	-0.050539
462	-0.271531	-0.029647	0.728451	-0.039014
463	-0.055039	-0.107744	0.944952	-0.114288
464	-0.061130	-0.112243	0.938824	-0.118906
465	-0.067962	-0.116679	0.931982	-0.123482

Continued on next page

Table 13
S-parameter data records for the single-slot parametric sweep. continued.

Run ID	$\Re\{S_{11}\}$	$\Im\{S_{11}\}$	$\Re\{S_{21}\}$	$\Im\{S_{21}\}$
466	-0.075571	-0.121001	0.924365	-0.127949
467	-0.084036	-0.125126	0.915894	-0.132222
468	-0.093432	-0.128941	0.906492	-0.136188
469	-0.103818	-0.132301	0.896102	-0.139702
470	-0.115225	-0.135031	0.884689	-0.142589
471	-0.127675	-0.136920	0.872279	-0.144622
472	-0.141140	-0.137756	0.858807	-0.145613
473	-0.155502	-0.137269	0.844443	-0.145283
474	-0.170609	-0.135210	0.829336	-0.143383
475	-0.186222	-0.131345	0.813723	-0.139716
476	-0.202020	-0.125483	0.797928	-0.134023
477	-0.217614	-0.117510	0.782319	-0.126191
478	-0.232552	-0.107427	0.767385	-0.116276
479	-0.246451	-0.095304	0.753489	-0.104322
480	-0.258749	-0.081503	0.741187	-0.090741
481	-0.269144	-0.066408	0.730777	-0.075850
482	-0.277475	-0.050396	0.722469	-0.060011
483	-0.282782	-0.038976	0.717187	-0.048749

Table 14
Integrated electric-field curve data records for the single-slot parametric sweep.

Run ID	$\Re\{E_1\}$	$\Im\{E_1\}$	$\Re\{E_2\}$	$\Im\{E_2\}$
1	1.615602	-0.873146	1.102684	-1.400963
2	1.687433	-1.006138	1.119636	-1.555306
3	1.760552	-1.161350	1.128111	-1.728658
4	1.826035	-1.343657	1.118863	-1.924036
5	1.879795	-1.558604	1.084480	-2.142134
6	1.906007	-1.803057	1.015731	-2.381997
7	1.900973	-2.084588	0.901482	-2.639228
8	1.842792	-2.391926	0.729691	-2.905185
9	1.720694	-2.721153	0.489108	-3.164056
10	1.519988	-3.052005	0.174755	-3.392331
11	1.231024	-3.352812	-0.209808	-3.562516
12	0.862429	-3.596406	-0.646452	-3.646839
13	0.435311	-3.748296	-1.103757	-3.622083
14	-0.015704	-3.798777	-1.541866	-3.496388
15	-0.451352	-3.743595	-1.925919	-3.276829
16	-0.839132	-3.601267	-2.232139	-2.995064
17	-1.157269	-3.398814	-2.450768	-2.683300
18	-1.408142	-3.166228	-2.594578	-2.370259
19	-1.593119	-2.924821	-2.673677	-2.074357
20	-1.725450	-2.692017	-2.706691	-1.807505
21	-1.813155	-2.535922	-2.716083	-1.615180
22	2.152842	-1.160804	1.461177	-1.853554
23	2.254706	-1.332726	1.490880	-2.053222
24	2.355148	-1.538514	1.503522	-2.280101
25	2.443909	-1.779191	1.493239	-2.536667
26	2.511583	-2.058249	1.450530	-2.823334
27	2.552503	-2.383351	1.363541	-3.139056
28	2.547860	-2.753207	1.217382	-3.478654
29	2.478646	-3.162801	0.996461	-3.830424
30	2.324062	-3.599074	0.686491	-4.174211
31	2.065595	-4.038038	0.279537	-4.480798
32	1.693546	-4.444541	-0.219942	-4.713956
33	1.213678	-4.776982	-0.790717	-4.837503
34	0.654179	-4.995867	-1.391577	-4.825454
35	0.059025	-5.078520	-1.972754	-4.672800
36	-0.521743	-5.020837	-2.487783	-4.398134
37	-1.044685	-4.847242	-2.904615	-4.037495
38	-1.483487	-4.591320	-3.211880	-3.632628
39	-1.829055	-4.288664	-3.415432	-3.220713
40	-2.086270	-3.969975	-3.531913	-2.827603
41	-2.269454	-3.658717	-3.581561	-2.470243
42	-2.416653	-3.461804	-3.594611	-2.201962
43	2.688569	-1.449337	1.802991	-2.291319
44	2.821405	-1.666730	1.839825	-2.537973
45	2.943865	-1.920380	1.855605	-2.816144
46	3.054021	-2.217441	1.843860	-3.129500
47	3.139657	-2.561693	1.793397	-3.479724
48	3.194378	-2.963718	1.689744	-3.865044
49	3.191723	-3.417910	1.515595	-4.279812
50	3.110627	-3.920003	1.251988	-4.710185
51	2.928438	-4.458613	0.881305	-5.133162
52	2.620336	-5.002780	0.393519	-5.513966

Continued on next page

Table 14
Integrated electric-field curve data records for the single-slot parametric sweep. continued.

Run ID	$\Re\{E_1\}$	$\Im\{E_1\}$	$\Re\{E_2\}$	$\Im\{E_2\}$
53	2.170324	-5.509174	-0.210481	-5.809875
54	1.592064	-5.932732	-0.899970	-5.977103
55	0.910934	-6.221813	-1.632564	-5.983379
56	0.178728	-6.345235	-2.349446	-5.819630
57	-0.542021	-6.297636	-2.991388	-5.503432
58	-1.200968	-6.104866	-3.521210	-5.076980
59	-1.760755	-5.803754	-3.919501	-4.589394
60	-2.207504	-5.439216	-4.190430	-4.086671
61	-2.547179	-5.051678	-4.354528	-3.603802
62	-2.790576	-4.668393	-4.432202	-3.160846
63	-2.902238	-4.383945	-4.474920	-2.889773
64	3.195671	-1.713049	2.146575	-2.714927
65	3.350480	-1.966993	2.191758	-3.005793
66	3.490788	-2.260927	2.212369	-3.332575
67	3.621653	-2.607343	2.201453	-3.700045
68	3.724882	-3.009665	2.142821	-4.108545
69	3.794632	-3.479613	2.025735	-4.560129
70	3.794618	-4.005569	1.827808	-5.045348
71	3.711851	-4.595179	1.527666	-5.551849
72	3.509441	-5.223149	1.104460	-6.051517
73	3.166363	-5.861809	0.547740	-6.506978
74	2.662371	-6.465059	-0.142876	-6.870521
75	2.004363	-6.981076	-0.941396	-7.091241
76	1.220042	-7.345158	-1.798461	-7.129205
77	0.367796	-7.524451	-2.647251	-6.969672
78	-0.485391	-7.505269	-3.422084	-6.629067
79	-1.274794	-7.309416	-4.071572	-6.150650
80	-1.955655	-6.979956	-4.570864	-5.590681
81	-2.507479	-6.567244	-4.920453	-5.003404
82	-2.930448	-6.117663	-5.137873	-4.431569
83	-3.238020	-5.668887	-5.249382	-3.903135
84	-3.401397	-5.443905	-5.301440	-3.636247
85	3.627577	-1.929140	2.481360	-3.107679
86	3.801307	-2.211614	2.533801	-3.435801
87	3.966171	-2.542315	2.560243	-3.806196
88	4.116087	-2.928175	2.551549	-4.221927
89	4.234380	-3.372751	2.493937	-4.685561
90	4.313364	-3.888526	2.369779	-5.196228
91	4.332298	-4.480364	2.157421	-5.746722
92	4.248273	-5.127684	1.833217	-6.322119
93	4.043380	-5.831527	1.370759	-6.895437
94	3.685557	-6.553385	0.761123	-7.427243
95	3.153012	-7.245151	0.001044	-7.864672
96	2.446104	-7.846122	-0.886112	-8.151847
97	1.589732	-8.294932	-1.853932	-8.241430
98	0.643275	-8.544641	-2.828769	-8.109872
99	-0.319870	-8.575053	-3.734832	-7.768029
100	-1.227149	-8.401564	-4.511455	-7.259726
101	-2.024364	-8.068407	-5.124079	-6.644247
102	-2.683703	-7.629678	-5.568061	-5.983514
103	-3.198788	-7.137583	-5.857818	-5.329023
104	-3.583636	-6.629865	-6.020639	-4.709917

Continued on next page

Table 14
Integrated electric-field curve data records for the single-slot parametric sweep. continued.

Run ID	$\Re\{E_1\}$	$\Im\{E_1\}$	$\Re\{E_2\}$	$\Im\{E_2\}$
105	-3.745695	-6.253959	-6.108371	-4.366440
106	4.077691	-2.167038	2.796779	-3.500367
107	4.262761	-2.471568	2.853440	-3.856364
108	4.445921	-2.835321	2.884101	-4.264823
109	4.613136	-3.258197	2.877158	-4.722297
110	4.753627	-3.751022	2.816686	-5.232201
111	4.846234	-4.315921	2.685838	-5.793984
112	4.870870	-4.957052	2.462463	-6.400637
113	4.793570	-5.667376	2.118747	-7.037061
114	4.590708	-6.439834	1.631841	-7.674863
115	4.220902	-7.233581	0.982904	-8.274853
116	3.666491	-8.007830	0.168921	-8.781871
117	2.918041	-8.695865	-0.792594	-9.136203
118	2.004141	-9.229461	-1.849011	-9.283168
119	0.978474	-9.558059	-2.930124	-9.193364
120	-0.081927	-9.649477	-3.953287	-8.872089
121	-1.101398	-9.514771	-4.851987	-8.356428
122	-2.015064	-9.196531	-5.580464	-7.708156
123	-2.784508	-8.747064	-6.125143	-6.994173
124	-3.399465	-8.225363	-6.497875	-6.271358
125	-3.869581	-7.675356	-6.723951	-5.579040
126	-4.097104	-7.378252	-6.836193	-5.233634
127	4.450806	-2.346012	3.103825	-3.856826
128	4.655195	-2.678007	3.168013	-4.251140
129	4.853771	-3.066664	3.204613	-4.696020
130	5.036177	-3.517105	3.202822	-5.192741
131	5.190887	-4.038955	3.145345	-5.745229
132	5.298664	-4.637801	3.014093	-6.353644
133	5.336627	-5.317159	2.785381	-7.010522
134	5.276106	-6.074218	2.433162	-7.701869
135	5.082830	-6.894792	1.930788	-8.402029
136	4.722777	-7.749823	1.256359	-9.070930
137	4.169319	-8.590995	0.405458	-9.650656
138	3.413487	-9.356564	-0.607341	-10.080377
139	2.472839	-9.977070	-1.738570	-10.300327
140	1.398260	-10.388512	-2.915702	-10.274043
141	0.264284	-10.563729	-4.055526	-9.995469
142	-0.848622	-10.491473	-5.079592	-9.495367
143	-1.867224	-10.212119	-5.933850	-8.834328
144	-2.744540	-9.777807	-6.594620	-8.081649
145	-3.461994	-9.246051	-7.065275	-7.299201
146	-4.018845	-8.677794	-7.371249	-6.545134
147	-4.390505	-8.557296	-7.522597	-6.172181
148	4.927363	-2.592178	3.385170	-4.197267
149	5.149933	-2.950672	3.457536	-4.619088
150	5.365669	-3.371532	3.499154	-5.096827
151	5.568743	-3.860955	3.499435	-5.629070
152	5.739318	-4.423443	3.443161	-6.219690
153	5.863009	-5.068825	3.310831	-6.868520
154	5.914942	-5.800277	3.078553	-7.570072
155	5.862910	-6.612966	2.718318	-8.309295
156	5.676977	-7.498495	2.204819	-9.061931

Continued on next page

Table 14
Integrated electric-field curve data records for the single-slot parametric sweep. continued.

Run ID	$\Re\{E_1\}$	$\Im\{E_1\}$	$\Re\{E_2\}$	$\Im\{E_2\}$
157	5.315627	-8.420971	1.514770	-9.785983
158	4.754758	-9.340222	0.639243	-10.429029
159	3.980816	-10.197785	-0.411372	-10.927475
160	3.003252	-10.912095	-1.596635	-11.219138
161	1.868263	-11.420487	-2.850095	-11.259166
162	0.649865	-11.678312	-4.085487	-11.033639
163	-0.567761	-11.679337	-5.220313	-10.566458
164	-1.705215	-11.444936	-6.191318	-9.911457
165	-2.706542	-11.028000	-6.964717	-9.139202
166	-3.541444	-10.490628	-7.536580	-8.317873
167	-4.203794	-9.896807	-7.926926	-7.510065
168	-4.745065	-10.052481	-8.124830	-7.140143
169	5.322820	-2.793961	3.658619	-4.520001
170	5.557563	-3.174676	3.735973	-4.967682
171	5.791926	-3.619570	3.782532	-5.469016
172	6.008955	-4.132660	3.787638	-6.027824
173	6.196103	-4.722991	3.735947	-6.647628
174	6.335555	-5.398179	3.607746	-7.328455
175	6.403611	-6.162522	3.379363	-8.065498
176	6.370597	-7.013393	3.023993	-8.844686
177	6.200650	-7.941394	2.511566	-9.643586
178	5.858838	-8.919640	1.820269	-10.423666
179	5.312965	-9.904505	0.936468	-11.131963
180	4.545679	-10.835375	-0.132821	-11.705319
181	3.562579	-11.639547	-1.356648	-12.079672
182	2.402725	-12.248161	-2.668655	-12.203726
183	1.132492	-12.608440	-3.988827	-12.054683
184	-0.163725	-12.699733	-5.230740	-11.645506
185	-1.402362	-12.537410	-6.322335	-11.022645
186	-2.517200	-12.167828	-7.218911	-10.252806
187	-3.468279	-11.651326	-7.908335	-9.408933
188	-4.249688	-11.046945	-8.404348	-8.547161
189	-4.697113	-10.856441	-8.658090	-8.131941
190	5.767105	-3.005460	3.913043	-4.803367
191	6.010353	-3.400868	3.997021	-5.266943
192	6.259374	-3.867416	4.050243	-5.789120
193	6.487707	-4.401280	4.062073	-6.370076
194	6.693405	-5.018577	4.017375	-7.013020
195	6.847326	-5.718832	3.897073	-7.718382
196	6.934879	-6.513475	3.678056	-8.481908
197	6.922581	-7.398123	3.333893	-9.292129
198	6.777832	-8.363463	2.837200	-10.126354
199	6.463014	-9.389710	2.160469	-10.952278
200	5.946623	-10.434016	1.291712	-11.718006
201	5.204655	-11.443770	0.228496	-12.365252
202	4.236629	-12.342370	-1.000682	-12.827984
203	3.071860	-13.060179	-2.342942	-13.052648
204	1.769584	-13.540171	-3.722225	-13.003615
205	0.408582	-13.748705	-5.054462	-12.683378
206	-0.923647	-13.688640	-6.258502	-12.126818
207	-2.155610	-13.397504	-7.282187	-11.394575
208	-3.234448	-12.929202	-8.098355	-10.556927

Continued on next page

Table 14
Integrated electric-field curve data records for the single-slot parametric sweep. continued.

Run ID	$\Re\{E_1\}$	$\Im\{E_1\}$	$\Re\{E_2\}$	$\Im\{E_2\}$
209	-4.131591	-12.350031	-8.707189	-9.686770
210	-4.643980	-12.145891	-9.037064	-9.263868
211	6.017885	-3.136276	4.165773	-5.112304
212	6.275888	-3.544329	4.256179	-5.597497
213	6.530152	-4.019638	4.312925	-6.141249
214	6.768921	-4.565592	4.327513	-6.744974
215	6.979413	-5.190653	4.285291	-7.412236
216	7.145408	-5.903838	4.167041	-8.144252
217	7.243387	-6.708429	3.950256	-8.936361
218	7.245922	-7.605022	3.608536	-9.777638
219	7.117779	-8.582810	3.113530	-10.648335
220	6.826053	-9.624871	2.440153	-11.514315
221	6.338523	-10.695304	1.571574	-12.328227
222	5.626001	-11.732987	0.505560	-13.032369
223	4.689365	-12.681604	-0.736692	-13.564271
224	3.549394	-13.470301	-2.108356	-13.862948
225	2.253841	-14.028811	-3.538087	-13.891164
226	0.878839	-14.326246	-4.942663	-13.642466
227	-0.492524	-14.352819	-6.238900	-13.141910
228	-1.782250	-14.135390	-7.365737	-12.444232
229	-2.935430	-13.726041	-8.290377	-11.617242
230	-3.910138	-13.187898	-8.998467	-10.739116
231	-4.553039	-13.514412	-9.326091	-10.374380
232	6.313716	-3.265956	4.396338	-5.355154
233	6.579520	-3.683052	4.490217	-5.853138
234	6.839508	-4.162903	4.553019	-6.407937
235	7.091885	-4.716604	4.575310	-7.023000
236	7.308857	-5.342359	4.542801	-7.701388
237	7.495748	-6.062018	4.438518	-8.443492
238	7.613664	-6.867822	4.240393	-9.247110
239	7.641113	-7.767212	3.920563	-10.104928
240	7.548132	-8.751746	3.454800	-10.996854
241	7.300334	-9.805093	2.816877	-11.894264
242	6.863819	-10.893886	1.987926	-12.754856
243	6.215206	-11.976154	0.960958	-13.524477
244	5.339771	-12.989728	-0.253086	-14.143486
245	4.253152	-13.863982	-1.612717	-14.550529
246	2.993682	-14.541925	-3.059398	-14.703404
247	1.624227	-14.969032	-4.513615	-14.580303
248	0.223308	-15.130756	-5.895495	-14.194319
249	-1.131230	-15.038644	-7.136363	-13.587707
250	-2.375126	-14.732752	-8.190141	-12.821577
251	-3.458398	-14.270870	-9.033264	-11.970176
252	-4.221113	-14.434680	-9.510230	-11.480609
253	6.709728	-3.464205	4.608889	-5.603229
254	6.994580	-3.904358	4.707749	-6.116615
255	7.268194	-4.404900	4.774318	-6.686676
256	7.530584	-4.977620	4.800314	-7.315831
257	7.758033	-5.623116	4.772103	-8.008581
258	7.956582	-6.364421	4.672294	-8.765498
259	8.083181	-7.189335	4.480325	-9.584079
260	8.127908	-8.112360	4.171928	-10.456442

Continued on next page

Table 14
Integrated electric-field curve data records for the single-slot parametric sweep. continued.

Run ID	$\Re\{E_1\}$	$\Im\{E_1\}$	$\Re\{E_2\}$	$\Im\{E_2\}$
261	8.054039	-9.123784	3.719293	-11.367413
262	7.828848	-10.207084	3.100326	-12.287912
263	7.419689	-11.333336	2.294479	-13.179513
264	6.797852	-12.456166	1.293197	-13.992807
265	5.953432	-13.531415	0.101777	-14.669983
266	4.890535	-14.483726	-1.245849	-15.151990
267	3.640713	-15.250655	-2.696973	-15.391818
268	2.259750	-15.781008	-4.180432	-15.364014
269	0.822801	-16.050384	-5.617320	-15.070738
270	-0.594126	-16.058713	-6.936677	-14.542603
271	-1.920776	-15.839364	-8.086612	-13.837328
272	-3.112413	-15.437520	-9.041735	-13.013333
273	-3.850810	-15.610742	-9.537427	-12.588609
274	6.969529	-3.575001	4.810848	-5.802100
275	7.263421	-4.018293	4.915775	-6.321417
276	7.543469	-4.519864	4.989031	-6.896049
277	7.811200	-5.091057	5.023461	-7.530045
278	8.055042	-5.739383	5.006229	-8.226703
279	8.260371	-6.472086	4.921156	-8.987417
280	8.400307	-7.287852	4.748456	-9.810401
281	8.470728	-8.204349	4.466391	-10.688540
282	8.435350	-9.211812	4.049972	-11.607518
283	8.251282	-10.290386	3.472567	-12.547793
284	7.902512	-11.427870	2.716522	-13.470599
285	7.352071	-12.579380	1.767577	-14.333971
286	6.580122	-13.687266	0.630409	-15.081113
287	5.595514	-14.711662	-0.674066	-15.657635
288	4.411923	-15.576164	-2.102627	-16.014829
289	3.077816	-16.226921	-3.590905	-16.117729
290	1.654360	-16.632981	-5.069909	-15.958246
291	0.215491	-16.785009	-6.468030	-15.555212
292	-1.169194	-16.694527	-7.724628	-14.949278
293	-2.436680	-16.407493	-8.796352	-14.202613
294	-3.379953	-16.702006	-9.468503	-13.661716
295	7.265947	-3.716914	4.992008	-6.005465
296	7.551505	-4.164632	5.098594	-6.537726
297	7.837226	-4.673167	5.174842	-7.120009
298	8.110840	-5.249653	5.213145	-7.759923
299	8.361613	-5.901885	5.201234	-8.461129
300	8.576854	-6.637763	5.123913	-9.225680
301	8.740652	-7.464557	4.962719	-10.051106
302	8.819482	-8.374176	4.696642	-10.931817
303	8.804016	-9.383404	4.300595	-11.859265
304	8.655280	-10.467521	3.753632	-12.807424
305	8.340151	-11.603783	3.034408	-13.747083
306	7.837564	-12.768060	2.129300	-14.638208
307	7.125298	-13.912172	1.037194	-15.431336
308	6.197402	-14.978806	-0.226045	-16.074395
309	5.067780	-15.908561	-1.624679	-16.515446
310	3.775505	-16.654253	-3.106075	-16.719887
311	2.374831	-17.168825	-4.600556	-16.670410
312	0.933264	-17.436347	-6.040223	-16.375674

Continued on next page

Table 14
Integrated electric-field curve data records for the single-slot parametric sweep. continued.

Run ID	$\Re\{E_1\}$	$\Im\{E_1\}$	$\Re\{E_2\}$	$\Im\{E_2\}$
313	-0.479529	-17.462180	-7.361605	-15.868796
314	-1.793251	-17.280754	-8.513721	-15.206015
315	-2.756880	-17.512221	-9.271446	-14.714332
316	7.375829	-3.767554	5.180023	-6.217233
317	7.671036	-4.218256	5.287980	-6.757738
318	7.957228	-4.724101	5.367255	-7.348969
319	8.231071	-5.296312	5.408854	-7.997702
320	8.482827	-5.940992	5.401199	-8.706538
321	8.697594	-6.663943	5.330002	-9.478045
322	8.866289	-7.477123	5.176288	-10.310529
323	8.958556	-8.373904	4.920985	-11.198484
324	8.957861	-9.358658	4.542169	-12.130938
325	8.832010	-10.418345	4.016960	-13.088272
326	8.555721	-11.537981	3.325405	-14.043412
327	8.101026	-12.687195	2.453636	-14.958800
328	7.448337	-13.826151	1.398026	-15.788743
329	6.587643	-14.908131	0.167066	-16.484286
330	5.530139	-15.871335	-1.205105	-16.994590
331	4.306666	-16.672011	-2.672458	-17.282087
332	2.962449	-17.259603	-4.172608	-17.325061
333	1.559194	-17.616528	-5.639370	-17.125862
334	0.161967	-17.741233	-7.012287	-16.708249
335	-1.169126	-17.655088	-8.241444	-16.115965
336	-2.087090	-18.155283	-8.973670	-15.673606
337	7.651555	-3.911310	5.334152	-6.401674
338	7.950770	-4.368214	5.441398	-6.940283
339	8.242648	-4.881246	5.522248	-7.534545
340	8.521701	-5.458457	5.566369	-8.184360
341	8.778965	-6.107356	5.562636	-8.893342
342	9.002388	-6.834503	5.497331	-9.663219
343	9.175389	-7.645451	5.351621	-10.492273
344	9.271660	-8.532857	5.111524	-11.377255
345	9.297221	-9.523248	4.753497	-12.306069
346	9.196287	-10.580721	4.256848	-13.261882
347	8.944536	-11.689085	3.602568	-14.221904
348	8.533454	-12.846579	2.774859	-15.152079
349	7.933575	-14.009114	1.767419	-16.012092
350	7.129749	-15.117985	0.589958	-16.751582
351	6.131949	-16.131877	-0.734503	-17.325337
352	4.961725	-16.995439	-2.164014	-17.695583
353	3.659754	-17.670493	-3.646339	-17.836509
354	2.280402	-18.128856	-5.118445	-17.742846
355	0.883071	-18.360202	-6.520781	-17.430297
356	-0.464892	-18.380801	-7.797538	-16.937616
357	-1.346319	-18.788067	-8.579095	-16.601207
358	7.854559	-4.011412	5.482380	-6.570980
359	8.143202	-4.463286	5.588584	-7.111392
360	8.433191	-4.974102	5.670929	-7.706501
361	8.707278	-5.545062	5.717732	-8.356689
362	8.972681	-6.193420	5.718378	-9.064611
363	9.195091	-6.910097	5.660023	-9.832699
364	9.381298	-7.715126	5.526687	-10.658259

Continued on next page

Table 14
Integrated electric-field curve data records for the single-slot parametric sweep. continued.

Run ID	$\Re\{E_1\}$	$\Im\{E_1\}$	$\Re\{E_2\}$	$\Im\{E_2\}$
365	9.493367	-8.594957	5.301037	-11.538183
366	9.525681	-9.560760	4.964038	-12.462716
367	9.449098	-10.602020	4.495562	-13.417397
368	9.240448	-11.711503	3.874956	-14.381362
369	8.868752	-12.852402	3.090963	-15.322359
370	8.323172	-14.005345	2.136624	-16.201284
371	7.585070	-15.121209	1.015109	-16.977737
372	6.660555	-16.162544	-0.254563	-17.608009
373	5.562774	-17.074487	-1.639251	-18.054795
374	4.326853	-17.819276	-3.090306	-18.288091
375	2.998888	-18.365420	-4.552589	-18.298240
376	1.633593	-18.697512	-5.968483	-18.092952
377	0.284903	-18.824585	-7.291542	-17.700115
378	-0.524379	-19.693187	-8.041491	-17.465848
379	8.167647	-4.162890	5.602065	-6.697653
380	8.471711	-4.625499	5.714412	-7.240854
381	8.773574	-5.146880	5.799898	-7.835726
382	9.060233	-5.728677	5.850717	-8.484073
383	9.328431	-6.380332	5.857195	-9.188892
384	9.567970	-7.108945	5.806862	-9.951904
385	9.760537	-7.915086	5.685520	-10.771643
386	9.890714	-8.802960	5.476041	-11.644284
387	9.939800	-9.771052	5.161752	-12.561845
388	9.885408	-10.815381	4.722890	-13.511559
389	9.704648	-11.923578	4.142567	-14.472582
390	9.376859	-13.081666	3.404872	-15.419575
391	8.874650	-14.248941	2.504743	-16.316157
392	8.189713	-15.395374	1.442736	-17.125387
393	7.320701	-16.480323	0.232668	-17.806188
394	6.277068	-17.453569	-1.097458	-18.320741
395	5.087657	-18.276980	-2.507048	-18.641063
396	3.793106	-18.915592	-3.945317	-18.751510
397	2.443850	-19.352645	-5.359034	-18.653854
398	1.099619	-19.587194	-6.692948	-18.370781
399	0.251243	-20.225181	-7.517835	-18.183613
400	8.117312	-4.137830	5.731673	-6.852494
401	8.399737	-4.586471	5.843526	-7.403582
402	8.694047	-5.094641	5.929129	-8.001058
403	8.974940	-5.660548	5.980904	-8.650527
404	9.243429	-6.296156	5.989081	-9.354843
405	9.469822	-6.993470	5.942516	-10.115316
406	9.668295	-7.775586	5.827240	-10.931114
407	9.802994	-8.629968	5.627780	-11.798656
408	9.853706	-9.552866	5.326572	-12.710211
409	9.820225	-10.556674	4.907874	-13.654092
410	9.669604	-11.621086	4.354487	-14.612243
411	9.384108	-12.730697	3.654206	-15.557635
412	8.937343	-13.858415	2.794762	-16.464825
413	8.321005	-14.973394	1.778082	-17.294939
414	7.532156	-16.036771	0.616218	-18.009205
415	6.581224	-17.011086	-0.666499	-18.573063
416	5.486789	-17.852262	-2.035436	-18.957841

Continued on next page

Table 14
Integrated electric-field curve data records for the single-slot parametric sweep. continued.

Run ID	$\Re\{E_1\}$	$\Im\{E_1\}$	$\Re\{E_2\}$	$\Im\{E_2\}$
417	4.283322	-18.530737	-3.445438	-19.145164
418	3.016024	-19.028498	-4.847569	-19.134118
419	1.756408	-19.333890	-6.168506	-18.942454
420	0.963246	-20.332764	-7.005595	-18.797607
421	8.499123	-4.318744	5.847064	-6.955592
422	8.811320	-4.787200	5.961745	-7.503258
423	9.112779	-5.305517	6.050931	-8.098389
424	9.402759	-5.882076	6.107546	-8.743264
425	9.672042	-6.521789	6.122184	-9.440859
426	9.921873	-7.237516	6.085384	-10.193991
427	10.120542	-8.019856	5.981988	-10.999836
428	10.274116	-8.885558	5.800453	-11.856835
429	10.350200	-9.823336	5.523960	-12.758744
430	10.337782	-10.835318	5.136509	-13.694671
431	10.212955	-11.908649	4.622268	-14.647222
432	9.958884	-13.032229	3.968396	-15.595056
433	9.552918	-14.184376	3.162814	-16.513067
434	8.985034	-15.332034	2.208470	-17.365479
435	8.245874	-16.437447	1.111734	-18.118277
436	7.343303	-17.465613	-0.108484	-18.738114
437	6.293959	-18.378818	-1.422338	-19.196278
438	5.126792	-19.144337	-2.791684	-19.473437
439	3.879133	-19.739326	-4.171598	-19.562580
440	2.606126	-20.151138	-5.506193	-19.471456
441	1.724642	-20.867266	-6.410903	-19.250535
442	8.758706	-4.442606	5.933163	-7.048907
443	9.090134	-4.921446	6.047443	-7.589980
444	9.403282	-5.448385	6.137997	-8.180638
445	9.695797	-6.028439	6.197365	-8.821706
446	9.975475	-6.675615	6.216789	-9.514873
447	10.227322	-7.391492	6.185822	-10.260756
448	10.440193	-8.181097	6.092220	-11.060989
449	10.600421	-9.045810	5.923280	-11.909692
450	10.699800	-9.992829	5.664208	-12.801580
451	10.703626	-11.003575	5.299687	-13.726598
452	10.606560	-12.085775	4.814127	-14.672913
453	10.375042	-13.206455	4.196691	-15.617489
454	10.008746	-14.366891	3.437427	-16.535535
455	9.483068	-15.526324	2.534667	-17.398504
456	8.792130	-16.654692	1.493154	-18.173750
457	7.940076	-17.714053	0.330095	-18.830513
458	6.942501	-18.673805	-0.929811	-19.340771
459	5.822326	-19.496400	-2.251072	-19.684051
460	4.617236	-20.163381	-3.592566	-19.850981
461	3.365034	-20.658142	-4.915110	-19.845181
462	2.483844	-21.105583	-5.835567	-19.794740
463	8.641700	-4.369698	6.019484	-7.133153
464	8.930454	-4.816968	6.137803	-7.678410
465	9.234055	-5.327286	6.230994	-8.272273
466	9.525863	-5.892697	6.292975	-8.914558
467	9.802213	-6.520281	6.315286	-9.607078
468	10.050186	-7.212166	6.288761	-10.352859

Continued on next page

Table 14
Integrated electric-field curve data records for the single-slot parametric sweep. continued.

Run ID	$\Re\{E_1\}$	$\Im\{E_1\}$	$\Re\{E_2\}$	$\Im\{E_2\}$
469	10.261526	-7.973467	6.201372	-11.149489
470	10.428899	-8.810468	6.040625	-11.995018
471	10.525565	-9.714723	5.790759	-12.883747
472	10.544274	-10.689896	5.440564	-13.806759
473	10.462870	-11.723236	4.974795	-14.748224
474	10.266459	-12.805389	4.382144	-15.691117
475	9.935612	-13.914288	3.653482	-16.611033
476	9.459330	-15.026886	2.786977	-17.481062
477	8.835538	-16.122123	1.787297	-18.271079
478	8.058634	-17.155406	0.667753	-18.952487
479	7.139705	-18.107488	-0.555154	-19.501004
480	6.105944	-18.936691	-1.840150	-19.890847
481	4.986163	-19.621032	-3.151131	-20.114141
482	3.810357	-20.153301	-4.457350	-20.171753
483	3.091645	-21.227278	-5.337352	-20.179765

Appendix B: Supplementary Single-Slot Analysis Figures

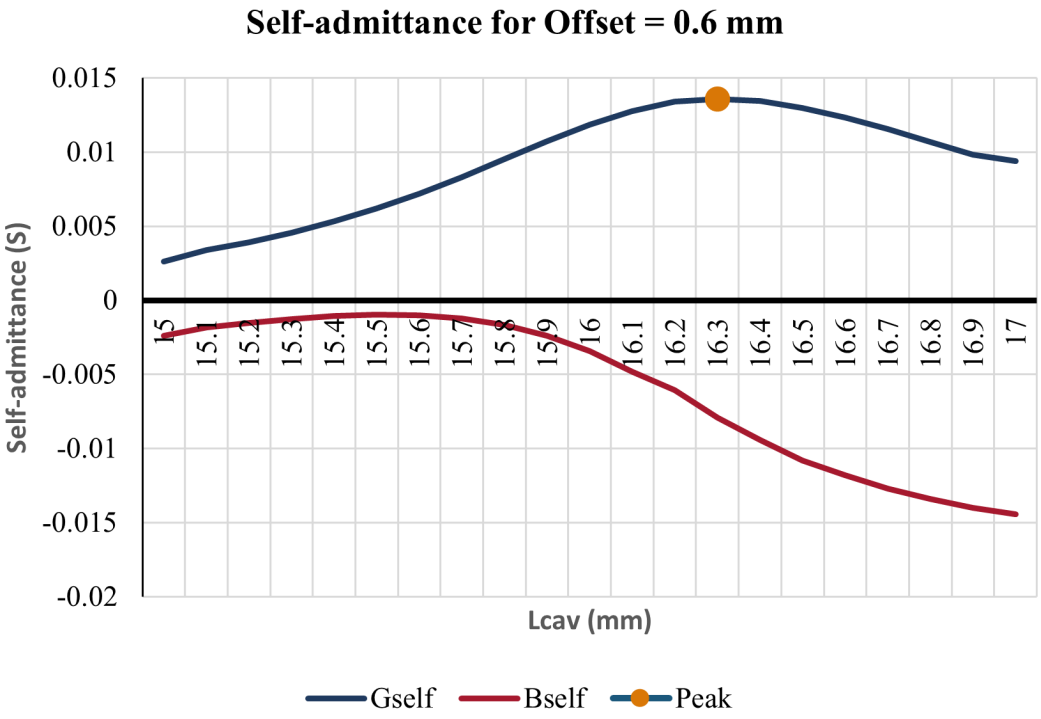


Figure 36. *CST result for slot offset* $x = 0.6$ mm.

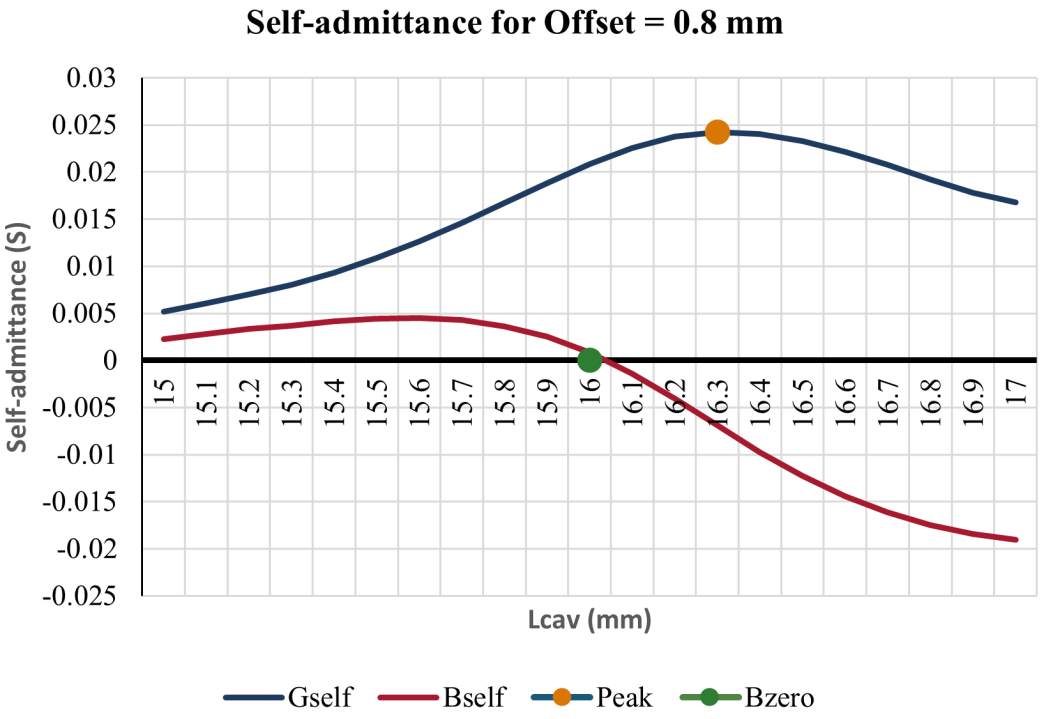


Figure 37. *CST result for slot offset* $x = 0.8$ mm.

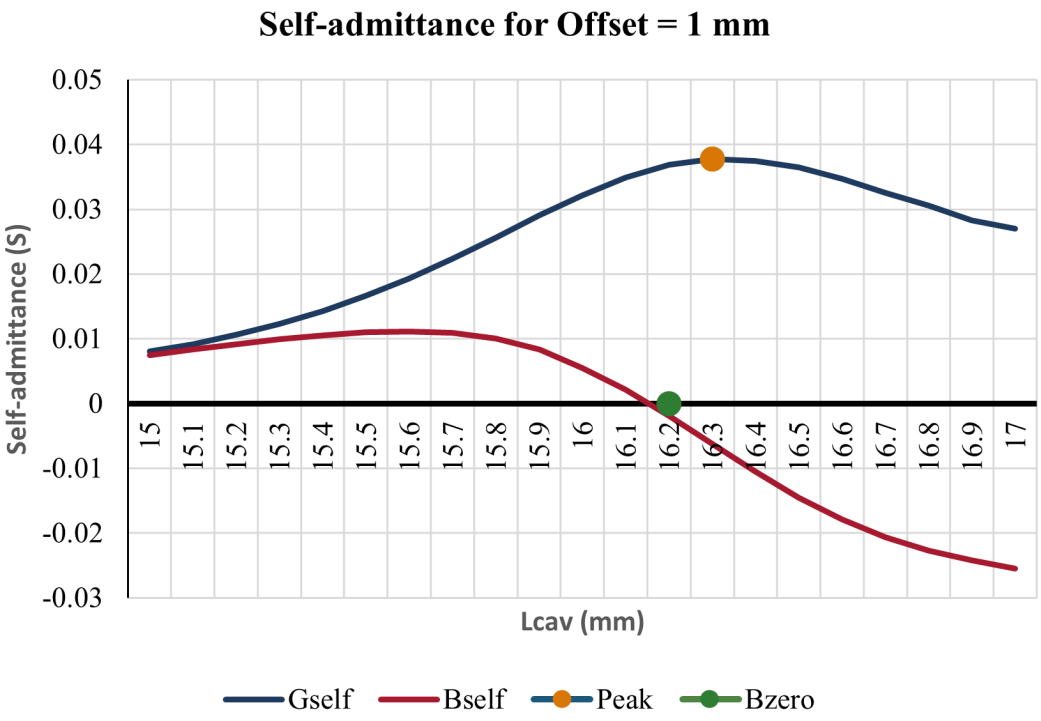


Figure 38. *CST result for slot offset* $x = 1.0$ mm.

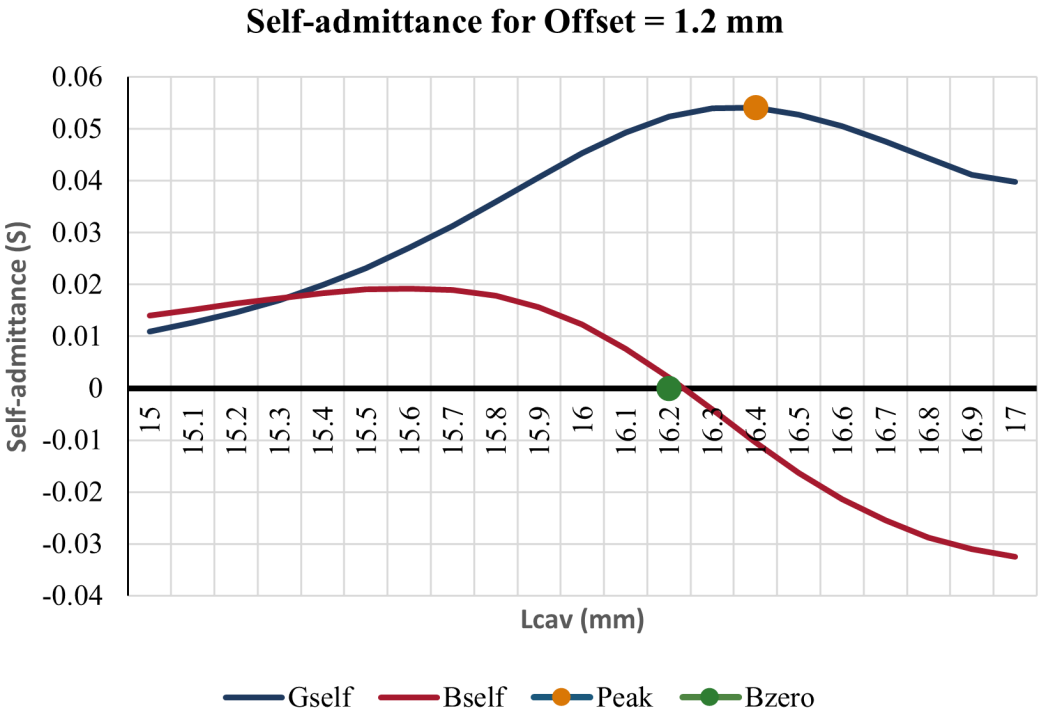


Figure 39. *CST result for slot offset* $x = 1.2$ mm.

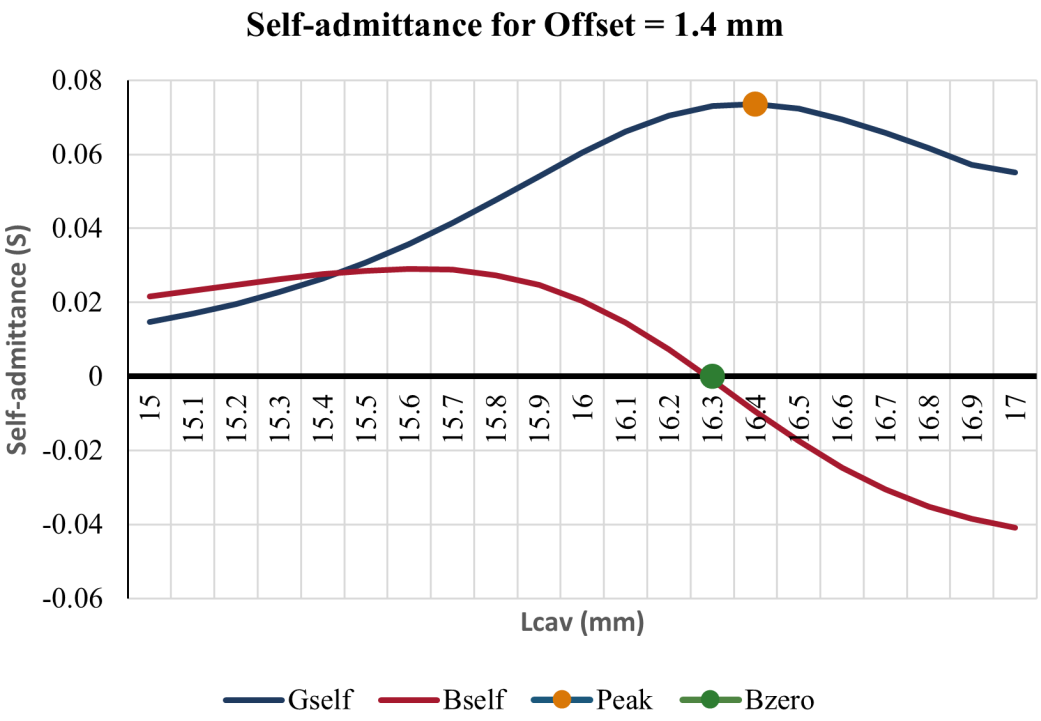


Figure 40. *CST result for slot offset* $x = 1.4$ mm.

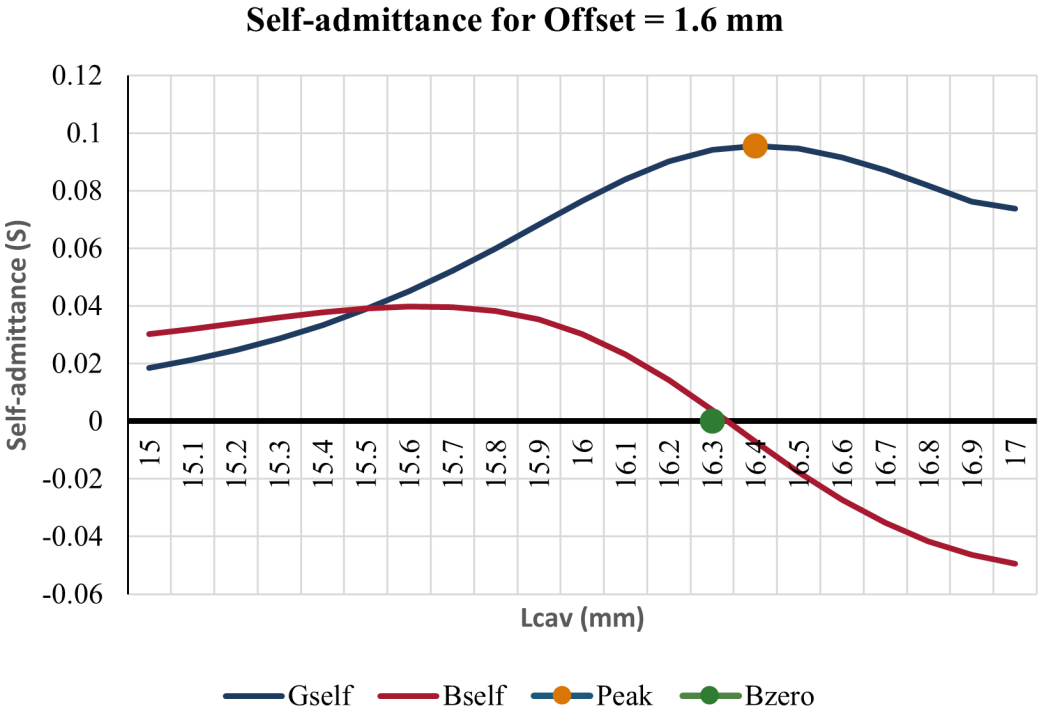


Figure 41. *CST result for slot offset* $x = 1.6$ mm.

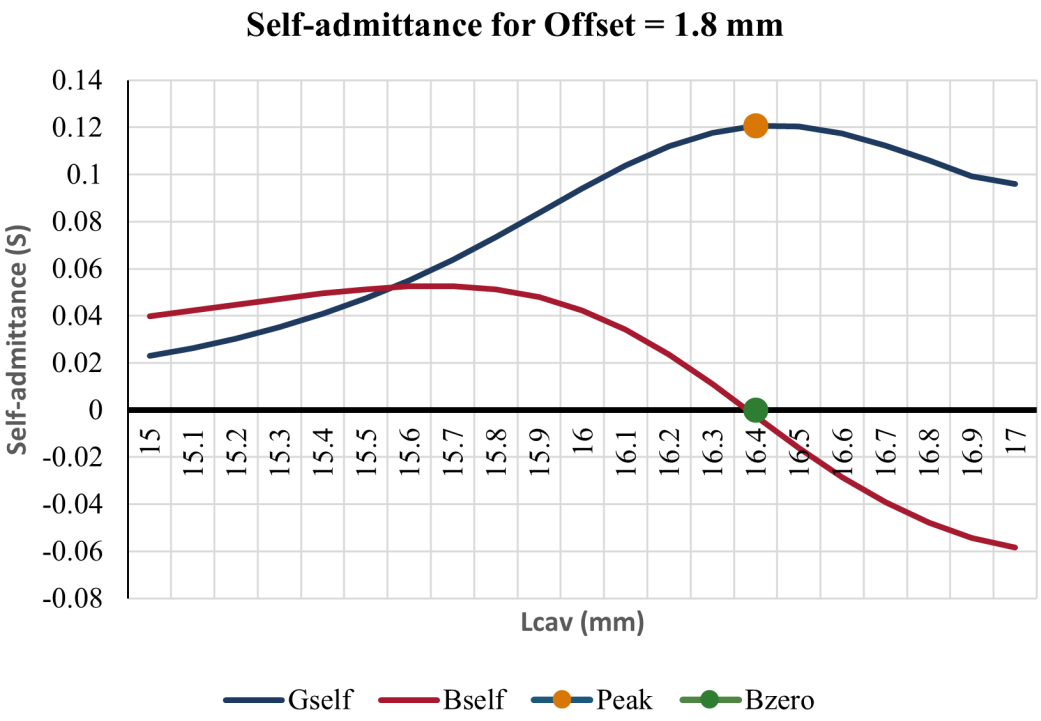


Figure 42. *CST result for slot offset* $x = 1.8$ mm.

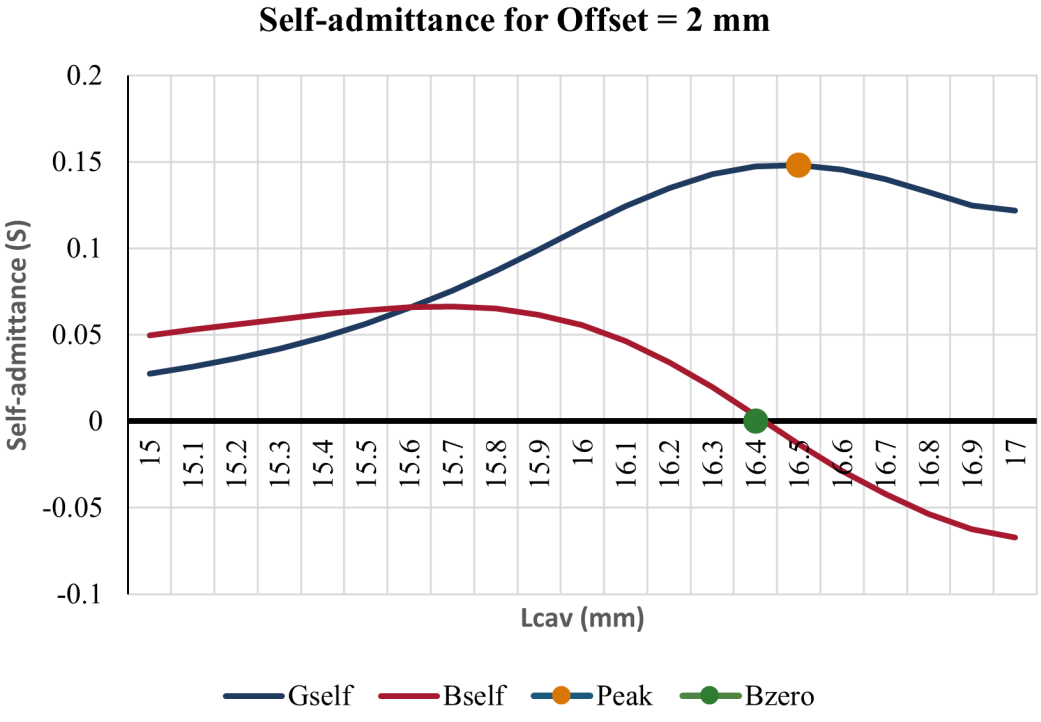


Figure 43. *CST result for slot offset* $x = 2.0$ mm.

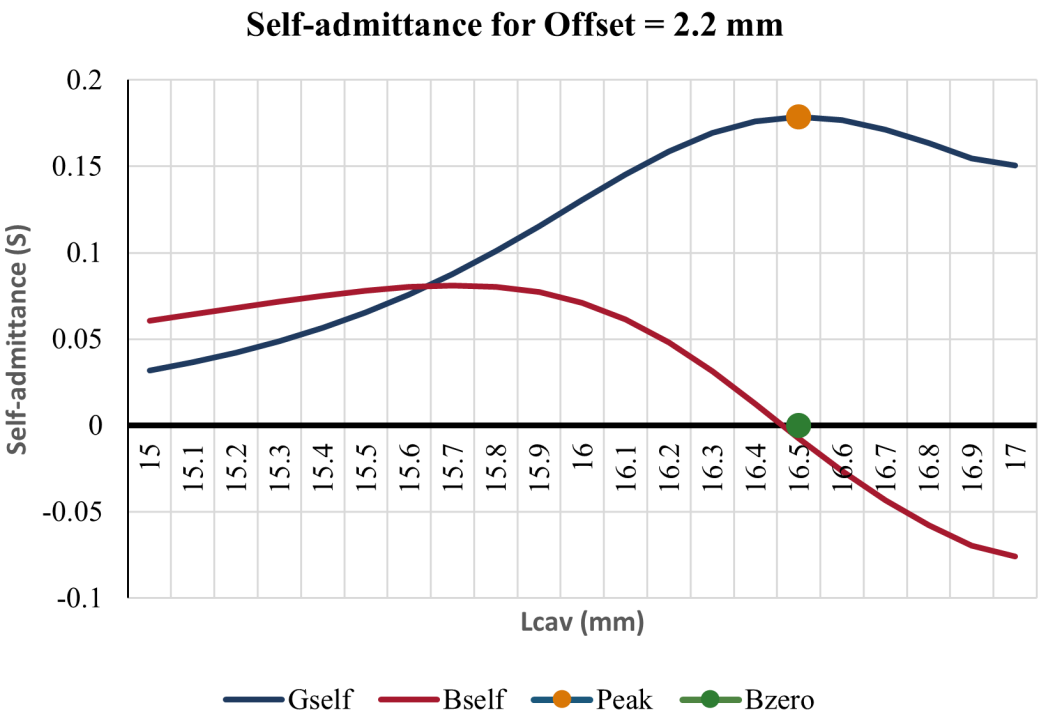


Figure 44. *CST result for slot offset* $x = 2.2$ mm.

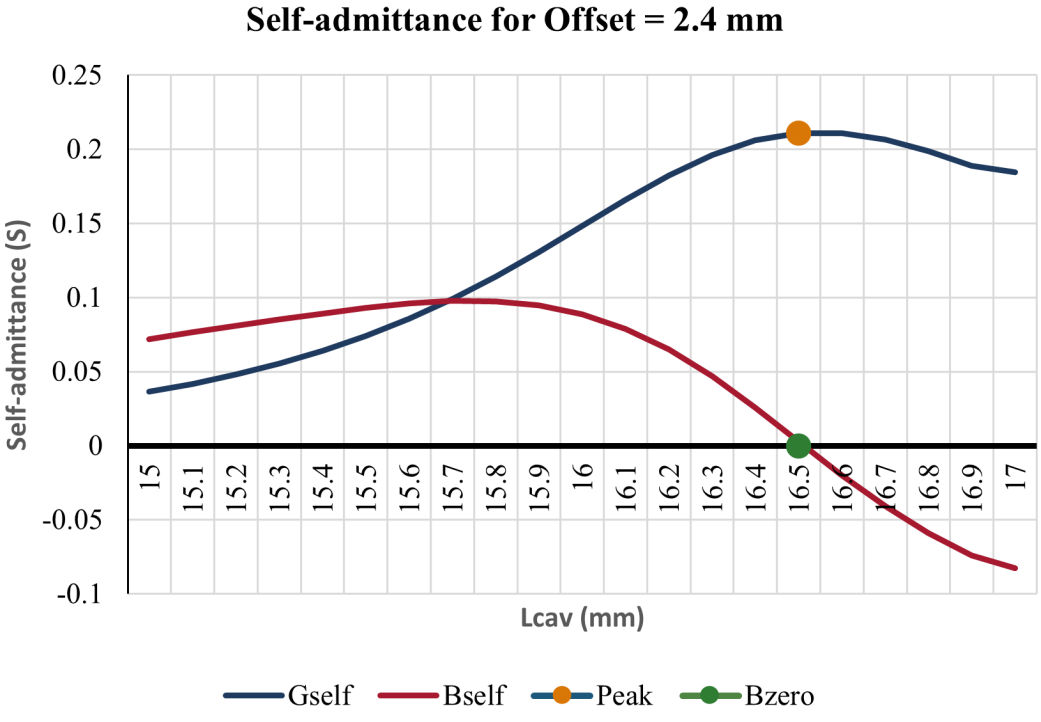


Figure 45. *CST result for slot offset* $x = 2.4$ mm.

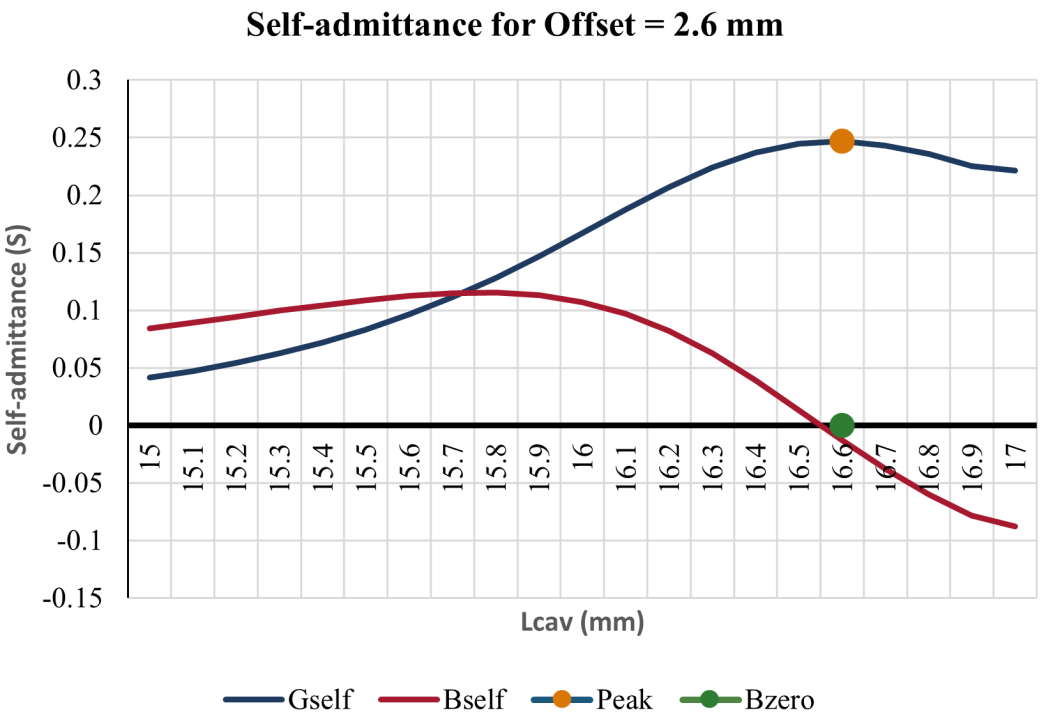


Figure 46. *CST result for slot offset* $x = 2.6$ mm.

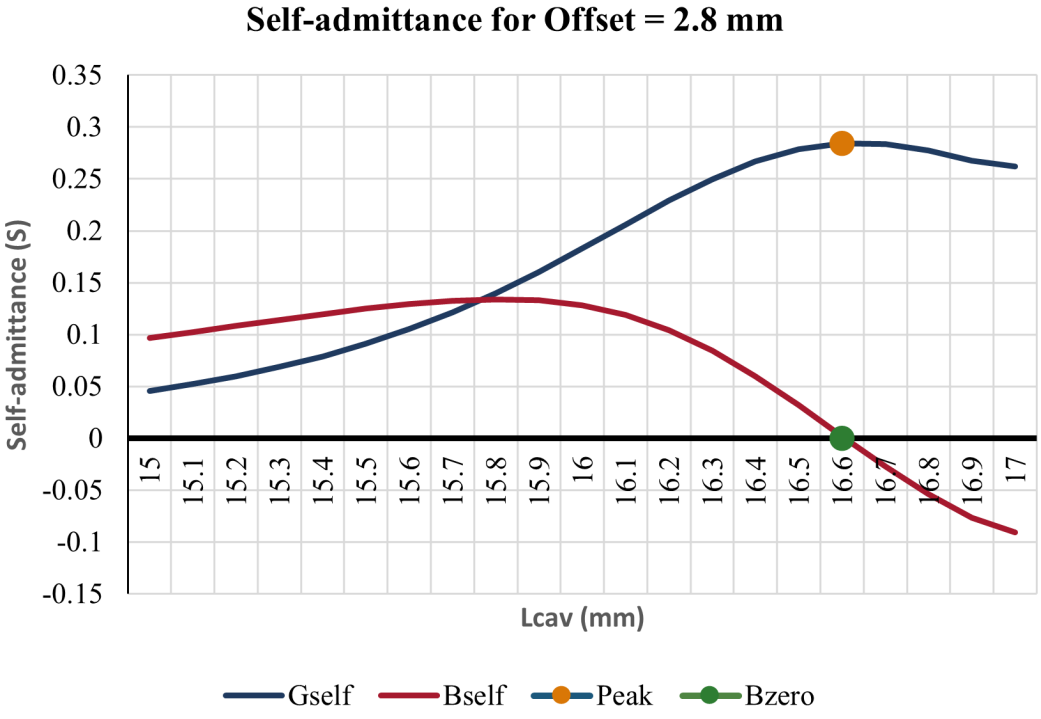


Figure 47. *CST result for slot offset* $x = 2.8$ mm.

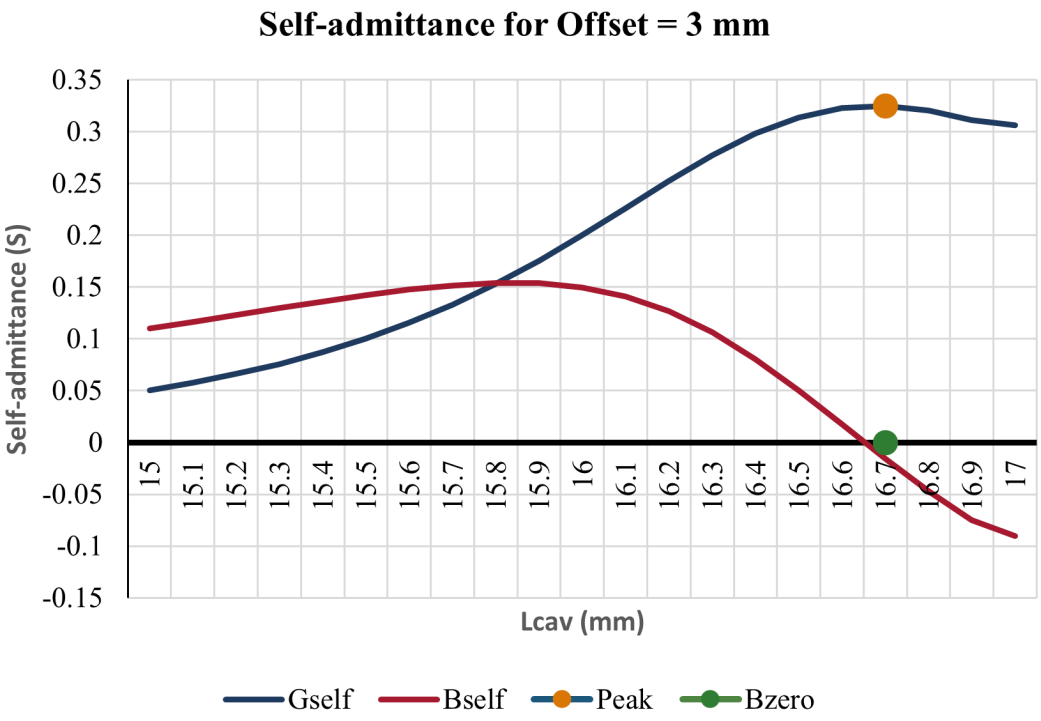


Figure 48. *CST result for slot offset* $x = 3.0$ mm.

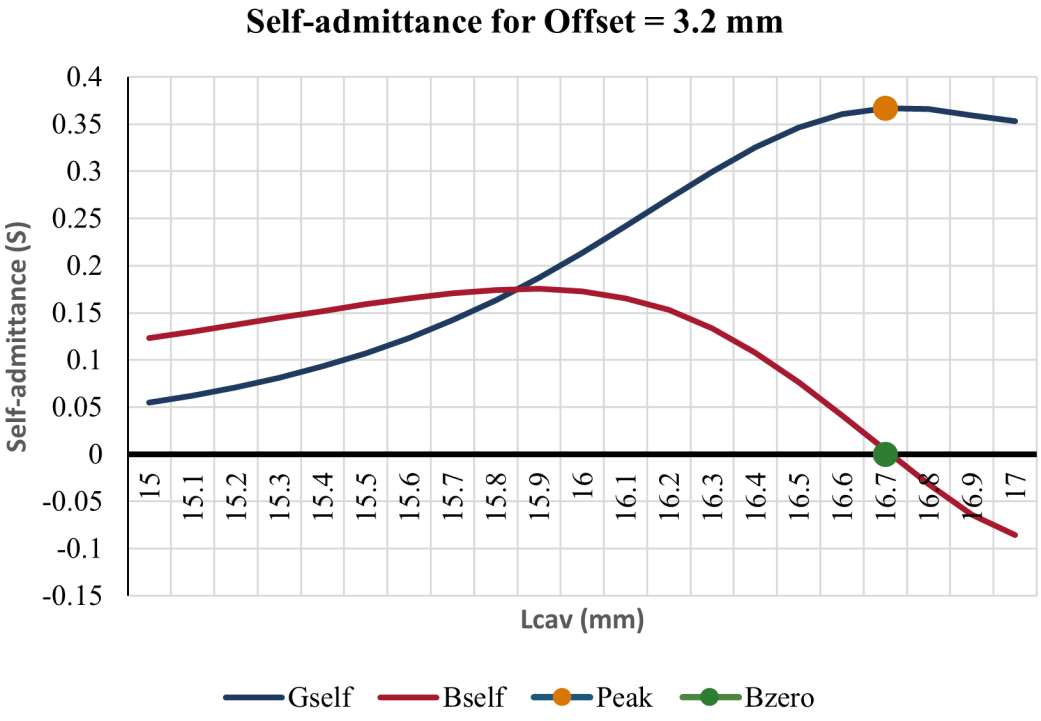


Figure 49. *CST result for slot offset* $x = 3.2$ mm.

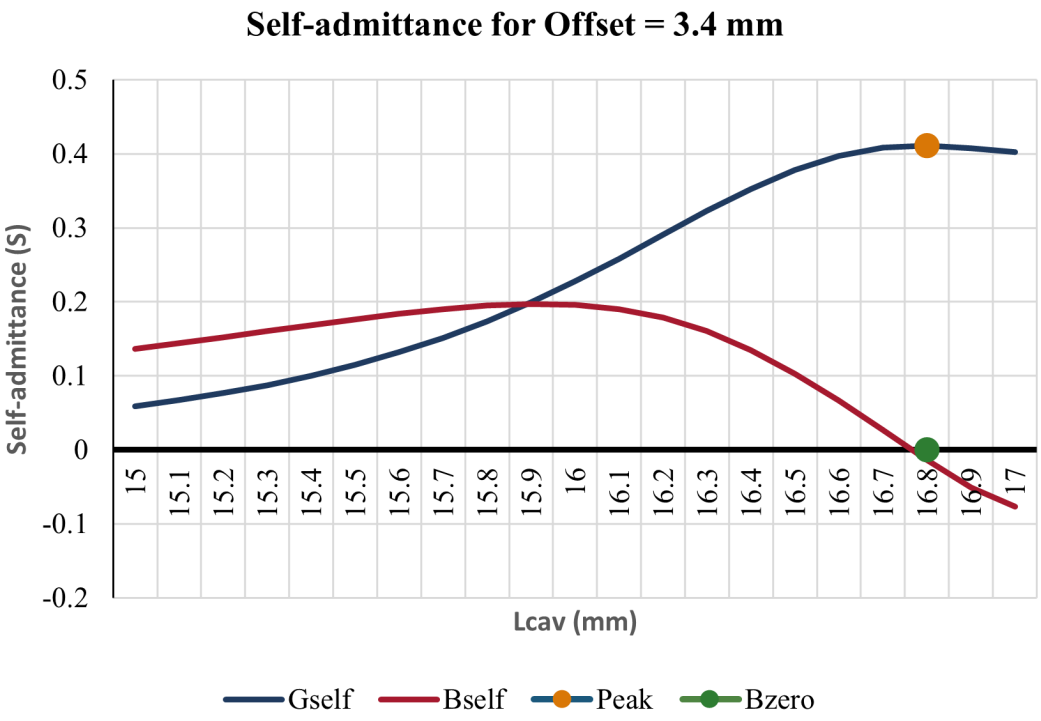


Figure 50. *CST result for slot offset* $x = 3.4$ mm.

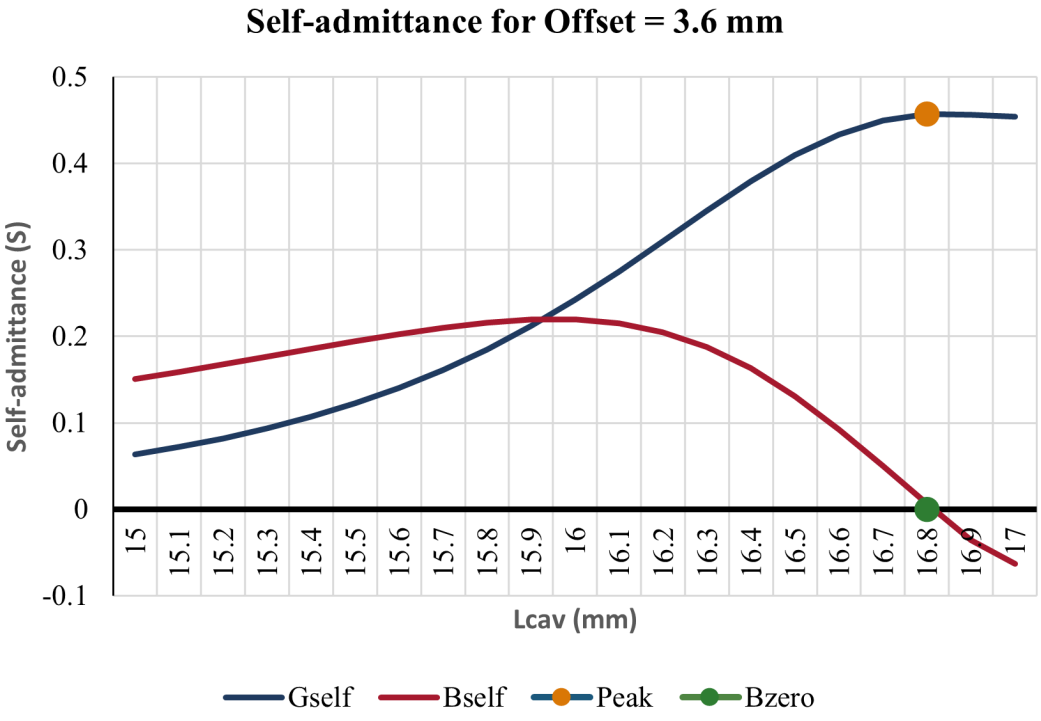


Figure 51. *CST result for slot offset* $x = 3.6$ mm.

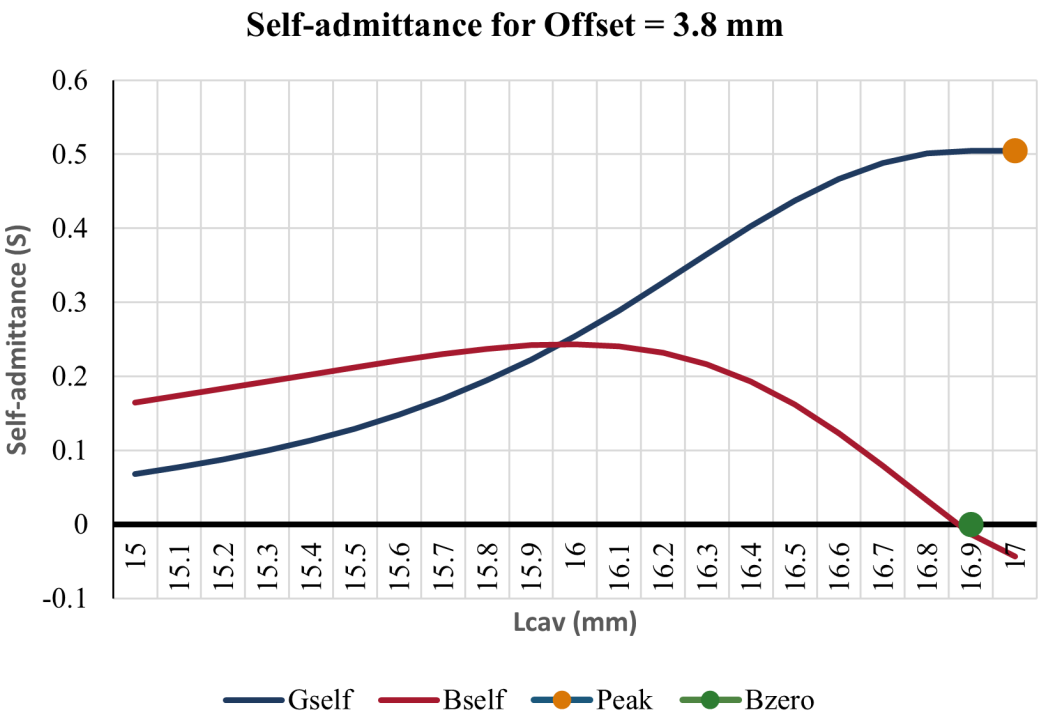


Figure 52. *CST result for slot offset* $x = 3.8$ mm.

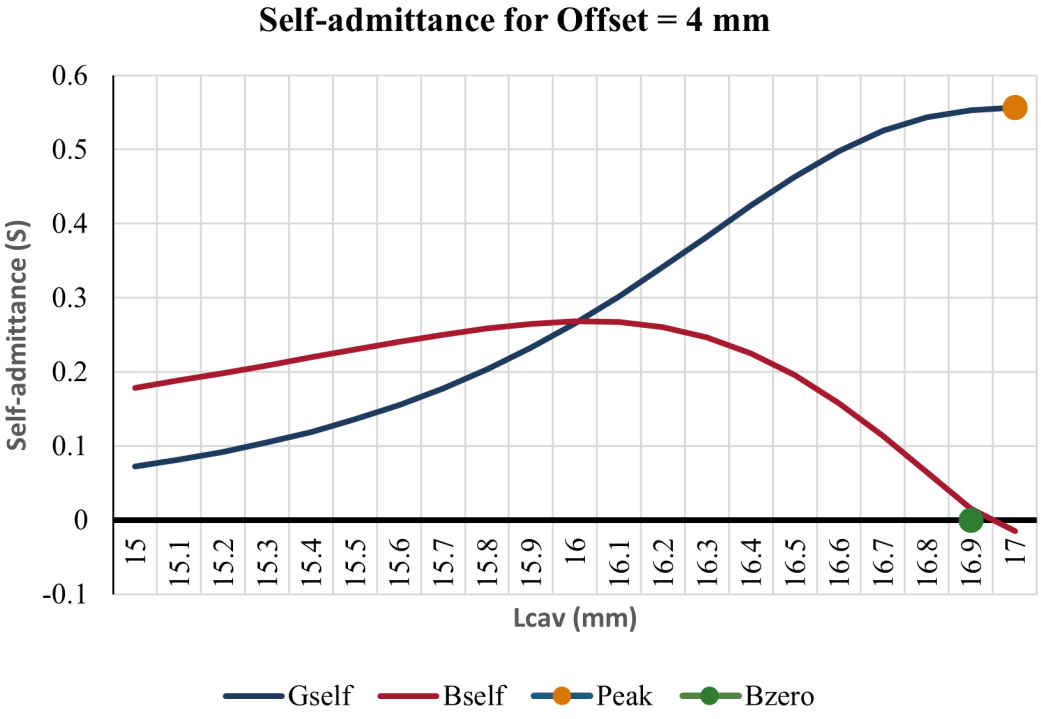


Figure 53. *CST result for slot offset* $x = 4.0$ mm.

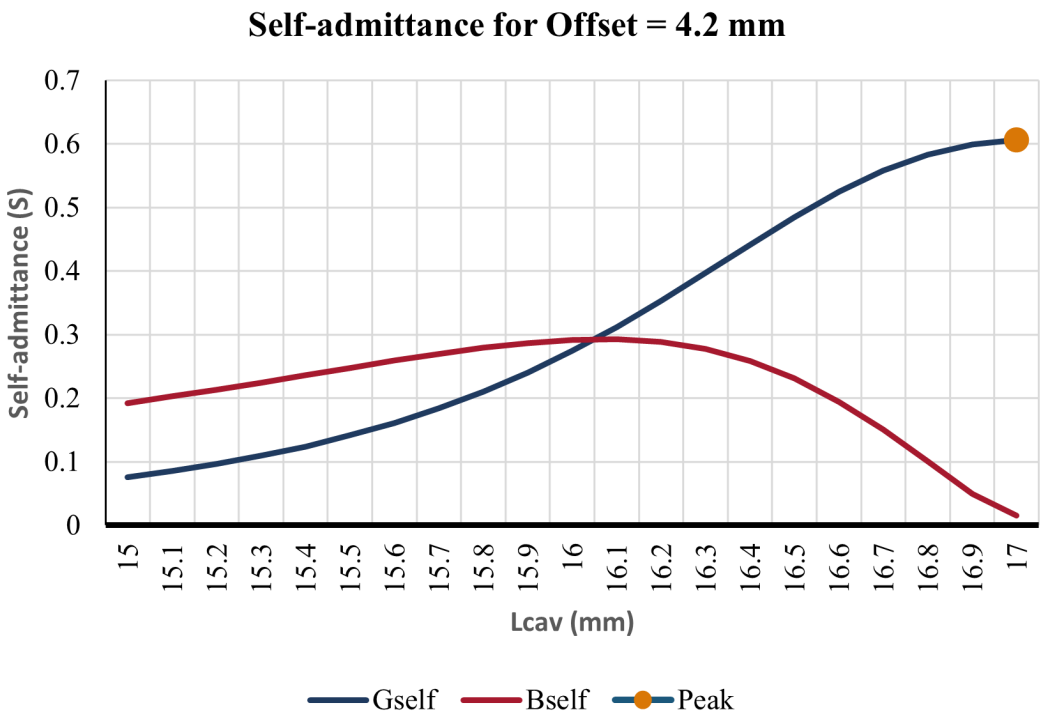


Figure 54. *CST result for slot offset* $x = 4.2$ mm.

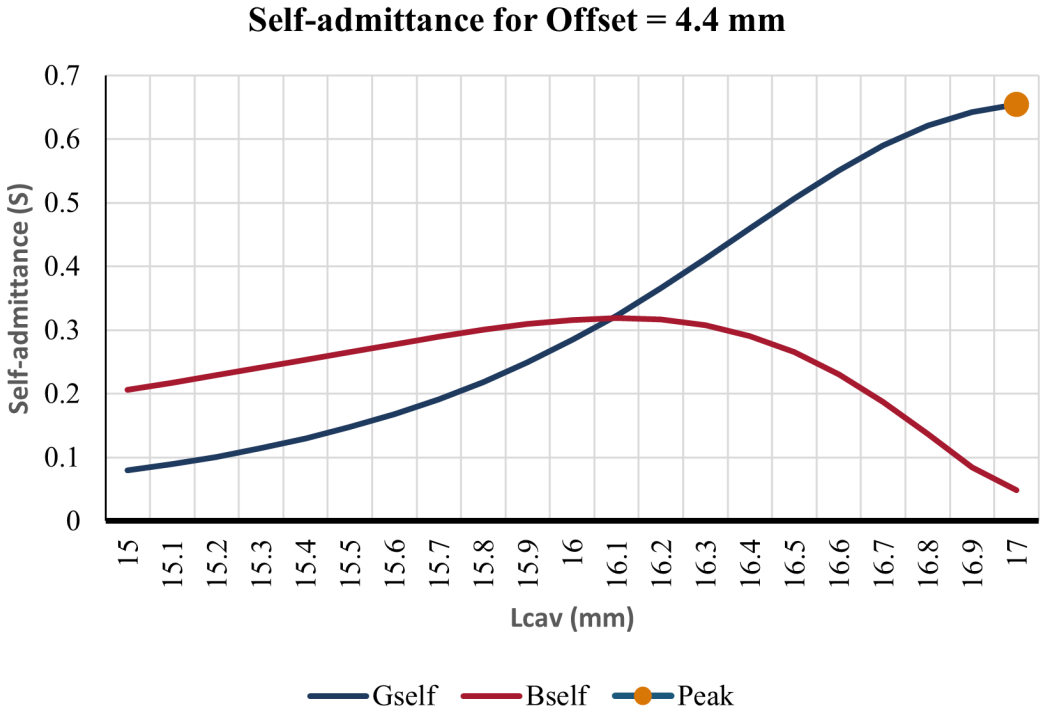


Figure 55. *CST result for slot offset* $x = 4.4$ mm.

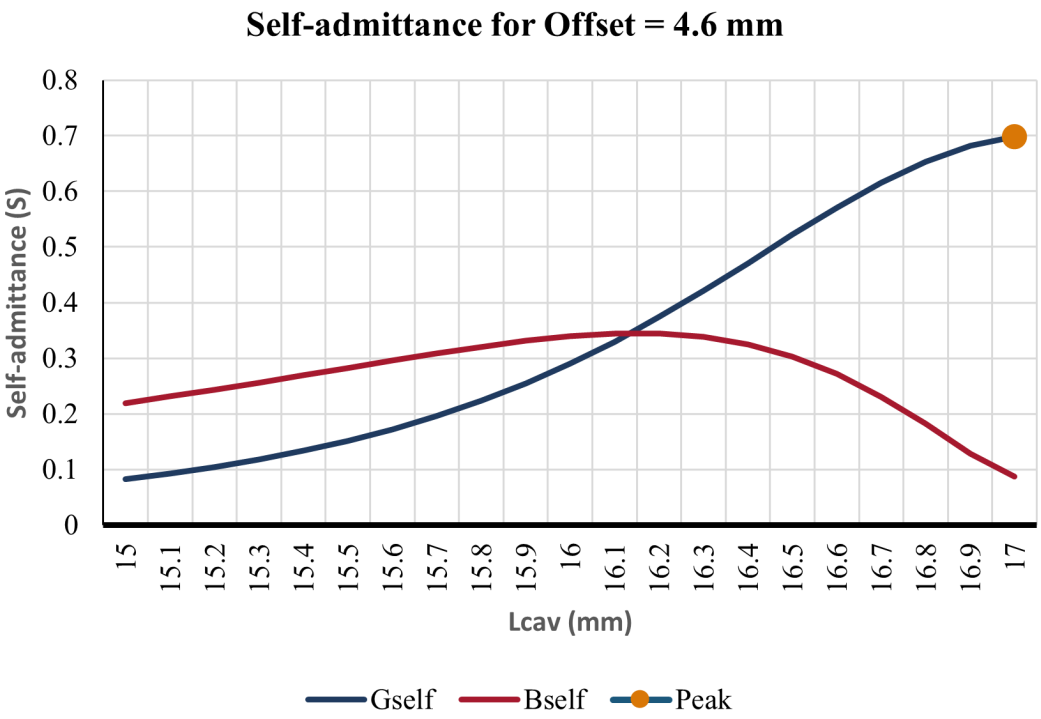


Figure 56. *CST result for slot offset* $x = 4.6$ mm.

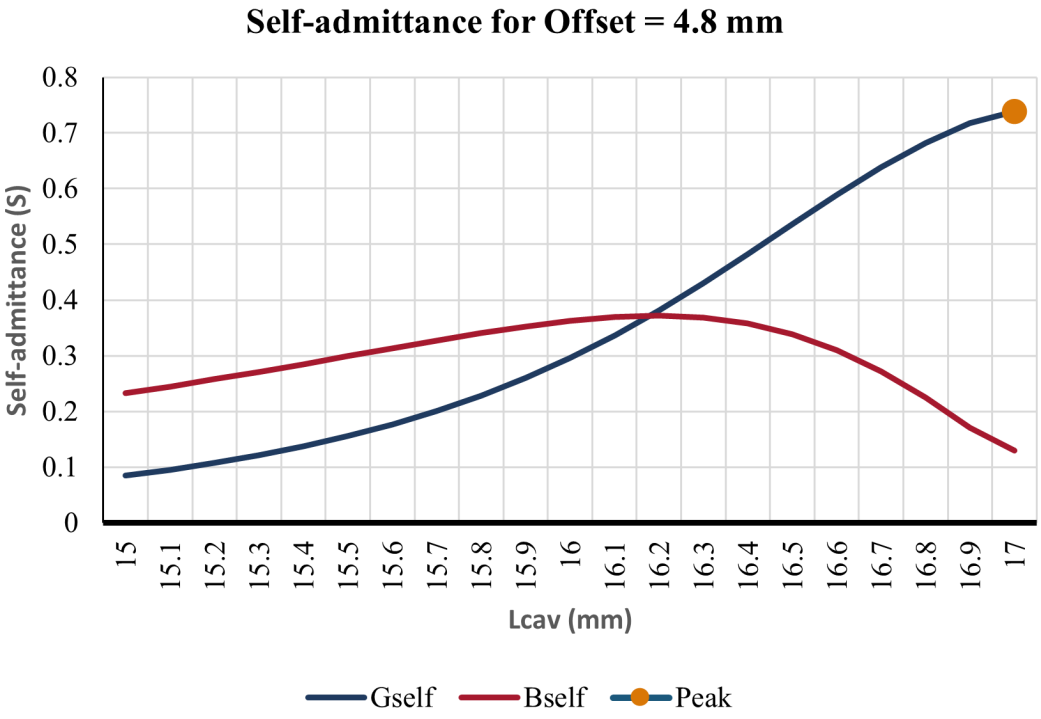


Figure 57. *CST result for slot offset* $x = 4.8$ mm.

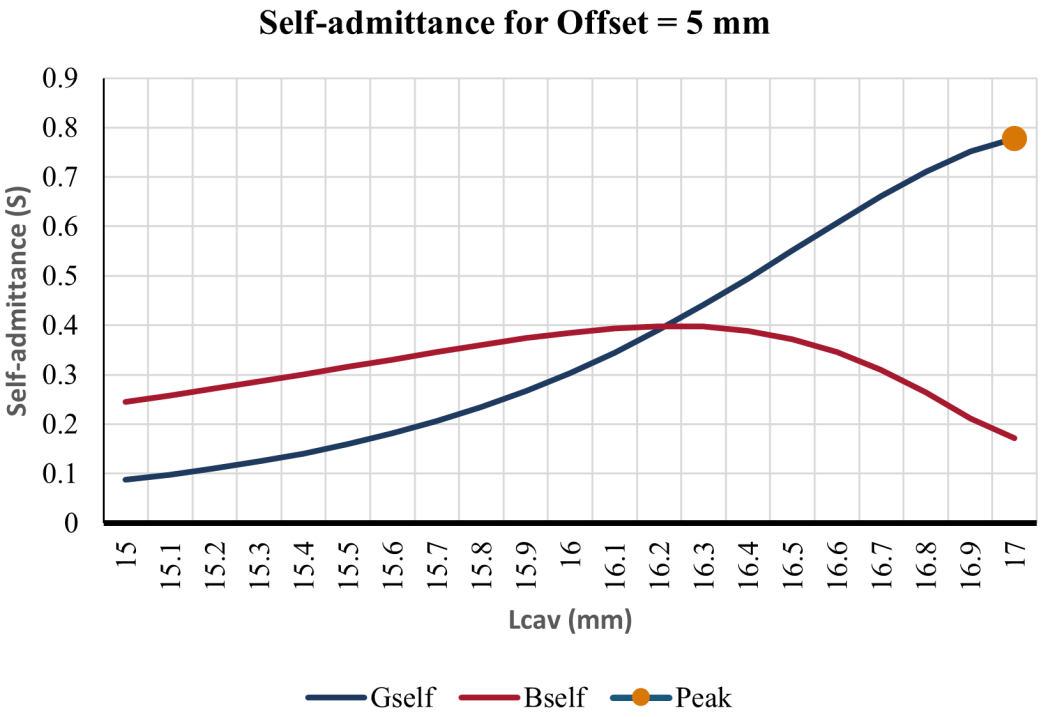


Figure 58. *CST result for slot offset* $x = 5.0$ mm.

Appendix C: Open-Cavity 6 by 6 Parameter Set

This appendix records the final geometric and excitation parameters used for the open-cavity 6×6 slot-array configuration. Unless otherwise stated, all dimensions are given in millimetres.

Table 15
General geometric parameters for the open-cavity 6×6 configuration.

Parameter	**Value**	**Parameter**	**Value**
a_m	22.860	a_b	22.860
a_c	12.000	b_m	10.160
b_b	10.160	b_c	5.000
c_c	18.000	t	1.270
t_{base}	5.000	w	1.5875
d_m	24.315	d_b	24.315
sides	30.000	*ends*	30.000
t_1	1.455	$\lambda_{10,m}$	48.630
$\lambda_{10,b}$	48.630	–	–

Table 16
Cavity-slot offset values $X^{\text{cav}}_{t,n}$ for the open-cavity 6×6 array.

Row t	$n=1$	$n=2$	$n=3$	$n=4$	$n=5$	$n=6$
1	1.293	-1.925	2.764	-2.764	1.925	-1.293
2	1.348	-2.084	2.801	-2.801	2.084	-1.348
3	1.324	-1.848	2.460	-2.460	1.848	-1.324
4	1.320	-1.840	2.495	-2.495	1.840	-1.320
5	1.350	-2.088	2.784	-2.784	2.088	-1.350
6	1.295	-1.932	2.745	-2.745	1.932	-1.295

Table 17
Cavity-slot length values $L^{\text{cav}}_{t,n}$ for the open-cavity 6×6 array.

Row t	$n=1$	$n=2$	$n=3$	$n=4$	$n=5$	$n=6$
1	16.007	16.156	16.323	16.323	16.156	16.007
2	15.832	15.961	16.053	16.053	15.961	15.832
3	15.803	15.912	16.075	16.075	15.912	15.803
4	15.802	15.911	15.997	15.997	15.911	15.802
5	15.833	15.961	16.131	16.131	15.961	15.833
6	16.008	16.157	16.277	16.277	16.157	16.008

Table 18
Coupling-slot angular and length parameters for the open-cavity configuration.

Slot Index	θ_n **(deg)**	L_n **(mm)**
1	6.879	15.775
2	-13.686	15.786
3	17.060	15.792
4	-17.155	15.792
5	13.660	15.786
6	-6.858	15.775

Appendix D: Spline-Based 6 by 6 Slot-Array Synthesis Code

This appendix provides the MATLAB script used to generate the open-cavity 6×6 slot-array parameter set from the single-slot CST sweep data. The script reads the CST-derived lookup table, extracts representative resonant design points, constructs spline interpolation functions, and generates the corresponding cavity-slot offsets and cavity-slot lengths for the array configuration.

```
%% Spline-Based 6x6 Slot Array Synthesis from Single-Slot CST Data
% Excel file:
% OPEN_SLOT_CAVITY (SIM2).xlsm
%
% Purpose:
% Uses the single-slot CST sweep as a lookup table, then applies spline
% interpolation to generate the cavity-slot offset and length values for a
% 6 x 6 slotted waveguide array.

clear; clc; close all;

%% ------------------------------------------------------------------------
%  1. USER SETTINGS
% ------------------------------------------------------------------------

inputFile = "OPEN_SLOT_CAVITY (SIM2).xlsm";
sheetName = "DATA";

outputFolder = "single_slot_outputs";

if ~exist(outputFolder, "dir")
    mkdir(outputFolder);
end

latexFile = fullfile(outputFolder, "spline_generated_6x6_slot_table.tex");
csvFile   = fullfile(outputFolder, "spline_generated_6x6_slot_table.csv");

%% ------------------------------------------------------------------------
%  2. READ EXCEL DATA
% ------------------------------------------------------------------------

if ~isfile(inputFile)
    error("Could not find Excel file: %s", inputFile);
end

data = readtable(inputFile, ...
    "Sheet", sheetName, ...
    "VariableNamingRule", "preserve");

disp("Excel file loaded successfully.");
disp("Available columns:");
disp(data.Properties.VariableNames');

%% ------------------------------------------------------------------------
%  3. EXTRACT SINGLE-SLOT CST LOOKUP DATA
% ------------------------------------------------------------------------

offset_raw = data.("Offset");
Lcav_raw   = data.("L=Lcav");
Gself_raw  = data.("Gself");
Bself_raw  = data.("Bself");

validRows = ~isnan(offset_raw) & ~isnan(Lcav_raw) & ...
            ~isnan(Gself_raw) & ~isnan(Bself_raw);

offset_raw = offset_raw(validRows);
Lcav_raw   = Lcav_raw(validRows);
Gself_raw  = Gself_raw(validRows);
Bself_raw  = Bself_raw(validRows);

offset_values = sort(unique(offset_raw));

%% ------------------------------------------------------------------------
%  4. REDUCE EACH OFFSET SWEEP TO A REPRESENTATIVE DESIGN POINT
% ------------------------------------------------------------------------
% For each offset, select the Lcav value where Gself is maximum.
% This creates a single-slot design curve:
%
% offset -> peak Gself
% offset -> Lcav at peak Gself
%
% This is the curve that will be used for spline interpolation.

peak_Lcav  = NaN(size(offset_values));
peak_Gself = NaN(size(offset_values));
peak_Bself = NaN(size(offset_values));

for k = 1:length(offset_values)

```

```
    x_current = offset_values(k);

    idx = offset_raw == x_current;

    L_local = Lcav_raw(idx);
    G_local = Gself_raw(idx);
    B_local = Bself_raw(idx);

    [Gmax, imax] = max(G_local);

    peak_Lcav(k)  = L_local(imax);
    peak_Gself(k) = Gmax;
    peak_Bself(k) = B_local(imax);

end

%% ------------------------------------------------------------------------
%  5. BUILD SPLINE LOOKUP CURVES
% ------------------------------------------------------------------------
% Forward curves:
%   offset -> peak Gself
%   offset -> peak Lcav
%
% Inverse curve:
%   target Gself -> offset
%
% The inverse curve is what creates the slot positions from desired
% excitation values.

F_G_from_x = griddedInterpolant(offset_values, peak_Gself, "spline", "none");
F_L_from_x = griddedInterpolant(offset_values, peak_Lcav,  "spline", "none");

% For inverse interpolation, peak_Gself must be monotonic.
% Sort by peak_Gself to create G -> x mapping.
[peak_G_sorted, sortIdx] = sort(peak_Gself);
offset_sorted_by_G = offset_values(sortIdx);

F_x_from_G = griddedInterpolant(peak_G_sorted, offset_sorted_by_G, ...
    "spline", "none");

%% ------------------------------------------------------------------------
%  6. DEFINE 6x6 ARRAY EXCITATION DISTRIBUTION
% ------------------------------------------------------------------------
% The supervisor-style table is not created by using one global optimum.
% Instead, each array element gets its own required excitation.
%
% Here, a symmetric aperture weighting is used. The centre columns radiate
% more strongly than the edge columns. A row taper is also applied.
%
% You can tune these values until they match the desired array distribution.

% Column excitation profile across the 6 slots.
% Symmetric about the centre.
columnWeight = [0.25 0.48 1.00 1.00 0.48 0.25];

% Row excitation profile along the 6 rows.
% Nearly symmetric, with small variation across rows.
rowWeight = [1.00 0.92 0.83 0.82 0.93 1.00];

% 6x6 target excitation matrix
targetWeight = rowWeight(:) * columnWeight(:).';

% Scale target weights into the valid peak-Gself range from the single-slot data.
% This controls the minimum and maximum slot strengths used in the array.

G_min_target = 0.05;
G_max_target = 0.27;

targetG = G_min_target + ...
    (G_max_target - G_min_target) .* ...
    (targetWeight - min(targetWeight(:))) ./ ...
    (max(targetWeight(:)) - min(targetWeight(:)));

%% ------------------------------------------------------------------------
%  7. GENERATE 6x6 CAVITY-SLOT OFFSETS USING INVERSE SPLINE
% ------------------------------------------------------------------------

xcav_mag = NaN(6,6);
Lcav_array = NaN(6,6);
G_check = NaN(6,6);

for t = 1:6
    for n = 1:6

        G_target = targetG(t,n);

        % Inverse spline: target conductance -> offset magnitude
```

```
        x_mag = F_x_from_G(G_target);

        % Forward spline: offset magnitude -> Lcav at selected curve
        L_val = F_L_from_x(x_mag);

        xcav_mag(t,n) = x_mag;
        Lcav_array(t,n) = L_val;
        G_check(t,n) = F_G_from_x(x_mag);

    end
end

%% ------------------------------------------------------------------------
%  8. ASSIGN OFFSET SIGNS ABOUT THE WAVEGUIDE CENTRELINE
% ------------------------------------------------------------------------
% The single-slot CST sweep usually gives offset magnitude.
% The sign is assigned according to the physical slot placement.
%
% This sign pattern matches the alternating/mirrored style seen in the
% supervisor table.

signPattern = [
     1 -1  1 -1  1 -1;
     1 -1  1 -1  1 -1;
     1 -1  1 -1  1 -1;
     1 -1  1 -1  1 -1;
     1 -1  1 -1  1 -1;
     1 -1  1 -1  1 -1
];

xcav_array = signPattern .* xcav_mag;

%% ------------------------------------------------------------------------
%  9. COUPLING SLOT VALUES
% ------------------------------------------------------------------------
% These are normally generated from a separate coupling-slot synthesis step.
% Here, the supervisor-style values are included directly.

theta_t = [
      6.879;
    -13.686;
     17.060;
    -17.155;
     13.660;
     -6.858
];

l_t = [
    15.775;
    15.786;
    15.792;
    15.792;
    15.786;
    15.775
];

%% ------------------------------------------------------------------------
%  10. SAVE CSV OUTPUT
% ------------------------------------------------------------------------

t_col = repelem((1:6)', 6);
n_col = repmat((1:6)', 6, 1);

xcav_col = reshape(xcav_array.', [], 1);
Lcav_col = reshape(Lcav_array.', [], 1);
Gtarget_col = reshape(targetG.', [], 1);
Gcheck_col  = reshape(G_check.', [], 1);

outputTable = table( ...
    t_col, ...
    n_col, ...
    xcav_col, ...
    Lcav_col, ...
    Gtarget_col, ...
    Gcheck_col, ...
    'VariableNames', {'t', 'n', 'xcav_mm', 'Lcav_mm', ...
                      'target_Gself', 'spline_Gself'} ...
);

writetable(outputTable, csvFile);

%% ------------------------------------------------------------------------
%  11. GENERATE LATEX TABLE
% ------------------------------------------------------------------------

fid = fopen(latexFile, "w");

```

```
if fid == -1
    error("Could not create LaTeX file.");
end

fprintf(fid, "\\begin{table}[H]\n");
fprintf(fid, "\\centering\n");
fprintf(fid, "\\caption{Cavity slot and coupling slot dimensions.}\n");
fprintf(fid, "\\label{tab:cavity_coupling_slot_dimensions}\n");
fprintf(fid, "\\scriptsize\n");
fprintf(fid, "\\setlength{\\tabcolsep}{3pt}\n");
fprintf(fid, "\\renewcommand{\\arraystretch}{1.00}\n\n");

fprintf(fid, "\\begin{tabularx}{\\columnwidth}{\n");
fprintf(fid, ">{\\centering\\arraybackslash}p{0.20\\columnwidth}\n");
fprintf(fid, ">{\\centering\\arraybackslash}p{0.38\\columnwidth}\n");
fprintf(fid, ">{\\centering\\arraybackslash}p{0.38\\columnwidth}}\n");

fprintf(fid, "\\hline\\hline\n");
fprintf(fid, "\\textbf{Element} &\n");
fprintf(fid, "\\textbf{Cavity slot offset} &\n");
fprintf(fid, "\\textbf{Cavity slot length} \\\\\n");
fprintf(fid, "\\textbf{index} &\n");
fprintf(fid, "\\textbf{$x^{\\mathrm{cav}}_{t,n}$ (mm)} &\n");
fprintf(fid, "\\textbf{$L^{\\mathrm{cav}}_{t,n}$ (mm)} \\\\\n");
fprintf(fid, "\\hline\n");

for t = 1:6
    for n = 1:6

        isHighlighted = (t == 3 && n == 3) || ...
                        (t == 3 && n == 4) || ...
                        (t == 4 && n == 3) || ...
                        (t == 4 && n == 4);

        if isHighlighted
            fprintf(fid, "\\cellcolor{SlotHighlight}%d,%d &\n", t, n);
            fprintf(fid, "\\cellcolor{SlotHighlight}% .3f &\n", xcav_array(t,n));
            fprintf(fid, "\\cellcolor{SlotHighlight}%.3f \\\\\n", Lcav_array(t,n));
        else
            fprintf(fid, "%d,%d & % .3f & %.3f \\\\\n", ...
                t, n, xcav_array(t,n), Lcav_array(t,n));
        end

    end
end

fprintf(fid, "\\hline\\hline\n");
fprintf(fid, "\\textbf{Slot} &\n");
fprintf(fid, "\\textbf{Coupling slot angle} &\n");
fprintf(fid, "\\textbf{Coupling slot length} \\\\\n");
fprintf(fid, "\\textbf{index} &\n");
fprintf(fid, "\\textbf{$\\theta_t$ (deg.)} &\n");
fprintf(fid, "\\textbf{$l_t$ (mm)} \\\\\n");
fprintf(fid, "\\hline\n");

for t = 1:6
    fprintf(fid, "%d & % .3f & %.3f \\\\\n", t, theta_t(t), l_t(t));
end

fprintf(fid, "\\hline\\hline\n");
fprintf(fid, "\\end{tabularx}\n\n");
fprintf(fid, "\\vspace{-2mm}\n");
fprintf(fid, "\\end{table}\n");

fclose(fid);

%% ------------------------------------------------------------------------
%  12. PLOTS FOR CHECKING THE SPLINE PROCESS
% ------------------------------------------------------------------------

xFine = linspace(min(offset_values), max(offset_values), 500);
Gfine = F_G_from_x(xFine);
Lfine = F_L_from_x(xFine);

figure('Color','w');
plot(offset_values, peak_Gself, 'ko', 'MarkerFaceColor', 'w');
hold on;
plot(xFine, Gfine, 'LineWidth', 1.5);
xlabel('Cavity slot offset, x^{cav} (mm)', 'Interpreter', 'tex');
ylabel('Peak G_{self}', 'Interpreter', 'tex');
title('Spline Interpolation: Offset to Peak Conductance', 'Interpreter', 'tex');
legend('Single-slot CST points', 'Spline curve', 'Location', 'best');
grid on;
set(gca, 'FontName', 'Times New Roman', 'FontSize', 11);

exportgraphics(gcf, fullfile(outputFolder, ...
    "spline_offset_to_Gself.png"), 'Resolution', 600);
```

```
341
342 figure('Color','w');
343 plot(offset_values, peak_Lcav, 'ko', 'MarkerFaceColor', 'w');
344 hold on;
345 plot(xFine, Lfine, 'LineWidth', 1.5);
346 xlabel('Cavity slot offset, x^{cav} (mm)', 'Interpreter', 'tex');
347 ylabel('Selected cavity slot length, L^{cav} (mm)', 'Interpreter', 'tex');
348 title('Spline Interpolation: Offset to Cavity Slot Length', 'Interpreter', 'tex');
349 legend('Single-slot CST points', 'Spline curve', 'Location', 'best');
350 grid on;
351 set(gca, 'FontName', 'Times New Roman', 'FontSize', 11);
352
353 exportgraphics(gcf, fullfile(outputFolder, ...
354     "spline_offset_to_Lcav.png"), 'Resolution', 600);
355
356 figure('Color','w');
357 imagesc(abs(xcav_array));
358 axis equal tight;
359 colorbar;
360 xlabel('Column index, n');
361 ylabel('Row index, t');
362 title('Generated 6x6 Cavity Slot Offset Magnitudes', 'Interpreter', 'tex');
363 set(gca, 'FontName', 'Times New Roman', 'FontSize', 11);
364
365 exportgraphics(gcf, fullfile(outputFolder, ...
366     "generated_6x6_offset_map.png"), 'Resolution', 600);
367
368 %% ------------------------------------------------------------------------
369 %  13. DISPLAY OUTPUT
370 % ------------------------------------------------------------------------
371
372 fprintf("\n=====================================================\n");
373 fprintf("Spline-Based 6x6 Slot Synthesis Complete\n");
374 fprintf("=====================================================\n");
375 fprintf("Input Excel file: %s\n", inputFile);
376 fprintf("Sheet used:       %s\n", sheetName);
377 fprintf("CSV output:       %s\n", csvFile);
378 fprintf("LaTeX output:     %s\n", latexFile);
379 fprintf("=====================================================\n\n");
380
381 disp("Generated x_cav matrix:");
382 disp(xcav_array);
383
384 disp("Generated L_cav matrix:");
385 disp(Lcav_array);
```

Listing 1: MATLAB script for spline-based 6×6 slot-array synthesis from single-slot CST data.

Appendix E: Radiated Curve Integrated Electric-Field Data

This appendix records the integrated radiated electric-field values extracted from the CST curve-radiation data for the open-cavity 6×6 slot-array configuration. The real and imaginary components are tabulated directly from the exported CST records. The magnitude and phase tables are included as derived quantities for compact comparison across the array aperture.

Table 19
Real component of the integrated radiated electric field, $\Re\{E_{\mathrm{rad},t,n}\}$.

Row t	$n=1$	$n=2$	$n=3$	$n=4$	$n=5$	$n=6$
1	1.431	1.558	2.190	1.648	1.964	1.226
2	3.054	4.102	5.318	4.756	4.457	2.898
3	4.016	5.904	7.000	6.831	5.874	4.119
4	4.092	5.899	6.913	7.012	5.846	3.975
5	2.916	4.466	4.938	5.375	4.122	3.031
6	1.242	1.998	1.806	2.341	1.430	1.449

Table 20
Imaginary component of the integrated radiated electric field, $\Im\{E_{\mathrm{rad},t,n}\}$.

Row t	$n=1$	$n=2$	$n=3$	$n=4$	$n=5$	$n=6$
1	-1.215	-2.300	-3.730	-3.471	-2.381	-1.142
2	-1.974	-4.400	-6.255	-6.780	-4.040	-2.161
3	-2.543	-5.235	-7.799	-8.266	-5.021	-2.617
4	-2.775	-5.228	-8.654	-8.240	-5.634	-2.724
5	-2.000	-3.786	-6.294	-5.878	-4.209	-1.942
6	-1.155	-2.433	-3.494	-3.758	-2.422	-1.197

Table 21
Magnitude of the integrated radiated electric field, $|E_{\mathrm{rad},t,n}|$.

Row t	$n=1$	$n=2$	$n=3$	$n=4$	$n=5$	$n=6$
1	1.877	2.778	4.325	3.843	3.087	1.675
2	3.636	6.016	8.210	8.282	6.015	3.615
3	4.753	7.891	10.480	10.723	7.728	4.880
4	4.944	7.883	11.076	10.820	8.119	4.819
5	3.535	5.855	8.000	7.965	5.891	3.600
6	1.696	3.148	3.933	4.427	2.813	1.880

Table 22
Phase of the integrated radiated electric field, $\angle E_{\mathrm{rad},t,n}$ in degrees.

Row t	$n=1$	$n=2$	$n=3$	$n=4$	$n=5$	$n=6$
1	-40.349	-55.886	-59.580	-64.604	-50.481	-42.976
2	-32.886	-47.006	-49.632	-54.950	-42.190	-36.711
3	-32.349	-41.564	-48.091	-50.430	-40.527	-32.437
4	-34.140	-41.551	-51.379	-49.600	-43.945	-34.417
5	-34.441	-40.285	-51.880	-47.559	-45.600	-32.640
6	-42.930	-50.601	-62.673	-58.078	-59.440	-39.539

Appendix F: C++ Code for Aperture Voltage Analysis

This appendix provides the C++ program used to process the complex aperture-voltage data for the 6×6 slot-array configuration. The program stores the real and imaginary components of V_{app}, computes the corresponding magnitude and phase distributions, evaluates the centre-four average response, normalises the aperture-voltage magnitude, and calculates phase deviation across the array.

```cpp
// vapp_analysis.cpp
// Purpose: Analyze 6x6 complex Vapp data (Re + i*Im), compute magnitude/phase,
//          center-4 averages, normalized magnitude, and phase deviation grids.
//
// Build:
//   g++ -O2 -std=c++17 vapp_analysis.cpp -o vapp_analysis.exe
//
// Run:
//   ./vapp_analysis.exe

#include <iostream>
#include <iomanip>
#include <cmath>
#include <complex>
#include <fstream>

int main() {
    constexpr int N = 6;
    const double RAD2DEG = 180.0 / std::acos(-1.0);

    std::ofstream outFile("vapp_analysis_output.txt");
    if (!outFile) {
        std::cerr << "Error: Could not create output file "
                  << "'vapp_analysis_output.txt'.\n";
        return 1;
    }

    // Re[Vapp] with i = row 1..6 and j = column 1..6
    const double Re[N][N] = {
        {1.4306804942992, 1.5578194451661, 2.1900688904949,
         1.6480174134865, 1.9642274168938, 1.2255279350535},
        {3.0535856389074, 4.1024130928465, 5.3176739858674,
         4.7560391046071, 4.4568883051169, 2.8979241354045},
        {4.0155145086903, 5.9038670153139, 6.9997624474471,
         6.8310145760952, 5.8737174719142, 4.1186668501635},
        {4.0919447574590, 5.8991211347727, 6.9134569903258,
         7.0123716040461, 5.8456113378081, 3.9752391497389},
        {2.9157367925029, 4.4662918463924, 4.9382998974743,
         5.3748797986801, 4.1220500573594, 3.0313798325779},
        {1.2417566637163, 1.9981187617230, 1.8056540605840,
         2.3408194825198, 1.4303270226417, 1.4494986692941}
    };

    // Im[Vapp] with i = row 1..6 and j = column 1..6
    const double Im[N][N] = {
        {-1.2154238411443, -2.2996391058387, -3.7298772507791,
         -3.4713106709322, -2.3812305924632, -1.1418836379064},
        {-1.9743629597035, -4.4002507636670, -6.2552735849317,
         -6.7797270745564, -4.0398089827427, -2.1609317611943},
        {-2.5433471044723, -5.2351480614382, -7.7989529044899,
         -8.2660449942037, -5.0214958504663, -2.6174743859838},
        {-2.7746599421165, -5.2284420535237, -8.6539805804671,
         -8.2396121540260, -5.6341608116956, -2.7236335369846},
        {-1.9995057080881, -3.7856949723058, -6.2936020413673,
         -5.8777243383082, -4.2092328652306, -1.9416434072191},
        {-1.1551362884020, -2.4326532260321, -3.4943215068759,
         -3.7575262169703, -2.4224560816959, -1.1965266421293}
    };

    double mag[N][N];
    double phaseDeg[N][N];

    for (int i = 0; i < N; ++i) {
        for (int j = 0; j < N; ++j) {
            mag[i][j] = std::hypot(Re[i][j], Im[i][j]);
            phaseDeg[i][j] = std::atan2(Im[i][j], Re[i][j]) * RAD2DEG;
        }
    }

    // Centre-four average:
    // array positions (3,3), (3,4), (4,3), and (4,4)
    double magCenter =
        (mag[2][2] + mag[2][3] + mag[3][2] + mag[3][3]) / 4.0;

    double phaseCenter =
        (phaseDeg[2][2] + phaseDeg[2][3] +
         phaseDeg[3][2] + phaseDeg[3][3]) / 4.0;

    auto printGrid = [&](const char* title, auto& g,
```

```
                        const char* unit, int prec) {
        std::cout << "\n=== " << title << " ===\n";
        outFile  << "\n=== " << title << " ===\n";

        std::cout << "          ";
        outFile  << "          ";

        for (int j = 1; j <= N; ++j) {
            std::cout << std::setw(12) << ("j=" + std::to_string(j));
            outFile  << std::setw(12) << ("j=" + std::to_string(j));
        }

        std::cout << "\n";
        outFile  << "\n";

        for (int i = 0; i < N; ++i) {
            std::cout << "i=" << (i + 1) << "  ";
            outFile  << "i=" << (i + 1) << "  ";

            for (int j = 0; j < N; ++j) {
                std::cout << std::setw(11)
                          << std::fixed << std::setprecision(prec)
                          << g[i][j] << unit;

                outFile << std::setw(11)
                        << std::fixed << std::setprecision(prec)
                        << g[i][j] << unit;
            }

            std::cout << "\n";
            outFile  << "\n";
        }
    };

    std::cout << std::fixed << std::setprecision(6);
    outFile  << std::fixed << std::setprecision(6);

    printGrid("Re[Vapp]", Re, "", 6);
    printGrid("Im[Vapp]", Im, "", 6);
    printGrid("|Vapp| Magnitude", mag, "", 6);
    printGrid("Phase Angle", phaseDeg, " deg", 2);

    std::cout << "\n=== Vapp = Re + i Im ===\n";
    outFile  << "\n=== Vapp = Re + i Im ===\n";

    for (int i = 0; i < N; ++i) {
        std::cout << "i=" << (i + 1) << "  ";
        outFile  << "i=" << (i + 1) << "  ";

        for (int j = 0; j < N; ++j) {
            char sign = (Im[i][j] >= 0) ? '+' : '-';

            std::cout << std::setw(8) << std::fixed
                      << std::setprecision(3) << Re[i][j]
                      << " " << sign << " "
                      << std::setw(6) << std::fixed
                      << std::setprecision(3) << std::fabs(Im[i][j])
                      << "i   ";

            outFile << std::setw(8) << std::fixed
                    << std::setprecision(3) << Re[i][j]
                    << " " << sign << " "
                    << std::setw(6) << std::fixed
                    << std::setprecision(3) << std::fabs(Im[i][j])
                    << "i   ";
        }

        std::cout << "\n";
        outFile  << "\n";
    }

    std::cout << "\n=== Centre-Four Averages ===\n";
    outFile  << "\n=== Centre-Four Averages ===\n";

    std::cout << "Average |Vapp| centre four = "
              << magCenter << "\n";
    outFile  << "Average |Vapp| centre four = "
             << magCenter << "\n";

    std::cout << "Average phase centre four = "
              << std::setprecision(4) << phaseCenter << " deg\n";
    outFile  << "Average phase centre four = "
             << std::setprecision(4) << phaseCenter << " deg\n";

    double normMag[N][N];

    for (int i = 0; i < N; ++i) {
```

```
        for (int j = 0; j < N; ++j) {
            normMag[i][j] = mag[i][j] / magCenter;
        }
    }

    printGrid("|Vapp(i,j)| / |Vcenter|", normMag, "", 4);

    double phaseDev[N][N];

    for (int i = 0; i < N; ++i) {
        for (int j = 0; j < N; ++j) {
            phaseDev[i][j] = phaseDeg[i][j] - phaseCenter;
        }
    }

    printGrid("Phase deviation from centre", phaseDev, " deg", 2);

    std::cout << "\n=== Sanity Checks ===\n";
    outFile  << "\n=== Sanity Checks ===\n";

    double sumDevCenter =
        phaseDev[2][2] + phaseDev[2][3] +
        phaseDev[3][2] + phaseDev[3][3];

    double avgNormCenter =
        (normMag[2][2] + normMag[2][3] +
         normMag[3][2] + normMag[3][3]) / 4.0;

    std::cout << "Sum of centre-four phase deviations: "
              << std::scientific << std::setprecision(3)
              << sumDevCenter << "\n";

    outFile << "Sum of centre-four phase deviations: "
            << std::scientific << std::setprecision(3)
            << sumDevCenter << "\n";

    std::cout << "Average centre-four normalised magnitude: "
              << std::fixed << std::setprecision(6)
              << avgNormCenter << "\n";

    outFile << "Average centre-four normalised magnitude: "
            << std::fixed << std::setprecision(6)
            << avgNormCenter << "\n";

    return 0;
}
```

Listing 2: C++ program used to analyse the complex aperture-voltage distribution of the 6×6 slot array.